Localized Effects of Piezopolymer Devices on the Dynamics of Inflatable Space-Based Structures

by

Robert Brett Williams

Thesis submitted to the faculty of

Virginia Polytechnic Institute and State University

in partial fulfillment of the requirements for the degree of

Master of Science

in

Mechanical Engineering

Dr. Daniel J. Inman, Chairman

Dr. Eric M. Austin

Dr. Norman E. Dowling

August 14, 2000
Blacksburg, Virginia

Keywords: inflatable, satellites, PVDF, layered, membrane, patch

Localized Effects of Piezopolymer Devices on the Dynamics of Inflatable Space-Based Structures

R. Brett Williams

Dr. Daniel J. Inman, Chairman
Virginia Polytechnic Institute and State University
Department of Mechanical Engineering

(Abstract)

Inflatable space-based devices have become popular over the past three decades, as they offer minimized launch-mass and launch-volume. Since some satellites have mirror sections over fifty feet in diameter and struts with lengths over ninety feet, inflation while in orbit has become a necessary procedure. Once inflated, these space structures are subject to two types of vibrations: those induced mechanically by guidance systems and space debris and those induced thermally from variable amounts of direct sunlight as they orbit about earth. Controlling vibrations of spaced-based structures is critical to ensuring optimal performance.
The focus of this research is derived from an Air Force program to develop and model an active control system using smart materials to suppress the vibrations of inflatable communication satellites. When small piezoceramic devices are attached to an aluminum or steel structure, the effects of the piezo on the dynamic properties of the host are typically ignored. However, the inflatable satellites of interest to this project are manufactured from Kapton®, a thin, light polyimide film. Therefore, even a piezopolymer film actuator, such as PVDF, could greatly change the mass and stiffness values in the area under and around the patch, altering the dynamic behavior of the satellite.

Thin-walled pressure vessel theory was employed to assess the state of stress at any location on an inflated torus. A flat, rectangular coupon was selected at a general point on the structure and modeled as a membrane. The equation of motion for this membrane with clamped edges was derived and a closed-form solution for the natural frequencies and mode shapes was presented. The Rayleigh-Ritz and finite element methods were then seen to numerically approximate the natural frequencies and mode shapes for the bare membrane with a high degree of accuracy. A passive PVDF patch was then attached to the base membrane and the equation of motion derived using an energy approach. Since a closed-form solution was not readily available, the Rayleigh-Ritz and finite element methods were again employed to obtain approximate results that agreed remarkably well. Trends in natural frequencies for various patch areas and thicknesses were explored. It was shown, that membrane theory represented the added mass of the patch but was unable to account for the added stiffness of the PVDF attachment. Traditional membrane theory was also unable to model an active PVDF patch as a sensor for out of plane vibrations, but the ability of the patch to alter the tension in the base layer was predicted.

Acknowledgements

The Air Force Office of Scientific Research (AFOSR) supported this research effort under grant number F49620-99-1-0231. The financial and technological support of this organization is gratefully acknowledged.

I would like to thank **Dr. Daniel J. Inman**, the Yoda to my Luke Skywalker, for his endless support, e-mails and flexibility on research topics, without which none of this work would have been possible.

I would like to thank **Dr. Eric M. Austin** for always having an open or semi-open door and bookshelf policy. He was always there to answer my simple questions with unbelievably difficult answers and suggestions for further readings and derivations.

Thanks to **Dr. Norman E. Dowling** for serving on my committee and answering all of my materials related questions. His classes and lab sessions have taught me a great deal about how and why things break.

Thanks to **Dr. Gyuhae Park** for his assistance and clear perspective near the conclusion of this work.

Thanks to **Gil Briand** and **Jake Lewis** for their work on this inflatable satellite project. Jake's ANSYS finite element expertise helped create large parts of Chapters 4 and 5.

Thanks to **Hildy Bachman** for reading and editing this thesis. Her experience as a technical editor has proved invaluable while making revisions to this work.

Thanks goes out to my **CIMSS colleagues** who were forced to work alongside me, for listening to my endless barrage of sordid spring break tales. Your companionship both in the office and at the bars has sustained me during my time at CIMSS.

Thanks to **Bob and Mary Williams** for their support and guidance from the beginning. They have taught me many valuable lessons, most importantly to not settle for mediocrity; I should strive to be the best at everything I attempt. However, vegetables and meatloaf are NOT crucial to the survival of the human species. Thanks also to my "bigger" little brother **Brian Williams**, who has become a great friend over the past few years.

My undying gratitude and admiration goes out to **Rachel Bachman**, a woman with an infinite amount of love, patience and tolerance for me. Without her affection, companionship and home-cooked meals this work would have never been finished, as I would have died from malnutrition long ago.

Table of Contents

List of Tables

List of Figures

Chapter 1

Introduction, Satellite Description and Background

1.1 Motivation:

The use of inflatable structures in geocentric orbit has become an imperative procedure over the past three decades, with some satellites having mirror sections over fifty feet in diameter and struts over excess of ninety feet in length. Clearly such a large structure would not fit inside the payload bay of the Space Shuttle, but when deflated, an entire satellite can be stored in a container approximately the size of a typical office desk (6'x3'x3') [Freeland 1998]. Besides allowing enormous satellites to be put into orbit, this deflation and packaging procedure allows minimized launch-mass and launch-volume, which saves money in terms of launch costs for a particular satellite project.

Despite these advantages, inflatable space-based structures are susceptible to various types of problems. For instance, great care must be taken to package the deflated satellite so that it is easily inflated once in orbit. Also, an inflation system must be designed to pump an inert gas, typically nitrogen, into the

structure. Both of these facets must be thoroughly considered in addition to the fact that inflation and deployment must be done in the microgravity conditions of space.

After being properly inflated, the potential for complications only increases. First, there is an abundance of space debris from both natural causes such as meteors and asteroids as well as human activity in space. These objects, some small and some large, are traveling with extremely high velocity, and impact with inflated satellites constructed from a thin plastic film would cause the structure to tear and deflate. Another serious problem with space vehicles and satellites is vibration disturbances. In the past, many notable space-based structures have experienced vibrations so severe that the device was essentially debilitated for an extended period of time. For example, the Hubble Telescope experienced thermally induced vibrations that rendered the high-powered observatory "blind" for fifteen minutes as it passed into the sunlight from the earth's shadow [Nurre et al. 1995]. A different design problem called Controlled Structures Interactions caused vibrations that rendered the Space Shuttle's Remote Manipulator System inoperable for fifty percent of the time it was in use [Ketner 1989].

With the knowledge gained from past vibration problems, the United States Air Force has decided to investigate the use of active vibration control with smart material sensors and actuators for future projects with inflatable communications satellites. Thus, the foundation of this study is derived from collaborative efforts between the Center for Intelligent Material Systems and Structures (CIMSS) at Virginia Tech and the Air Force Institute of Technology to model inflatable satellites and design such an active control system.

1.2 Description of Inflatable Satellite:

The satellites of interest to this project typically consist of a parabolic membrane reflector stretched across the inside of an inflated torus. Three inflated struts extend out from the plane of the torus and join together at the end opposite the reflector. The electronic system is mounted at this end of the satellite. This device contains communication devices, guidance and navigation systems and deployment hardware, which controls inflation of the satellite. The communications hardware is responsible for sending and receiving signals by reflecting them off of the adjacent membrane. The Spartan 207 satellite, shown in Figure 1.1, is similar to the satellites of interest to the Air Force, and was thus the starting point for this research.

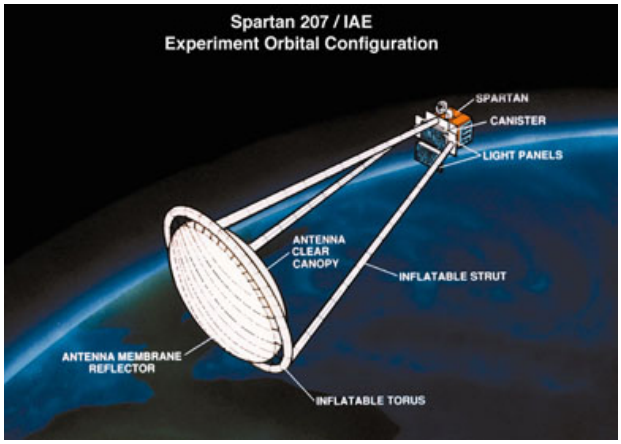

Figure 1.1: Spartan 207 Communications Satellite

1.3 Vibration of Space Structures:

Once inflated, these space structures are subject to two main types of vibrations. The first type is induced mechanically by onboard guidance systems or impacts with space debris. The guidance systems are gyroscopes that rotate continuously; by changing the rotational velocity one can cause the satellite to travel and point in different directions. However, no gyroscope can be made perfectly round and uniform in mass; therefore, vibrations caused by rotational imbalance, similar to those of a washing machine with an unbalanced load, are

inevitable. When the satellite impacts space debris and does not deflate, vibrations are caused in the same manner as a modal hammer impacting an metal plate or a drumstick hitting a cymbal; the motion of the objects is translated into an impact force applied over a very short period of time. The second type of vibration is induced from thermal effects due to variable amounts of direct sunlight as the satellite orbits about the earth. When the satellite comes into or out of direct sunlight, the temperature is changed so rapidly that large vibrations typically occur.

The membrane reflector is the most sensitive portion of the satellite to disturbance as it will not properly reflect signals if vibrations are present. Thus, controlling the vibration of the inflated torus becomes of key importance since it offers support to the reflector. Controlling these vibrations in spaced-based structures is critical to ensuring optimal performance. Since the satellite structure is made of Kapton®, a thin polyimide film, its structural stiffness is much lower than traditional engineering material such as steel and aluminum. Despite its low actuation authority compared to piezoceramics such as PZT (Lead Zirconate Titanate), PVDF is expected to be capable of applying the necessary forces required to control the compliant Kapton® film. Also, PVDF has a much greater sensitivity to mechanical strains than PZT when used as a sensor. Furthermore, active control using the "smart" piezoelectric polymer PVDF for sensors and actuators is a feasible option that deserves more investigation and modelling, as PVDF is highly flexible and ten times more compliant than PZT and easily conforms to the doubly curved surface of the torus.

Since little is known about the effects of such attachments on the vibration of membranes, the decision was made to initially focus on a coupon section of the inflated torus, rather than on the entire structure. Thus, this research focuses on

a flat, rectangular section of the satellite in the area surrounding a given PVDF patch.

1.4 Objective:

The objective of this research is to understand how PVDF patches alter the free vibration characteristics of thin, lightweight polyimide films and to assess the ability of the patches to act as sensors and actuator when modeled as a layered membrane system. Membranes are two-dimensional elements that are considered infinitely thin, thus having no inherent resistance to bending. A more detailed discussion of membranes is offered in Section 3.2. When small piezoceramic devices are attached to aluminum or steel structures, the effects of the active element on the dynamic properties of the host are typically ignored. However, when the host structure is a membrane, even lightweight PVDF could greatly change the mass and stiffness values in the area under and around the patch. Whether or not these alterations in material properties of the system significantly affect the dynamic properties of the structure is the primary focus of this document. A closed-form solution and approximation methods are used to determine the natural frequencies and mode shapes of a bare rectangular membrane. Only the approximation techniques, namely the Rayleigh-Ritz and finite element methods, are used to obtain results for a similar rectangular membrane with a PVDF patch. These methods are highly accurate and preferable when a closed-form solution is not readily available or even impossible. A comparison of the two systems is made to determine how much the piezopolymer sensor/actuator alters the dynamic characteristics of the rectangular coupon. Furthermore, the impact of increasing the patch area relative to the base layer is considered. Consequently, the amount of effort required to model the entire inflated torus structure with attached piezopolymer sensors and actuators will be understood. Also, the interaction between the base layer membrane and the PVDF patch is modeled in terms of sensing out of plane

displacements of the system and reducing such motion by altering the tension in the system.

1.5 Background

Even though using inflatable structures for space satellites is a relatively new concept, there are a fair number of groups working on various aspects of this emerging technology. This sections highlights some of the work being done on inflated structures as well as the vibration and control of thin membranes.

1.5.1 Vibration Analysis of Inflated Structures:

Even though the communication satellites of interest to this study are composed of inflated geometric sections, other industries are interested in such structures. For example, the auto industry has performed some analyses of tires by modeling them as toroidal membranes. Saigal and Yang [1986] used this approach to understand the free vibration characteristics of tires inflated to different pressures. They used both analytical and finite element methods to assess natural frequencies of flat, cylindrical and toroidal membranes. In general, the natural frequencies were found to rise as internal pressure of the tire was increased.

As far as space structures are concerned, Main et al. [1995] examined the dynamic properties of inflatable space structures composed of inflated tubes, struts or beams. Their analysis was based on a modified Euler-Bernoulli beam theory in which the structure can carry no load in compression because the inflatable tube would wrinkle and introduce non-linear terms. Small amplitude dynamic loads were then applied to predict the lowest natural frequencies. The damping was predicted to be two-fold, a viscous component due to motion through surrounding air and compression of the enclosed gas, and a strain rate component due to stretching of the beam fabric. Experimental modal analysis

was then performed on an inflated cantilevered beam, in both ambient and microgravity conditions, to verify the analytical results and indicate the material moduli, natural frequencies and distributed damping coefficients. It was found that the first few mode shapes were the same as for a solid elastic beam. Also, the modulus was found to vary greatly between static and dynamic loading conditions. Furthermore, viscous damping of the inflated structure did not depend on the internal pressure; however, the strain rate damping decreased as the pressurization stress levels in the fabric rose. There was also higher damping noted in microgravity test conditions as the only loading present was due to the internal pressure of the beam, resulting in an even distribution of the fabric rather than wrinkling that tends to occur in ambient tests.

Engineers at the Dynamics Test Branch at NASA's George C. Marshall Space Flight Center in Alabama performed a modal analysis of the Solar Orbital Transfer Vehicle (SOTV) under ambient conditions [Coleman 1998]. The results of their experiment were compared to a similar test performed in a vacuum and used to verify a finite element model of the satellite. Using a random input shaker and laser vibrometers, they found 10 resonant frequencies and corresponding mode shapes and damping ratios below 50 Hz for excitation in the plane of the reflector and 12 such modal parameters for excitation perpendicular to this plane.

Researchers at the University of Kentucky performed a modal analysis of an inflated thin-film torus structure [Griffith and Main 2000]. They used a modal hammer to excite the structure and low-mass accelerometers to record the accelerations at various points on the torus. As was the case with the NASA experiment mentioned previously, excitation was provided both in the plane of the torus and the perpendicular direction. The first three in-plane and out-of-plane bending modes were identified for internal pressures of 0.8 and 1.0 psig.

All of these modes occurred below 80 Hz and displayed between 0.9 and 6.9% damping. The test performed under higher internal pressure tended to cause higher natural frequencies but lower damping ratios.

As mentioned previously, scientists at the Air Force Institute of Technology in Ohio are also working on various aspects of inflatable satellites. In a preliminary experiment, the ability of PVDF to excite an inflated torus structure for modal analysis was studied [Agnes and Rogers 2000]. An inflated torus structure was constructed from a kiddy pool. While not being a precise inflatable structure, its ultra-low cost was crucial to this preliminary experiment in which bonding techniques for the PVDF could be understood without damage to expensive components. In order to assess the capability of the PVDF to excite the structure, modal analysis was performed on the torus using first an electrodynamic shaker and then a PVDF patch for input motion. These two methods were compared to each other as well as to a finite element model of the test article created in I-DEAS. The finite element software predicted some but not all of the modes observed experimentally. The modes that were not predicted likely corresponded to pendulum modes and in–plane motion of the experimental torus. The torus excited with PVDF produced frequency response functions similar to that of the shaker. Also, pendulum modes of the suspended structure predicted by the finite element analysis matched the PVDF excited test article, while the shaker excitation resulted in a different frequency. In summary, this experiment showed that PVDF can be used to excite inflated structures for modal testing; however, further work is needed to better model such structures and develop experimental methods so that modal parameters are more readily extracted.

1.5.2 Vibration of Membranes:

The focal point of this work is to understand the difference in dynamic properties between a bare membrane and one with a PVDF patch. Therefore, a great deal of literature dealing with the vibration of various types and configurations of membranes was consulted. The equation of motion for a flat, homogeneous, rectangular membrane with uniformly applied tension is derived in many locations, for example Rayleigh [1945], Meirovitch [1967] and Rao [1990]. This differential equation is presented, solved and applied in almost all vibration texts, Inman [1996] for example. However, the simplifications made in order to arrive at such solutions are violated in many real-life applications. Many practical uses of membranes result in inhomogeneous conditions. Material inhomogeneities of a membrane typically result from variations in its mass per unit area, which could be a result of varying thickness or material density. They can vary continuously or discontinuously and can be a function of direction or location in the membrane. In addition, inhomogeneity can be attributed to tension applied to a membrane that varies in different directions [Masad 1996]. This situation is clearly not related to the material, but rather a loading inhomogeneity. Nevertheless, any source of inhomogeneity significantly increases the complexity of the equation of motion derivation and solution over that which is presented in standard vibration textbooks. Below, some relevant work in the area of nonhomogeneous membranes is reviewed.

Rayleigh considered the free vibration of square and circular membranes with a point mass attachment in his book *The Theory of Sound* [Rayleigh 1945]. Using an estimation technique, he found formulae for the natural frequencies of such loaded membranes. However, his approximation only used one term of what would come to be called the Rayleigh-Ritz method.

In his paper, Langley [1995] claims that the equations for natural frequencies developed by Rayleigh are invalid. Since the point mobility of a membrane has an infinite imaginary component, any inertial force created by an attached point mass would lead to an infinite displacement at that point. Clearly this is not the case; however, it was found that large deformations do take place around the attachment that can only be represented by a multi-term Rayleigh-Ritz method. With this approach, Langley presents solutions for the free vibration of a circular membrane with a point mass attachment as well as the forced response of a square membrane with a point mass attachment using the modal summation method. The results are used to understand the physical limitations of linear membrane theory with point mass attachments. In order to obtain more accurate results, he suggests the use of a nonlinear theory, considering the attachment to have a finite area or taking into account the finite bending stiffness of the membrane (i.e., plate theory).

A square membrane under uniform tension with a centrally located circular area of finite radius and either continuously or discontinuously varying density was considered by Bambill, et al. [1997]. He determines the natural frequencies using both the Optimized Rayleigh-Ritz method and an approximate conformal mapping approach. Reasonable agreement is seen between the two methods for the discontinuously varying density. Likewise, acceptable results are obtained for the square membrane with circular center section of continually varying density.

Masad [1996] studied a rectangular membrane with uniform tension and thickness, but with linearly varying density along one dimension of the membrane. Solutions to natural frequencies and mode shapes were obtained using both a numerically accurate analytical technique and approximation methods for the inhomogeneous membrane. The resulting frequencies and

mode shapes were compared to those of an equivalent, homogeneous membrane. As expected, some variation was seen between the two types of membranes and the approximate method was able to closely predict the natural frequencies.

Of particular interest to the present study, Pronsato et. al. [1999] considers a rectangular membrane under uniform tension with a rectangular center section having a constant density different than the rest of the structure. Again, approximation techniques are used to find the frequency coefficients, from which natural frequencies can be extracted. The approximation was made possible by using a truncated Fourier series consisting of a linear combination of sine waves to approximate the displaced shape of the vibrating membrane. The results are tabulated for different ratios of density between the outer and inner areas as well as different dimensions of the inner rectangular section. Finally, good correlation is seen when the results are compared to a previous paper in which only one polynomial expression was used to represent the displacement of the membrane. It can be shown that results attained by Pronsato are even more accurate than those of the previous paper.

1.5.3 Piezoelectricity:

From their study of crystal structures, Pierre and Jacques Curie discovered the piezoelectric effect in 1880. Piezoelectricity, whose prefix *piezo-* is derived from the Greek word for *to press*, is an interaction between electrical and mechanical systems. The direct or generator piezoelectric effect is when a material produces an electrical polarization in response to an applied mechanical stress. In contrast, the converse or motor piezoelectric effect occurs when a material develops a mechanical strain in response to an applied electric field [Ikeda 1996]. This ability to react to its surroundings has lead to monikers such as "active" or "smart" materials. In the 120 years since its discovery, piezoelectricity has

become a well-defined science. As a result, there is a vast body of literature dealing with this phenomenon. The ones that found extensive application to the current work are reviewed herein.

In the work from which his Master of Science thesis arose, Collins et al. [1990] provided a brief but informative history of piezoelectricity and some of the basic physical properties and mathematical relationships used in the study of piezoelectric materials. The fact that other noncrystalline materials, such as wood, bone and some polymers, exhibit piezoelectric behavior is discussed. In particular, the discovery of the piezoelectric effect in polyvinylidene fluoride (PVDF) is presented. In its unpolarized form, PVDF is a clear, lightweight and tough yet highly flexible film that is often used as a passive protective coating for many surfaces due to its high resistance to various chemicals and ultraviolet light. After suitable processing consisting of stretching at high temperatures, exposure to high electric fields during cooling (poling) and surface metallization, PVDF can be used as a sensor and/or actuator for active structural control. After the outstanding introduction to the history, manufacturing and application of piezopolymers, Collins et al. proceeds to model and experimentally verify the use of PVDF as modal sensors and spatial filters for various mechanical systems.

Hagood, Chung and von Flotow [1990] presented a more detailed consideration of the interaction between an elastic structure and piezoelectric actuators used for active structural control. Also, they developed state space models for voltage and current-driven piezoelectric devices and assessed how the dynamics of the actuator and passive electrical network influence the overall system dynamics. These models are used to predict the behavior of a cantilevered beam with surface-mounted piezoceramic devices. Lastly, open- and closed-loop control experiments were performed to verify the analytical models, thus showing significant effects of the electrical circuit on the beam dynamics.

Crawley and de Luis [1987] developed analytical models to predict the static and dynamic response of intelligent systems to an applied voltage. These models were applicable to systems with segmented piezoelectric actuators that are either bonded to an elastic member or embedded in a laminated composite structure. They also consider perfect bonding conditions between the actuators and the structure as well as bonds of finite thickness and stiffness. The models were used to select an optimal location for actuators. With a PZA consisting of two piezoceramic actuator devices bonded at equal but opposite distances from the neutral axis of the beam, three experimental systems were constructed: an aluminum beam with two surface-mounted PZAs, a glass-epoxy beam with two PZAs and a graphite-epoxy beam with one PZA. The PZAs were used to excite steady-state resonant vibrations in the beams and the experimental responses were seen to agree with the analytical models. Static tests performed on the glass-epoxy laminated material with embedded PZAs showed a reduction in ultimate strength of only 20% and no significant change in the global elastic modulus of the composite laminate.

Kulkarni and Hanagud [1991] developed an electromechanical model for a combined generic three-dimensional, isotropic, linearly elastic body and piezoelectric body undergoing small or large deformations using a variational formulation. The model is then used to develop a two-dimensional finite element formulation to predict the static and dynamic response of the system to applied voltages that vary with time and spatial distribution on the surface of the patch. A detailed treatment of the electromechanical coupling between the active element and the elastic body is presented. The stresses and strains predicted by the static analytical model were verified using a cantilevered aluminum beam with piezoceramic patches bonded to the top and the bottom surfaces. The same beam was used to verify the dynamic response of the system to various types of applied voltages. It was found that electric fields applied to the actuators in a

nonuniform manner, such as a linear, cosine or exponential variation along its length, result in different types of bending moment distributions being applied to the beam.

Banks, Smith and Wang [1995] examined the interaction between piezoelectric actuators on such structures as beams, plates and more complicated shell structures such as a right circular cylinder. The changes in mechanical stiffness of the structure due to the attachments were studied in addition to the ability of the patches to apply forces and moments, which were found to depend on the geometry and placement of the patch in addition to the applied voltage. The influence of internal forces and moments due to the structure and the actuator as well as those due to actuating the patch are then related to the time-dependent structural equations of motion. With that, these models can be applied directly to controlling the vibration of such structures, particularly those of a curved nature. Since the structure at the focus of this research was a toroidal shell, the results from Banks, Smith and Wang will contribute greatly when control of the entire inflated member is considered.

Some work has been done on using piezopolymer materials to control the vibrations of membranes. Niekerk and Tongue [1995] investigated ways to actively reduce the transient noise transmission through a membrane covering a circular duct. Once the nature of the sound has been identified, only a few milliseconds are available to determine the control signal and actuate the structure. Therefore, piezopolymer actuators were used because they offer the ability to operate at high frequencies. Their experiment used a speaker to impart sound waves into a duct whose cross-section is covered by an elastic membrane fitted with discreet piezopolymer (PVDF) actuators. The sound pressure imparted to the film was measured immediately before the membrane by a microphone. The resulting velocity of the center of the membrane was measured

with a laser vibrometer, whose output was used as a feedback signal for the control loop. The output of this control loop was given to the PVDF actuators attached to the membrane. The resulting sound pressure level was measured at a microphone on the side of the membrane opposite the speaker. Three control schemes were investigated analytically, and then experimentally, namely optimal control, sliding control and velocity feedback control. It was found that a reduction in transient noise transmission through the membrane was possible. Experimental results confirmed this analytical prediction. The PVDF actuators performed fast enough to control the membrane and velocity feedback was found to be the most stable and easily implemented control method.

This experiment by Niekerk and Tongue suggests that active control using piezopolymer actuators could be possible for the thin inflatable satellite at the focus of the current research. However, many actuators would be needed and the impact of these many actuators on the dynamics of the structure needs to be and is assessed in this work.

1.6 Overview of Thesis:

This first chapter introduces inflatable satellite technology, the need for such structures and some of the problems associated with their use and proper functioning. Section 1.5 discusses work that has already been done in the area of inflatable structures, membrane vibrations and piezoelectric materials. Disturbances caused by structural vibrations are noted as the particular concern of this work, and sources of such vibrations are presented. In an attempt to actively control these vibrations, the use of piezopolymer sensors and actuators are considered, as are the effects of such components on the dynamic properties of the inflated satellite. As this is preliminary work for studying such effects on the entire torus structure, research will commence at the coupon level. A

comparison of two flat, rectangular coupon sections of the satellite, one bare and one with a PVDF attachment has been selected as an adequate starting point.

Chapter 2 deals with developing and understanding the effects of internal pressurization on the Kapton® material. This pressure causes stresses to be developed in the film, and these stresses are essentially the forces that form the tension in the membrane. Since the torus is cylindrical, these stresses are different in two orthogonal directions. Since membranes have no bending resistance, the only force available to restore a displaced membrane to its plane of equilibrium is this tension; understanding how this tension is developed is a key element to understanding how the membrane vibrates. This pressure vessel stress analysis concludes with an equivalent tension system shown on the rectangular coupon of interest to this study.

Chapter 3 is devoted to the closed-form solution of bare membrane vibrations. It begins by discussing what constitutes a membrane in the context of other types of structural elements. Then, applying the tension loads developed in Chapter 2, Newton's Method is used to derive the differential equation of motion for the coupon without the PVDF patch. This boundary value problem is solved in closed form to find the exact natural frequencies, mode shapes and total solution of a membrane with fixed edges.

Chapter 4 uses the Rayleigh-Ritz and finite element methods to approximate the natural frequencies and mode shapes of the bare membrane with direction dependent tensions. The commercially available software package ANSYS was employed to develop the finite element model and solve for the dynamic properties of interest. A numerical comparison is made with the closed form solution in order to verify the accuracy of these approximation techniques. Once the Rayleigh-Ritz and finite element methods are seen to closely approximate the

closed-form solution, they will be expanded to analyze a more complicated system, a membrane with a passive PVDF patch attachment.

Chapter 5 uses the approximate methods validated in Chapter 4 to analyze a similar membrane with a passive PVDF attachment. Energy methods are used to develop the equation of motion and the Rayleigh-Ritz method is then used to approximate the natural frequencies and mode shapes of this layered membrane system with its piezoelectric attachment. However, it is found that membrane theory does not allow one to account for the added stiffness of the patch. In contrast, membrane theory can handle only the mass added to the system by the PVDF attachment. A finite element model using membrane elements is constructed in ANSYS to support the approximation made using the Rayleigh-Ritz method. The results of these two methods are shown to agree quite well, further substantiating the claim that membrane theory has severe limitations in terms of representing the true effects of the patch.

Chapter 6 considers the same membrane with a PVDF attachment that is analyzed in Chapter 5, however; the piezoelectric behavior of the patch is now considered. It is shown that traditional membrane theory does not allow the patch to be used as a sensor for the dynamic response of the base layer. Even though static measurements of stress and strain due to internal torus pressure could be made, piezoelectric sensors make poor static measurement devices as they lose charge quickly. However, voltage can be applied to the patch to vary the tension in the membrane. Understanding how the PVDF actuates the base layer in response to an applied voltage will lead to further work in the area of using active control to suppress membrane vibrations.

Chapter 7 presents the results of the various methods used in Chapters 3 through 6. The first few mode shapes of the bare system are presented for completeness,

and the differences between bare and layered membranes are discussed. Effects of changing the patch size relative to the base layer are also presented. In addition, relationships between the patch thickness and natural frequencies of the layered system are predicted. Also, practical limitations for the model of the interaction between the patch and membrane base layer presented in Chapter 6 are presented. A list of contributions from this work is specified and the thesis concludes with recommendations for further work and a discussion of how these results can aid in the development of a model of the inflated torus and then the inflated satellite.

Chapter 2

Analysis of the Prestress Condition

2.1 Introduction:

The basic premise behind inflatable space-based satellites is that a gas is pumped into the structure so that the intended shape is assumed and maintained. This method is reliable and allows large structures to be launched in the payload bay of a Space Shuttle Orbiter. Meanwhile, the pressure used to inflate and sustain the satellite causes tensile stresses to develop within the material.

Since the space environment is a vacuum, the pressure inside of the torus is both an absolute and a gage pressure reading. Typical inflatable devices used by NASA and the U.S. Air Force pump inert nitrogen gas into the satellite until a pressure on the order of one pound per square inch is reached. For typical toroidal geometries, the stresses that develop from this pressure are much lower than the yield strength of Kapton®, thus failure of the satellite material is not a primary concern. However, these stresses do influence the vibration response of the satellite. For this research effort, a coupon of satellite material will be modeled as a flat, rectangular membrane. Since membranes theoretically have

no bending stiffness, the only forces that tend to restore an equilibrium condition during vibration are caused by tension within the material. To understand how the material of the satellite vibrates, it is first important to assess the state of stress caused by the internal pressure of the torus. Thus, Chapter 2 focuses on determining these stresses, selecting an appropriate portion of the torus to analyze and finally determining how the stresses relate to tensions required for the membrane vibration equation.

2.2 State of Stress in Pressure Vessels:

Cylindrical pressure vessels are common structures that engineers wish to analyze. Some common examples are gas storage tanks, pipes, soda cans and steam boilers. A right circular cylindrical shell is a general type of pressure vessel often used to develop stress and strain equations for such structures. Figure 2.1 shows this type of shell, where t is the thickness, r_1 is the inner radius, r_2 is the outer radius and p is the internal pressure of the tube.

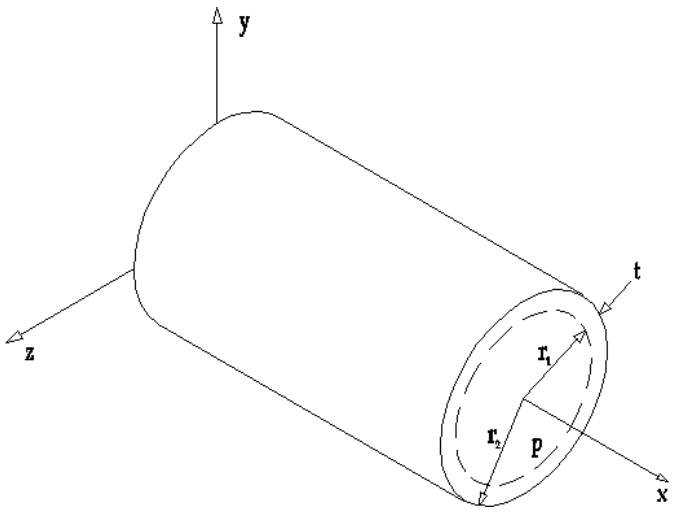

Figure 2.1: Cylindrical Pressure Vessel

2.2.1 Thick-Walled Pressure Vessels:

Oftentimes, the application of the structure, such as high-pressure boilers, dictates that the wall thickness be considerable in order to operate safely. When

the thickness is substantial with respect to the radius of the vessel, thick-walled pressure vessel theory must be used to analyze the state of stress in the walls. For tubes with "thick" walls made of a linear-elastic material, closed ends, and a uniform internal pressure, there exist three orthogonal principal normal stresses, namely, tangential, longitudinal and radial, denoted σ_t, σ_l and σ_r, respectively. Longitudinal stress, parallel to the longitudinal axis of the cylinder, is uniform over the thickness of the wall and develops to resist the force caused by the pressure against the end caps. The formula for longitudinal stress is given in Eq. (2.1) as

$$\sigma_l = \frac{p r_1^2}{r_2^2 - r_1^2} \tag{2.1}$$

Tangential stress is perpendicular to the longitudinal stress in a plane tangent to the cylinder at the point of interest. It is also known as *hoop stress* in reference to the stress in a metal hoop used to hold wooden barrels together. Tangential stress is found by the following expression:

$$\sigma_t = \frac{p r_1^2}{r_2^2 - r_1^2}\left(\frac{r_2^2}{R^2} + 1\right) \tag{2.2}$$

Unlike the longitudinal stress, the tangential stress varies as a function of radial location, R. The internal pressure tends to cause a compressive stress in the tube wall in the radial direction. The formula for this radial stress is given in Eq. (2.3) as

$$\sigma_r = -\frac{p r_1^2}{r_2^2 - r_1^2}\left(\frac{r_2^2}{R^2} - 1\right) \tag{2.3}$$

As was the case for tangential stress, the radial stress also varies as a function of radial location, R. As mentioned earlier, the radial stress is always compressive, as indicated by the minus sign in Eq. (2.3). Both the tangential and radial stresses assume their greatest absolute values at the inner wall, when R equals r_1. The radial stress varies in a quadratic manner from $-p$ at the inner wall to zero at the outside surface. Likewise, the tangential stress varies in a quadratic manner

from a maximum value at the inner wall to a minimum value at the outside surface. The reader is referred to Shigley and Mitchell [1993] for a formal derivation of thick-walled pressure vessel theory.

2.2.2 Thin-Walled Pressure Vessels:

The three equations above for thick-walled pressure vessels with internal pressure are rather cumbersome; by making a few simplifying assumptions, a set of equations can be developed that are easier to use while still having a high degree of accuracy for certain pressure vessel geometries. These simplified equations are known as thin-walled pressure vessel theory. When the ratio of the wall thickness to the inner radius is less than one-tenth, the radial stress is typically much lower than the resulting tangential stress. In this case, the radial stress is assumed to be zero, because it would vary from a small value, with respect to the tangential stress, at the inner wall to zero at the outer wall. One then also presumes that the tangential stress is constant through the thickness of the tube. If a vessel meets these restrictions, thin-walled theory can be used to obtain stress values to within 5% of the thick walled-theory [Dowling, 1999]. From the description of the satellite of interest in Chapter 1, the ratio of t/r_1 is approximately 0.001, well within the restriction for thin-walled theory. With that, thin-walled pressure vessel theory will now be developed and subsequently used for the inflated torus.

Similar to thick-walled pressure vessels, thin-walled right circular cylinders with internal pressure and end caps also have longitudinal and tangential stresses. One can begin to develop equations for these stresses by slicing the cylinder in Figure 2.1 along the *x*-*y* plane and considering a differential length of the cylinder, *dx*. Summation of forces can be used on the remaining free body diagram, shown in Figure 2.2, to determine the tangential stress, σ_t.

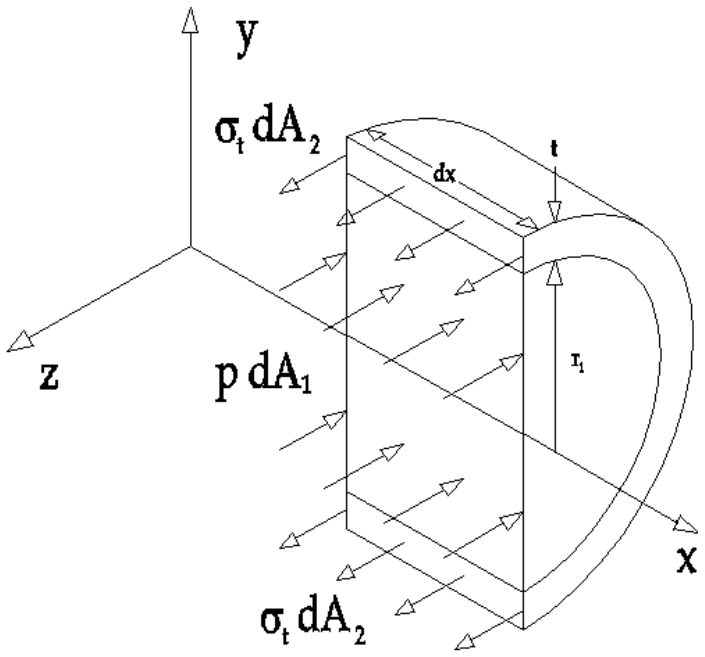

Figure 2.2: Free Body Diagram for Determining σ_t

From Figure 2.2, it is clear that σ_t is applied over two sections of A_2, which is equal to tdx. Also, the pressure, p is applied over the area A_1, which is a projection of the inner wall onto the x-y plane and equal to $2r_1dx$. Summation of the forces in the z direction yields

$$\sum F_z = 0: \quad 2\sigma_t (t\,dx) - p(2r_1\,dx) = 0 \tag{2.4}$$

From Eq. (2.4), σ_t is shown to be

$$\sigma_t = \frac{pr_1}{t} \tag{2.5}$$

At this point, it should be noted that Eq. (2.5) gives the tangential stress at the inner wall, where it is a maximum. For thin-walled theory however, it has been assumed that this value of tangential stress has no variation in the radial direction. A similar summation of forces in the x direction yields the expression for the longitudinal stress, assuming the ends of the cylinder are capped. Slicing the cylinder in Figure 2.1 on a plane parallel to the y-z plane gives the free body diagram shown in Figure 2.3.

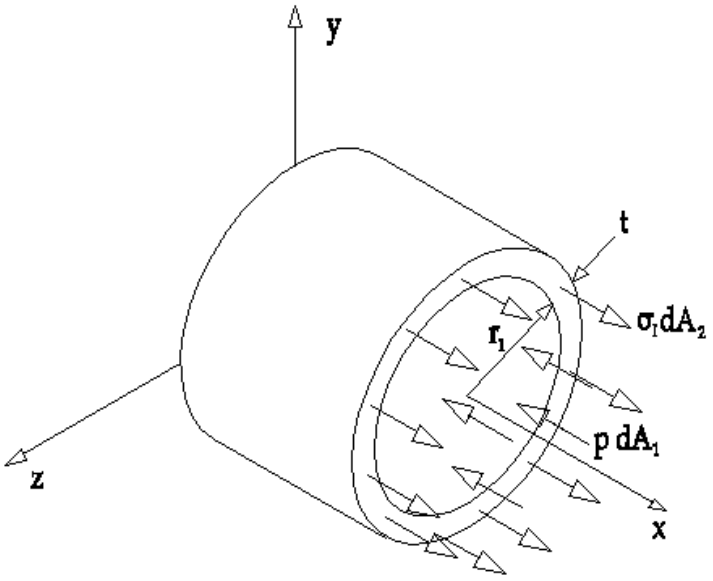

Figure 2.3: Free Body Diagram For Determining σ_l

From Figure 2.3, it is clear that σ_l is applied over A_2, which, for thin-walled theory, is approximated by the circumference of the tube at the inner wall times the wall thickness. That is, $A_2 = 2\pi r_1 t$. Furthermore, the internal pressure p is applied to the end caps over an area A_1, which is equal to πr_1^2. With these two areas defined, summation of the forces in the x direction is straightforward.

$$\sum F_x = 0 : \sigma_l (2\pi r_1 t) - p\pi r_1^{\,2} = 0 \tag{2.6}$$

From Eq. (2.6), σ_l is found below:

$$\sigma_l = \frac{pr_1}{2t} \tag{2.7}$$

This equation shows that the longitudinal stress in the wall is half the value of the tangential stress. With Eq. (2.5) and Eq. (2.7), one can approximate the stresses in a closed, thin-walled cylinder with an internal gage pressure at the inner wall. The result is a state of plane stress at the point of interest on the outer surface. These stresses are also two of the principal stresses if there is no load that would cause shearing stress in this plane. Of course, the third principal stress, σ_r, is zero at all points on the outer wall.

2.3 Inflated Toroidal Shells:

Even though an inflated torus and a cylindrical shell do not look much alike, the effects of an internal pressure on the structure are quite similar. In fact, a cylindrical shell can be considers a torus with an infinite radius of revolution, and at a specific radial location on the torus, the state of stress is identical to that calculated from Eq. (2.5) and Eq. (2.7). However, the values of stress depend on the geometry of the torus. Figure 2.4 shows half of the torus structure with the geometric properties defined.

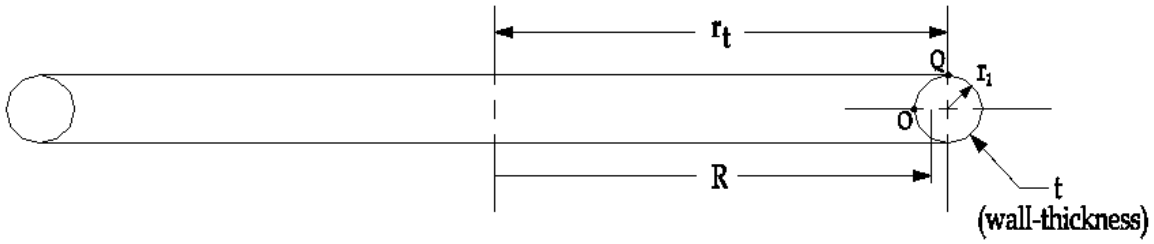

Figure 2.4: Torus Geometry

From Figure 2.4, one sees that the radius of revolution of the toroidal shell is denoted r_t while the wall thickness is represented by t. The radius of the tube is r_1, and since this torus is considered a thin-walled structure, r_2 is not defined, because their numerical values are considered equivalent. Lastly, the symbol R is used to represent a variable distance to a point of interest on the torus in the radial direction.

The stresses developed in the torus material lay in a plane that is tangent to the structure at the point of interest. A longitudinal stress develops as a result of the internal pressure, and is given by the same formula as for the circular cylinder with end caps. A tangential stress also develops as a result of the internal pressure and is similar to the tangential stress component for the circular cylinder, only for the torus, the tangential stress is a function of the radial

distance *R*. Figure 2.5 shows an arbitrary point of interest and a differential element on which these two stress components act.

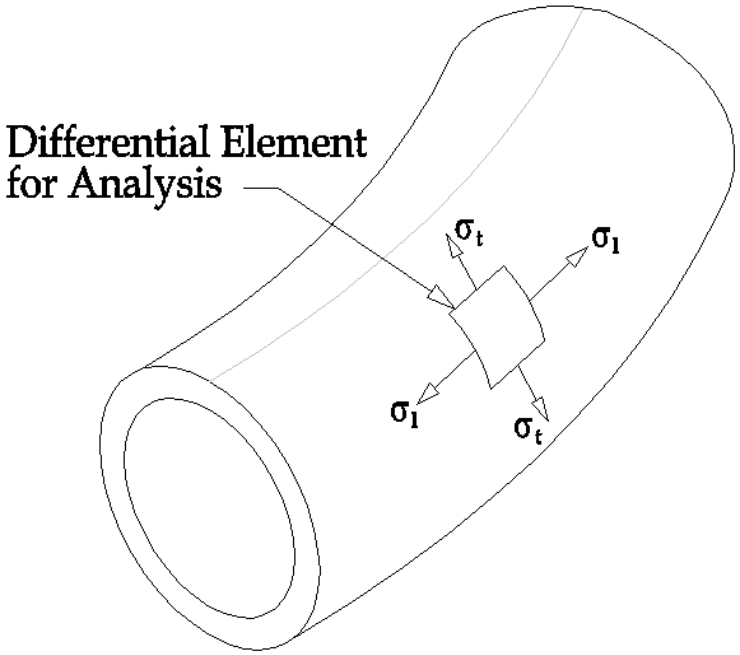

Figure 2.5: Differential Element of Torus With Stress Components

The stress in the longitudinal direction is given by Roark [1975] to be

$$\sigma_l = \frac{pr_1}{2t} \tag{2.8}$$

This equation is identical to Eq. (2.7), which stands to reason as longitudinal stresses develop as a result of the closed nature of the torus or tube and are neither dependent on the geometry of the structure nor the radial location. However, the difference in shape between the tube and the torus does affect the expression for the tangential stress, which is [Roark, 1975]

$$\sigma_t = \frac{pr_1}{2t}\left(\frac{R+r_t}{R}\right) = \sigma_l\left(\frac{R+r_t}{R}\right) \tag{2.9}$$

Clearly from Eq. (2.9), the tangential stress varies along the radius of revolution of the torus. When R is equal to r_t, the term in parentheses in Eq. (2.9) becomes two and the expression for σ_t simplifies to Eq. (2.5). At this radial location, denoted as point Q in Figure 2.4, the state of stress calculated from Eq. (2.8) and

Eq. (2.9) is identical to that of a cylinder with the same radius, internal pressure and wall thickness.

2.4 From Differential Element to Rectangular Coupon:

Eq. (2.8) and Eq. (2.9) define the state of stress at a given point on the torus. However, now consider the differential element in Figure 2.5 to be a flat, rectangular element with finite area and tangent to the torus at a point. The state of stress at that point of tangency is approximately the state of stress applied to the flat, rectangular element, shown in Figure 2.6. Note that since a plane element is now under consideration, a Cartesian coordinate system has been adopted in place of the longitudinal-tangential coordinates of a cylinder. Thus, σ_l and σ_t become σ_x and σ_y, respectively.

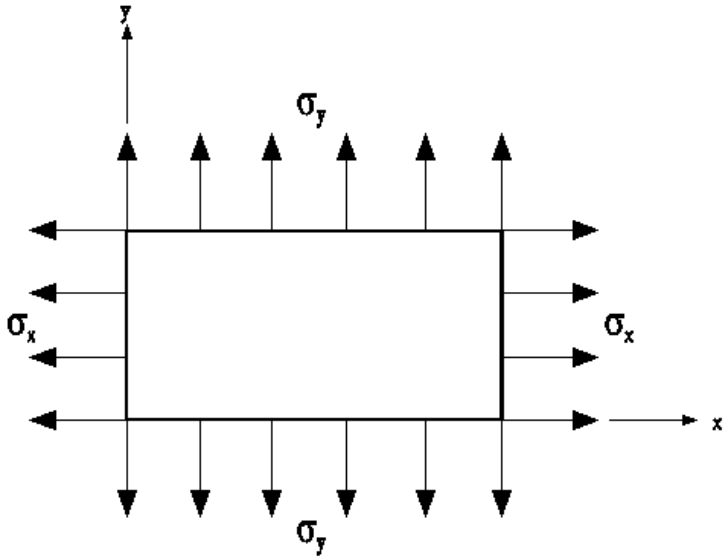

Figure 2.6: State of Stress on Rectangular Element Tangent to a Point on Torus

These stresses are responsible for the initial tension present in the membrane. The net forces resulting from these stresses are used in Chapter 3 to derive the equation of motion for this membrane. Whereas these forces could be easily found by multiplying the stress by the area over which it is applied, membrane vibrations require tension quantities, that is, with units of force per unit length of

membrane boundary. This is easily done by multiplying the stress by the thickness of the membrane, *t*, as show:

$$\begin{aligned} P_x &= \sigma_x t \\ P_y &= \sigma_y t \end{aligned} \tag{2.10}$$

However, using Eq. (2.8) and Eq. (2.9), the tensions in the *x* and *y* directions can be written in terms of the geometric properties of the torus. With that, Eq. (2.10) becomes

$$\begin{aligned} P_x &= \frac{pr_1}{2} \\ P_y &= \frac{pr_1}{2}\left(\frac{R+r_t}{R}\right) = P_x\left(\frac{R+r_t}{R}\right) \end{aligned} \tag{2.11}$$

From Eq. (2.11), one notes that the tensions are not a function of the wall thickness. For a given torus, the value of r_t is known, so for a given radial location *R* on such a torus, the term inside the parentheses in Eq. (2.11) is a constant. Thus, there exists a proportional relationship between the tensions in the *x* and *y* directions as depicted:

$$\begin{aligned} P_y &= \kappa P_x \\ &where\ \kappa = \left(\frac{R+r_t}{R}\right) \end{aligned} \tag{2.12}$$

This proportional relationship between the *x* and *y* tensions is critical to the derivation of the equation of motion for a rectangular membrane with tensions that vary with direction in Chapter 3. It is interesting to note that this proportional relationship depends solely on torus geometry and radial location. The wall thickness, radius and internal pressure do not affect the relationship between tensions in different directions. Figure 2.7 shows the unequal tensions applied to a rectangular membrane. This figure will be referred to throughout this work as these tensions are used not only in Newton's Method in Chapter 3, but also in the energy method formulations in Chapter 4 and Chapter 5. They also contribute a great deal in Chapter 6 when the effects of patch actuation are considered.

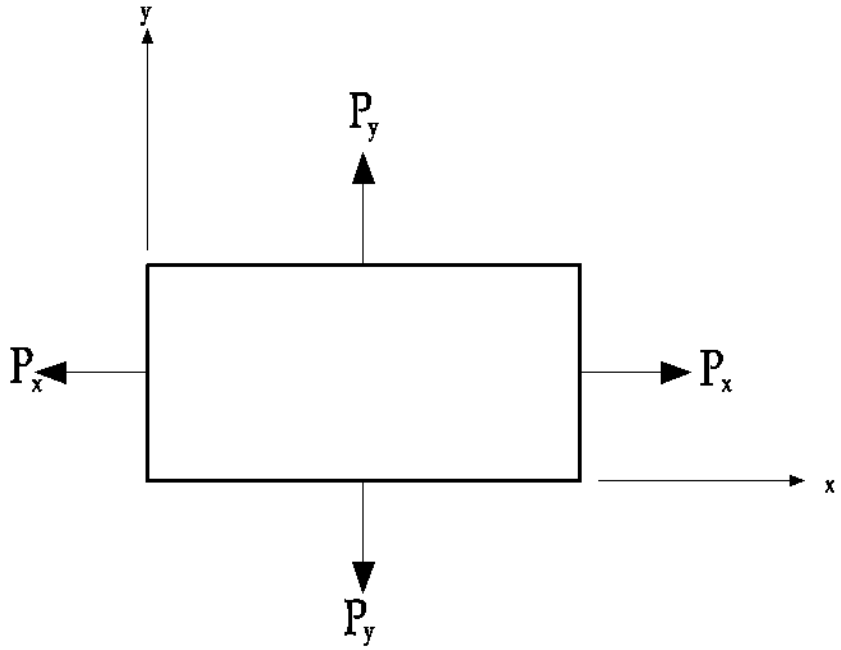

Figure 2.7: Unequal Tensions on Coupon Boundaries

2.5: Summary:

Chapter 2 discusses the stresses that develop in the walls of both thick- and thin-walled pressure vessels. Since the toroidal shell used on the satellite of interest is constructed of extremely thin Kapton® film, thin-walled pressure vessel theory was used to express the state of stress developed in the torus wall. A coupon of material was chosen around a particular point of interest and the formulae for stress were then used to determine expressions for the tension applied to the coupon boundaries. These tensions were noted to have a simple, proportional relationship based only on torus geometry. In Chapter 3, these tensions are used as a basis for deriving the equation of motion for a bare rectangular membrane section of the torus. In Chapters 4 and 5, these tensions are used to formulate the equation of motion for the bare membrane and layered membrane from an energy standpoint. For the layered system consisting of the base coupon layer and a PVDF attachment, the tensions found in this chapter are considered to still be valid far away from the PVDF patch in Chapter 6, where the piezoelectric behavior of the attachment is considered.

Chapter 3

Closed-Form Solution to Bare Membrane Vibrations

3.1 Introduction:

Chapter 2 discusses thin-walled pressure vessel theory that was developed and used to determine the state of stress at any point on a thin toroidal shell, which represents the inflated torus section of the satellite in Figure 1.1. The formulated state of stress at a given location was then used to determine the tension applied to coupon boundaries with the results being presented in Figure 2.7. As mentioned previously, these tensions are the only source of load available to restore the coupon to its flat equilibrium position. Chapter 3 discussed how these tensions are used to derive the equation of motion by modeling the coupon as a flat, rectangular membrane, which is considered to have no bending stiffness. This equation of motion and fixed boundary conditions define a boundary value problem that will be solved in closed form using the separation of variables method to produce a total solution. Additionally, equations for the natural frequencies and mode shapes are presented.

3.2 Distributed Mass Systems and the Membrane Approximation:

A membrane is an extremely thin sheet of material that, for the purposes of this research, lies in a plane while in its equilibrium state. A membrane is also considered to be a two-dimensional, distributed mass system. The two-dimensional aspect requires that the motion of the membrane be described by two spatial variables, such as x and y in a Cartesian coordinate system or r and θ for a polar coordinate system. For the purpose of this project, only out-of-plane displacements will be considered. The motion also depends on time, which is intrinsic to the study of vibrations. Furthermore, unlike one-dimensional systems, the shape of the boundary plays a role in determining the vibration characteristics of the membrane. The distributed mass aspect distinguishes this type of system from elementary vibration models that consider a mass to be concentrated at a single point. A simple concentrated mass system is shown in Figure 3.1.

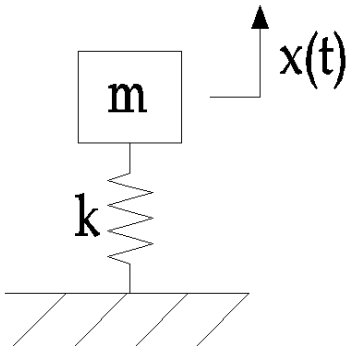

Figure 3.1: Single Degree of Freedom, Concentrated Mass System

The one-dimensional counterpart of a membrane is a string, which has mass distributed along its length and negligible bending stiffness. A string that cannot be assumed to have zero bending stiffness is referred to as a beam. Since a string is a one-dimensional system, the displacement is only a function of one spatial variable, location along its length. A diagram showing the general parameters of

a string, with length L, constant tension P, fixed ends, vertical motion $y(x,t)$ and subjected to the forcing function $f(x,t)$ is shown in Figure 3.2.

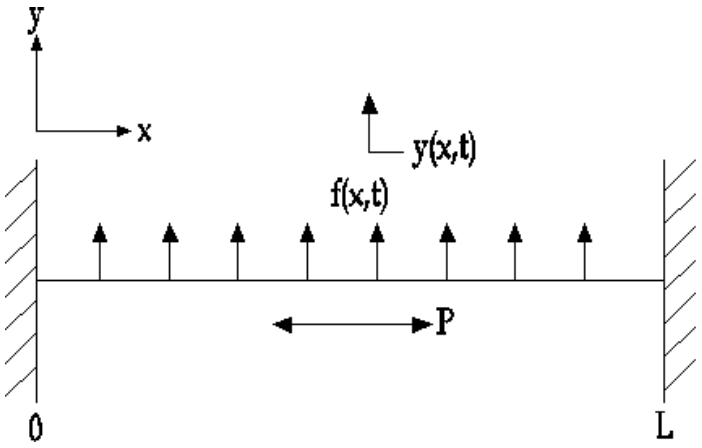

Figure 3.2: General Vibration Model of a String

Since a membrane is thin, it offers very little resistance to bending, thus any effects of bending stiffness are considered negligible. This simplification can be understood quantitatively if one considers the cross-section of a membrane as shown in Figure 3.3.

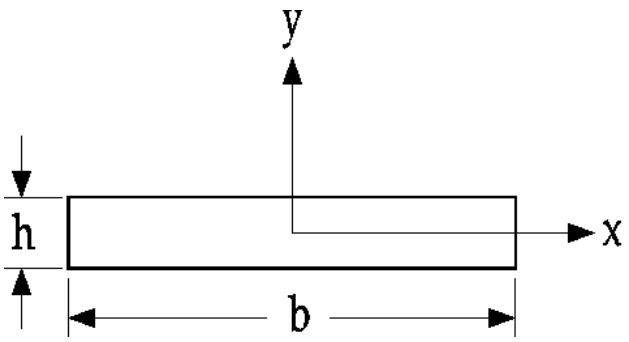

Figure 3.3: Cross-Sectional Area of Membrane

The measure of bending stiffness for a plate is the flexural rigidity D where

$$D = \frac{E h^3}{12(1-\nu^2)}$$

$$\text{where } E = \text{Young's Modulus and} \qquad (3.1)$$

$$\nu = \text{Poisson's ratio}$$

Clearly, as h becomes small, its cubic relationship drives D to zero quickly. If the Kapton® rectangular membrane selected for numerical analysis in Chapter 4, with E=370000 psi, h=0.003 inch and ν=0.34, is considered to be a thin plate, one quickly calculates from Eq. (3.1) that D for this member would be approximately 9.413×10^{-4} lb-in. However, if the thickness h were one inch, D would be 3.49×10^{4} lb-in. Since the first D is so small, it is clearly reasonable to use membrane theory, thereby neglecting the effects of bending stiffness. Of course, a membrane that is so thick that it has a significant bending stiffness is called a plate. A membrane is essentially a two-dimensional version of a string and possesses the same relationship to a plate that a string does to a beam. Some common objects that are often modeled as membranes are eardrums, drumheads and soap films.

3.3 Membrane Without PVDF Patch:

To begin a simulation of membrane vibrations, one begins with a thin, flat material of arbitrary shape under some initial tension. Oftentimes, the tension is assumed to be constant over the domain of the membrane, as would be the case with a drumhead [Rao 1990]. However, if the tension is known to vary proportionally in two different directions, then one can proceed with the derivation of the equation of motion while paying close attention to this variation. Furthermore, with respect to the initial tension, the out-of-plane displacements denoted $w(x,y,t)$ are assumed to be small enough that the tensions in each orthogonal direction in the membrane do not change as a function of time. From Chapter 2, the directional dependent tensions are formulated in Eq. (2.11). Numerical values are used for a numerical comparison in Chapter 4 but a more general solution will have to be derived first. Figure 3.4 shows such a membrane with arbitrary shape, bound by the curve S in the x-y plane. As shown at some location in the middle is a differential element of length dx and width dy. The forces $P_x dy$ and $P_y dx$ are the product of the tension (force per unit

length of membrane) and the differential dimension (units of length) perpendicular to the direction of load.

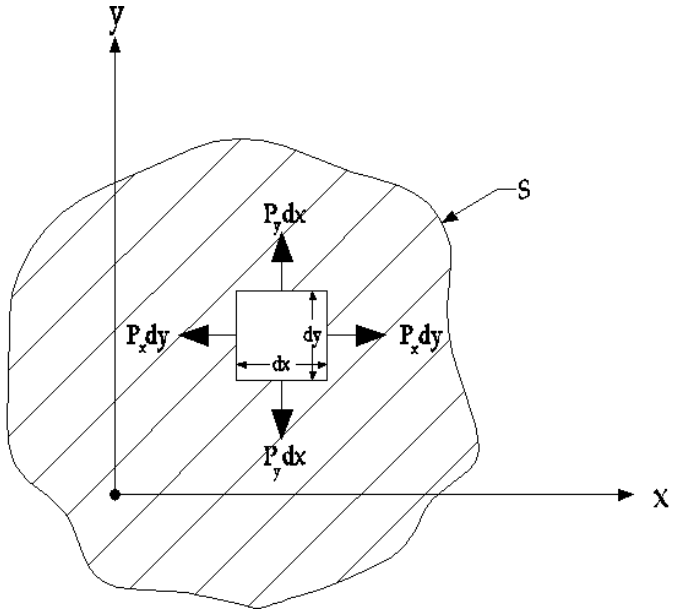

Figure 3.4: Membrane Bound by Plane Curve *S* in the *x*-*y* Plane

The physical conditions along the boundary *S* is discussed later, as they affect the spatial solution. However, they are not considered when a free body diagram of the displaced membrane is constructed.

3.3.1 Derivation of the Membrane Equation of Motion:

To derive the equation of motion, the membrane is assumed to be displaced some amount, *w*, in the out of plane direction *z*. The displaced membrane is then viewed in the *x*-*z* and *y*-*z* planes to determine the components of force in the *z* direction created by the forces shown in Figure 3.4. These components of force in the *z* direction are then added together and set equal to the inertial force as shown [Rao 1990]

$$\sum_i F_{zi} = \rho \frac{\partial^2 w}{\partial t^2} dx\, dy \tag{3.2}$$

Eq. (3.2) is clearly an application of Newton's Second Law; force equals mass times acceleration, with ρ representing the mass term, on a per-unit-area basis and the second derivative of w with respect to time representing the acceleration in the z direction. The $dxdy$ term represents the area of the differential element and accounts for the fact that the mass is given per unit area. The F_{zi} notation is simply a way of numbering the components of force in the z direction so that they may be added together after they all have been determined. Figure 3.5 shows the displaced membrane in the x-z plane.

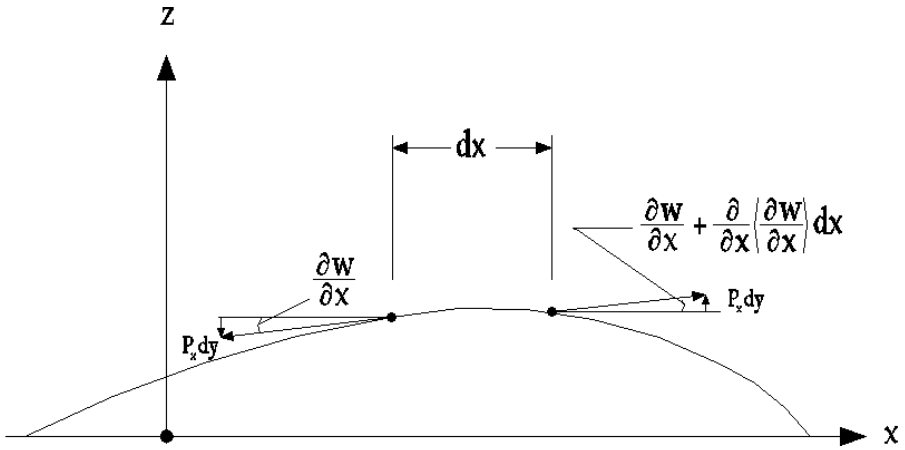

Figure 3.5: Displaced Membrane in the x-z Plane

As seen in Figure 3.5, both of the two forces due to tension in the membrane, $P_x\ dy$, have a component in the z direction. Using the simple "rise over run" approach, the slope of the force pointing in the negative x direction with respect to the x-axis is shown to be

$$-\frac{\partial w}{\partial x} \tag{3.3}$$

while the slope of the force in the positive x direction is shown to be

$$\frac{\partial w}{\partial x}+\frac{\partial}{\partial x}\left(\frac{\partial w}{\partial x}\right)dx \tag{3.4}$$

The force component of each tension in the z direction can be found by multiplying the force, $P_x\ dy$ by the slope it creates with the x-axis. With that, the first force in the z direction is found to be

$$F_{z1} = P_x \frac{\partial w}{\partial x} dy + P_x \frac{\partial}{\partial x}\left(\frac{\partial w}{\partial x}\right) dx dy \tag{3.5}$$

The other component of force in the z direction is found to be

$$F_{z2} = -P_x \frac{\partial w}{\partial x} dy \tag{3.6}$$

A similar procedure is followed to find the force components in the z direction by examining the displaced membrane in the y-z plane. Figure 3.6 shows this view of the membrane and the forces acting on the differential element.

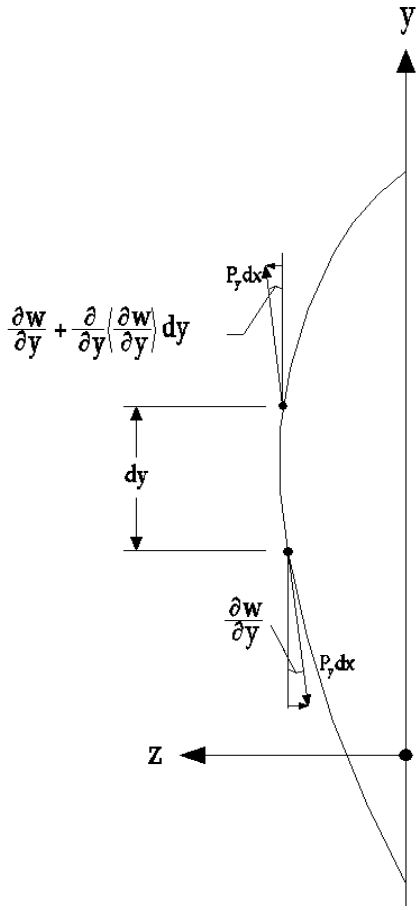

Figure 3.6: Displaced Membrane in the y-z Plane

The slope of the force pointing in the negative y direction with respect to the y-axis is shown to be

$$-\frac{\partial w}{\partial y} \tag{3.7}$$

and the slope of the force in the positive y direction is shown to be

$$\frac{\partial w}{\partial y}+\frac{\partial}{\partial y}\left(\frac{\partial w}{\partial y}\right)dy \tag{3.8}$$

Multiplying each of these slopes by their respective forces yields the following two force components in the z direction

$$F_{z3}=P_y\frac{\partial w}{\partial y}dx+P_y\frac{\partial}{\partial y}\left(\frac{\partial w}{\partial y}\right)dxdy \tag{3.9}$$

$$F_{z4}=-P_y\frac{\partial w}{\partial y}dx \tag{3.10}$$

At this point, there are four expressions for forces in the z direction, which can now be summed according to Eq. (3.2). Making the substitutions from Eq. (3.5), Eq. (3.6), Eq. (3.9) and Eq. (3.10) above gives the following balance of forces

$$\begin{aligned}&P_x\frac{\partial w}{\partial x}dy+P_x\frac{\partial}{\partial x}\left(\frac{\partial w}{\partial x}\right)dxdy-P_x\frac{\partial w}{\partial x}dy+\\&P_y\frac{\partial w}{\partial y}dx+P_y\frac{\partial}{\partial y}\left(\frac{\partial w}{\partial y}\right)dxdy-P_y\frac{\partial w}{\partial y}dx=\rho\frac{\partial^2 w}{\partial t^2}dx\,dy\end{aligned} \tag{3.11}$$

Eq. (3.11) contains some terms that sum to zero and can be simplified further by dividing through by the differential area $dxdy$ and using exponents to denote higher order partial derivatives. Thus, Eq. (3.11) reduces to

$$P_x\frac{\partial^2 w}{\partial x^2}+P_y\frac{\partial^2 w}{\partial y^2}=\rho\frac{\partial^2 w}{\partial t^2} \tag{3.12}$$

Eq. (3.12) is the equation of motion for free vibration for the membrane shown in Figure 3.4. Since it was derived on a differential element of an arbitrary membrane, Eq. (3.12) is valid for a flat membrane of any shape with tensions that are different in two different orthogonal directions such as x and y.

3.3.2 Spatial Solution to the Membrane Equation of Motion:

The first step in the vibration analysis of a mechanical system is to determine the natural frequencies and corresponding mode shapes. To obtain exact results, one must solve the equation of motion of an arbitrary membrane, Eq. (3.12) with

appropriate boundary conditions. With these properties of the system known, one can proceed to a more detailed time response of the system to various initial conditions and forcing functions by using the temporal solution that also can be found from Eq. (3.12). With that, this section focuses on solving Eq. (3.12) for the spatial solution, but the ability to predict a time response is kept intact throughout by including the temporal solution. The precise definition of *spatial solution* and *temporal solution* is given after a bit more analysis, as they are more clearly understood in the context of solving partial differential equations discussed later.

From the pressure vessel analysis in Chapter 2, it is known that a simple, proportional relationship exists between the tension in the x and y directions of the selected coupon. By using Eq. (2.12), the vibration analysis presented in this section is valid for any value of R on the torus. The expression for κ in Eq. (2.12) is for thin toroidal shells; however, any factor between tensions is acceptable for the subsequent analysis.

This relationship between the tension forces can be used to simplify the subsequent solution of the differential equation of motion, Eq. (3.12). With that, Eq. (2.12) is substituted into Eq. (3.12) and the x direction tension P_x is factored from the left-hand side yielding

$$P_x\left(\frac{\partial^2 w}{\partial x^2}+\kappa\frac{\partial^2 w}{\partial y^2}\right)=\rho\frac{\partial^2 w}{\partial t^2} \tag{3.13}$$

Dividing through both sides of the Eq. (3.13) by ρ allows another constant to be defined, namely c_1. Thus, Eq. (3.13) simplifies to

$$c_1^{\,2}\left(\frac{\partial^2 w}{\partial x^2}+\kappa\frac{\partial^2 w}{\partial y^2}\right)=\frac{\partial^2 w}{\partial t^2}$$
$$\text{where } c_1^{\,2}=\frac{P_x}{\rho} \qquad \text{Eq. (3.14)}$$

The task at hand is to solve the partial differential equation with constant coefficients given by Eq. (3.14). To solve this equation, it is assumed that the solution separates, and thus the separation of variables method from differential equations can be used. This method leads directly into modal analysis and the concepts of natural frequencies and associated mode shapes for distributed parameter systems [Inman 1996]. This assumption means, more precisely, that the out-of-plane displacement, w, is a function of the other three variables, x, y and t. Furthermore, the separation of variables implies that w is the product of three functions, each depending only on one variable. Quantitatively, separation of variables allows w to be written as

$$w(x,y,t) = X(x)Y(y)T(t) \tag{3.15}$$

The product $X(x)Y(y)$ gives out-of-plane displacements of points based on where they are located in space (on the membrane); thus, their solutions from Eq. (3.13) are referred to as the *spatial solution*. The function $T(t)$ is the variable that describes how the out-of-plane displacement changes in time and is thus referred to as the *temporal solution*. Now that a form of the solution for w has been assumed, the three second-order partial derivatives seen in Eq. (3.14) are found to be

$$\frac{\partial^2 w}{\partial x^2} = X''(x)Y(y)T(t) \tag{3.16}$$

$$\frac{\partial^2 w}{\partial y^2} = Y''(y)X(x)T(t) \tag{3.17}$$

$$\frac{\partial^2 w}{\partial t^2} = \ddot{T}(t)X(x)Y(y) \tag{3.18}$$

It should be noted that the double primes on the spatial functions, $X(x)$ and $Y(y)$ refer to total derivatives with respect to that variable, while the double over-dots on the time variable $T(t)$ refer to the total derivative with respect to time. These three derivatives can now be substituted into Eq. (3.14) yielding

$$c_1^2\left(X''(x)Y(y)T(t) + \kappa\, Y''(y)X(x)T(t)\right) = \ddot{T}(t)X(x)Y(y) \tag{3.19}$$

After dividing through by $X(x)Y(y)T(t)\ c_1^2$, this equation becomes

$$\frac{X''(x)}{X(x)} + \kappa \frac{Y''(y)}{Y(y)} = \frac{1}{c_1^{\,2}} \frac{\ddot{T}(t)}{T(t)} \tag{3.20}$$

In Eq. (3.20), one notes that since each term is a function of only one variable, the three terms must each be equal to three constants. To see this relationship, the total derivative of both sides of Eq. (3.20) is taken with respect to x. That is,

$$\frac{d}{dx}\left(\frac{X''(x)}{X(x)} + \kappa \frac{Y''(y)}{Y(y)} \right) = \frac{d}{dx}\left(\frac{1}{c_1^{\,2}} \frac{\ddot{T}(t)}{T(t)} \right) \tag{3.21}$$

Since the terms involving y and t are not functions of x, they are constant with respect to x, and thus become zero upon differentiation. Hence,

$$\frac{d}{dx} \frac{X''(x)}{X(x)} = 0 \tag{3.22}$$

Simply integrating both sides shows that the term involving x is simply equal to a constant of integration:

$$\frac{X''(x)}{X(x)} = -\alpha^2 \tag{3.23}$$

The minus sign assures that the right-hand side of Eq. (3.23) is always negative. A positive or zero value is mathematically possible but would yield physically impossible results [Inman 1996]. Based on the argument formed around Eq. (3.22) and Eq. (3.23), the other two terms from Eq. (3.20) can be assigned constant values

$$\kappa \frac{Y''(y)}{Y(y)} = -\beta^2 \tag{3.24}$$

$$\frac{1}{c_1^{\,2}} \frac{\ddot{T}(t)}{T(t)} = -\gamma^2 \tag{3.25}$$

From Eq. (3.20), the three arbitrarily assigned constants are related by

$$\alpha^2 + \beta^2 = \gamma^2 \tag{3.26}$$

Eq. (3.25), Eq. (3.26) and Eq. (3.27) are now algebraically manipulated to yield the more traditional form in terms of solving differential equations,

$$X''(x)+\alpha^2 X(x)=0 \qquad \text{Eq. (3.27)}$$

$$\kappa Y''(y)+\beta^2 Y(y)=0 \qquad \text{Eq. (3.28)}$$

$$\ddot{T}(t)+\gamma^2 {c_1}^2 T(t)=0 \qquad \text{Eq. (3.29)}$$

The general form of the solution to these second order, constant coefficient ordinary differential equations is given in many texts [Inman 1996 or Rao 1990]; however, the symbolic manipulation program *Mathematica* was used to determine independent solutions given the presence of the various constants arising from the physical properties and direction-dependent tension in the membrane. The *Mathematica* notebook used to solve Eq. (3.27) through Eq. (3.29) is supplied in Appendix 1. With that, the solutions are

$$X(x)=A_1\cos(\alpha x)+A_2\sin(\alpha x) \qquad (3.30)$$

$$Y(y)=A_3\cos\left(\frac{\beta y}{\sqrt{\kappa}}\right)+A_4\sin\left(\frac{\beta y}{\sqrt{\kappa}}\right) \qquad (3.31)$$

$$T(t)=A_5\cos(c_1\gamma t)+A_6\sin(c_1\gamma t) \qquad (3.32)$$

Since the initial concern with this membrane is natural frequencies and mode shapes, the primary concern is with the spatial solution. With Eq. (3.30) and Eq. (3.31), the form of the spatial solution of w is written directly as the product $X(x)Y(y)$:

$$w(x,y)=\left[A_1\cos(\alpha x)+A_2\sin(\alpha x)\right]\left[A_3\cos\left(\frac{\beta y}{\sqrt{\kappa}}\right)+A_4\sin\left(\frac{\beta y}{\sqrt{\kappa}}\right)\right] \qquad (3.33)$$

After expanding this expression and replacing products of various A_i terms with C_i, the spatial solution becomes

$$\begin{aligned} w(x,y)=C_1\cos(\alpha x)\cos\left(\frac{\beta y}{\sqrt{\kappa}}\right)+C_2\sin(\alpha x)\cos\left(\frac{\beta y}{\sqrt{\kappa}}\right)+ \\ C_3\sin(\alpha x)\cos\left(\frac{\beta y}{\sqrt{\kappa}}\right)+C_4\sin(\alpha x)\sin\left(\frac{\beta y}{\sqrt{\kappa}}\right) \end{aligned} \qquad (3.34)$$

The constants C_i will be found from the geometric boundary conditions, as discussed in the next section.

3.3.3 Application of Boundary Conditions to Spatial Solution:

At this time it is necessary to focus on a specific shape of membrane in order for the analysis to proceed. In Section 2.4, a flat, rectangular membrane element with finite area was considered to be tangent to a point on a thin toroidal shell. Furthermore, the state of stress in the rectangular membrane is presumed to be equivalent to the state of stress at the point of tangency as depicted in Figure 2.6. This rectangular coupon is presented again in three-dimensional Cartesian coordinates in Figure 3.7 with the dimensions *a* and *b* representing the width and length of the rectangle. Also, the equation for each edge is shown along with the direction of out-of-plane motion, *w*.

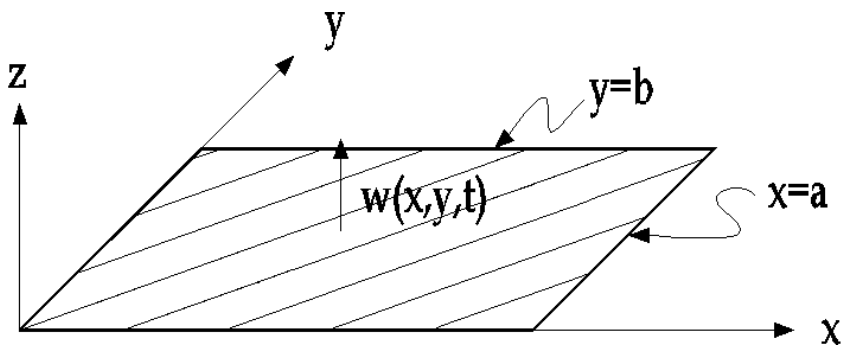

Figure 3.7: Rectangular Membrane in 3-D Cartesian Coordinates

For the purpose of this research, the boundaries of the membrane in Figure 3.7 are considered fixed. A fixed boundary condition is one in which no out-of-plane motion is allowed. Thus, *w(x, y, t)* is zero along each edge. The fixed boundary condition also constrains motion in the *x* and *y* directions, but this restriction is not mathematically relevant, as one of the presumptions of the preceding analysis was that only vibrations in the *z* direction were being considered. For the membrane under consideration, the fixed boundary condition on each edge can be expressed mathematically as

$$\begin{aligned} w(0,y)&=0 \quad (a) & \qquad w(x,0)&=0 \quad (c) \\ w(a,y)&=0 \quad (b) & \qquad w(x,b)&=0 \quad (d) \end{aligned} \tag{3.35}$$

Since these restrictions do not change with time, these four boundary conditions can now be applied to the spatial solution derived previously, Eq. (3.34). These boundary conditions along with the differential equation of motion, Eq. (3.14), define the eigenvalue problem [Meirovitch 1997]. Upon substitution of the relationship given in Eq. (3.35) (a), Eq. (3.34) simplifies to

$$w(0,y) = C_1 \cos\left(\frac{\beta y}{\sqrt{\kappa}}\right) + C_2 \sin\left(\frac{\beta y}{\sqrt{\kappa}}\right) = 0 \tag{3.36}$$

Since rigid body motion is not a physically acceptable phenomenon given the membrane in question, β must not equal zero [Inman 1996]. Therefore, in order for Eq. (3.36) to be valid for all values of y, C_1 and C_2 must equal zero. Thus, two terms from the spatial solution can be eliminated, reducing Eq. (3.34) to

$$w(x,y) = C_3 \sin(\alpha x)\cos\left(\frac{\beta y}{\sqrt{\kappa}}\right) + C_4 \sin(\alpha x)\sin\left(\frac{\beta y}{\sqrt{\kappa}}\right) \tag{3.37}$$

The boundary condition in Eq. (3.35) (b) is now applied to the spatial solution of Eq. (3.37) and the $\sin(\alpha a)$ term factored such that

$$w(a,y) = \sin(\alpha a)\left(C_3 \cos\left(\frac{\beta y}{\sqrt{\kappa}}\right) + C_4 \sin\left(\frac{\beta y}{\sqrt{\kappa}}\right)\right) = 0 \tag{3.38}$$

This expression is essentially the product of two terms, at least one of which must equal zero so that their products will equal zero. C_3 and C_4 could equal zero, but then the spatial solution would simply become zero, the trivial solution in which no motion occurs. Thus, it is concluded that

$$\sin(\alpha a) = 0 \tag{3.39}$$

This is true when the argument of the sine function equals zero and multiples of π. The zero value is discarded because it does not offer any new information about α and would allow rigid body motion. Therefore,

$$\alpha_m a = m\pi \quad or \quad \alpha_m = \frac{m\pi}{a} \quad (m = 1,2,3,\ldots\infty) \tag{3.40}$$

where m is an integer and α has been assigned the m subscript to denote an infinite number of values corresponding to integer multiples of π. When the

boundary condition in Eq. (3.35) (c) is applied to the spatial solution of Eq. (3.37), it is clear that

$$w(x,0) = C_3 \sin(\alpha x) = 0 \tag{3.41}$$

Again, if Eq. (3.41) is to be valid for all values of x and α is nonzero as specified in Eq. (3.40), one must conclude that C_3 equals zero. With that, the spatial solution of Eq. (3.37) simplifies further to

$$w(x,y) = C_4 \sin(\alpha x)\sin\left(\frac{\beta y}{\sqrt{\kappa}}\right) \tag{3.42}$$

The fourth boundary condition, Eq. (3.35) (d) is now applied to the most recent spatial solution, which becomes

$$w(x,b) = C_4 \sin(\alpha x)\sin\left(\frac{\beta b}{\sqrt{\kappa}}\right) = 0 \tag{3.43}$$

Clearly, with C_1, C_2 and C_3 already shown to be zero, C_4 cannot be zero if the trivial solution is to be avoided. The $\sin(\alpha x)$ term cannot be zero, as the equation must hold for all values of x, which is not possible because α is an integer multiple of π. Thus, the remaining sine term must equal zero:

$$\sin\left(\frac{\beta b}{\sqrt{\kappa}}\right) = 0 \tag{3.44}$$

Again, this expression is a characteristic equation that is true when the argument of the sine function equals zero and multiples of π. As was the case earlier, the zero value is discarded, because it offers no new information about β, which was presumed nonzero to determine C_1 and C_2. Therefore,

$$\frac{\beta_n b}{\sqrt{\kappa}} = n\pi \quad or \quad \beta_n = \frac{n\pi\sqrt{\kappa}}{b} \quad (n = 1,2,3,\ldots\infty) \tag{3.45}$$

3.3.4 Natural Frequencies and Mode Shapes:

The two characteristic equations, Eq. (3.40) and Eq. (3.45), are added in accordance to Eq. (3.26) to define the eigenvalues of the rectangular membrane shown in Figure 3.7. These eigenvalues are expressed in Eq. (3.46), where the

subscripts have been added to γ to denote multiple values dependent on integer values of m and n such that

$$\left(\frac{m\pi}{a}\right)^2+\left(\frac{n\pi\sqrt{\kappa}}{b}\right)^2=\gamma_{mn}{}^2 \tag{3.46}$$

After simplification, the eigenvalues can be written as

$$\gamma_{mn}=\pi\sqrt{\left(\frac{m}{a}\right)^2+\kappa\left(\frac{n}{b}\right)^2} \tag{3.47}$$

This expression for eigenvalues can now be used to calculate the natural frequencies of the rectangular membrane depicted in Figure 3.7. This is done by converting the eigenvalues from eigenspace to physical coordinates, as seen in the period of oscillation (natural frequency) of the time solution in Eq. (3.32). With that,

$$\omega_{mn}=c_1\gamma_{mn} \tag{3.48}$$

Following this equation along with the definition of c_1 in Eq. (3.14) and γ_{mn} in Eq. (3.47), the natural frequencies become

$$\omega_{mn}=\pi\sqrt{\frac{P_x}{\rho}\left(\left(\frac{m}{a}\right)^2+\kappa\left(\frac{n}{b}\right)^2\right)} \tag{3.49}$$

Next, with the constants α and β now known, the eigenfunctions w_{mn} are written from the most recent spatial solution as

$$w_{mn}=C_{mn}\sin\left(\frac{m\pi}{a}x\right)\sin\left(\frac{n\pi}{b}y\right) \tag{3.50}$$

Plots of the first four mode shapes are shown in Chapter 7. Mode shapes and eigenfunctions differ only by a constant, thus the constant C_{mn} is a scaling factor for the eigenfunction and is arbitrarily chosen to be unity. Since the membrane equation of motion is linear, any linear combination of solutions is a solution [Inman 1996]. Thus, the general form of the spatial solution is

$$w(x,y)=\sum_{m=1}^{\infty}\sum_{n=1}^{\infty}\sin\left(\frac{m\pi}{a}x\right)\sin\left(\frac{n\pi}{b}y\right) \tag{3.51}$$

3.3.5 Total Solution to the Membrane Equation of Motion:

Now that the general form of the spatial solution has been found, it can be multiplied by *T(t)* to find the total solution. From Eq. (3.32) and Eq. (3.51), the total solution is

$$w(x,y,t)=\sum_{m=1}^{\infty}\sum_{n=1}^{\infty}\sin\left(\frac{m\pi}{a}x\right)\sin\left(\frac{n\pi}{b}y\right)\left(A_5\cos(\omega_{mn}t)+A_6\sin(\omega_{mn}t)\right) \qquad (3.52)$$

where ω_{mn} is given in Eq. (3.49). The constants A_5 and A_6 can be found by application of initial conditions and utilizing the orthogonal nature of the eigenfunctions. However, the time response is not of interest to this preliminary vibration analysis but will be useful in future studies.

3.4 Summary:

Chapter 3 presents the derivation of a closed-form solution to the equation of motion for a bare rectangular membrane with fixed edges and tensions that differ by a constant factor in two orthogonal directions. Exact equations are found for the natural frequencies and mode shapes of this continuous system. The next step is to analyze a similar membrane with a rectangular PVDF patch attached to the membrane's center. However, energy methods will be used to derive the equation of motion and approximate natural frequencies and mode shapes will be generated using the Rayleigh-Ritz method, as a closed-form solution is not readily available. Also, the finite element method can be used to model such a membrane with an attachment. Since both these methods are advanced mathematical approximation techniques, they are first used in Chapter 4 to analyze the same bare membrane from Figure 3.7 and are compared to the closed-form solution for natural frequencies and mode shapes from Chapter 3 to establish their accuracy and proper implementation. Once these two approximation methods have been verified on a system with a readily available closed-form solution, they can subsequently be applied to a system without a known closed-form solution, namely, a membrane with a PVDF attachment.

Chapter 4

Approximation Methods for Bare Membrane Vibrations

4.1 Introduction:

Chapter 3 discusses the derivation of the partial differential equation of motion for a flat membrane subjected to different tensions in the x and y directions using Newton's Method. The total solution was found from the equation of motion using the separation of variables approach. Boundary conditions were applied to the spatial solution to find expressions for the natural frequencies and mode shapes. However, this method of analyzing the vibrations of continuous systems is limited because only basic systems with fairly simple boundary conditions will yield a closed-form solution. More complex mechanical systems can have differential equations of motion whose solutions are either extremely difficult or impossible to find directly. Therefore, mathematical techniques have been developed to approximate the natural frequencies and mode shapes of such complicated problems without solving the eigenvalue problem of the exact equation of motion.

The Rayleigh-Ritz method is a widely used technique for approximating the solution to the eigenvalue problem for self-adjoint, distributed-parameter systems. Employing this approach, one replaces the original eigenvalue problem with a sequence of algebraic eigenvalue problems by approximating the out-of-plane displacements by a series of linearly independent functions of the spatial variables [Meirovitch 1997]. With the form of the deflection "known," one can proceed to approximate the natural frequencies and mode shapes of the system.

Another popular way to approximate the natural frequencies and mode shapes of a mechanical system is by using finite elements. The finite element method is a powerful numerical procedure used to solve many types of engineering problems beyond the scope of simplified analytical models. This method divides the member of interest into small elements of finite size and determines the response of each element, taking into account the reactions of the other elements. Mathematically, this task is accomplished by solving a set of coupled algebraic equations. Matrix notation is typically employed when the number of elements becomes large, and computers are often used to solve such unwieldy equations in a timely manner. To that end, there are many commercially available finite element packages that allow the user to draw in a desired geometry through a CAD front-end and then define the size, shape and type of elements to be used. The software then builds global mass and global stiffness matrices and solves for the natural frequencies and mode shapes. The software package ANSYS was used for the current research effort.

Both the Rayleigh-Ritz and finite element methods are used in this chapter to approximate the solution to the bare membrane analyzed in closed form in Chapter 3. By performing such approximations on a system with a known exact solution, one can verify their proper use and accuracy. After these approximation methods are seen to accurately predict the results from the exact

solution, they can be used with confidence to analyze more complicated systems for which no exact solutions are readily available. In particular, Chapter 5 focuses on using these approximation techniques to analyze a membrane with a PVDF attachment.

4.2 Energy and Rayleigh-Ritz Methods for Bare Membrane:

Oftentimes it is easier to derive equations of motion for mechanical systems using Newton's Methods as discussed in Chapter 3. However, this procedure only works for a few simple systems and offers the ability to handle only simple boundary conditions. By using energy methods, one can handle systems of much higher complexity and more complicated boundary conditions. To use energy methods, one must formulate the kinetic and potential energies as well as the work done by external forces, the latter for forced vibrations only. These quantities are then combined using Hamilton's Principle as discussed in Section 4.2.3. One then takes the variation of the expression formed using Hamilton's Principle and sets it equal to zero. From this, the equation of motion and boundary conditions can be extracted. While the use of energy methods for membrane vibrations is presented in many vibration texts, most consider only the simplified case of constant tension in all directions. In contrast, the procedure outlined below is more general in that it accounts for tensions that vary by a constant factor in two orthogonal directions.

4.2.1 Kinetic Energy:

Derivation of the expression for kinetic energy is fairly simple if approached from the point of view of elementary mechanics. For an object with mass m traveling at a velocity $\dot{x}$, such as the one degree-of-freedom system shown in Figure 3.1, the kinetic energy K is given as

$$K = \frac{1}{2} m \dot{x}^2 \tag{4.1}$$

where $\dot{x} = dx/dt$. For membranes, the velocity is expressed as the partial derivative of the out-of-plane displacement w with respect to time. Furthermore, the mass is specified on a per-unit-area basis, and must be integrated (summed) over the area of the membrane. Thus, for a membrane in Cartesian coordinates with constant mass per unit area ρ, the kinetic energy is given by

$$K = \frac{1}{2}\iint \rho\left(\frac{\partial w}{\partial t}\right)^2 dxdy \tag{4.2}$$

4.2.2 Potential Energy:

When a membrane is displaced from its flat, equilibrium position, a slight stretching occurs. This stretching results in potential energy, also known as strain energy, being stored within the membrane material. To derive an expression for the potential energy, one must consider the displaced membrane from a work-energy standpoint. That is, since energy is defined as the ability to do work, the potential energy of the system is equal to the work done by the tension to return the membrane to its equilibrium position. With work defined as a force applied over a distance, consider a differential element of an arbitrary membrane with unequal tensions as shown in Figure 4.1.

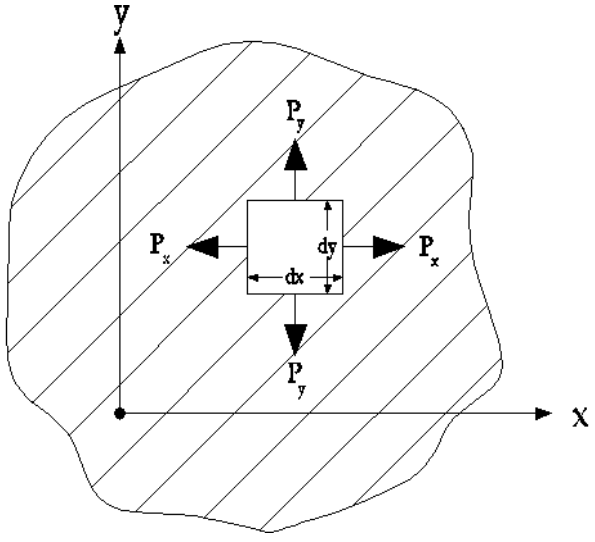

Figure 4.1: Differential Element with Unequal Tensions P_x and P_y

For the simplified case of constant tension in all directions, as addressed in most vibration texts, one can formulate the potential energy by integrating the product of the tension and the change in area of the differential element shown mathematically as

$$\begin{aligned} U &= \iint T(dA' - dA) \\ where\ \ T &= uniform\ tension \\ dA' &= stretched\ area \\ dA &= unstretched\ area \end{aligned} \tag{4.3}$$

However, for tensions that vary by direction, the stretching must be considered in the x and y directions independently. Thus, consider the differential element in Figure 4.1 to be displaced by a small amount, viewed first in the x-z plane as shown in Figure 4.2.

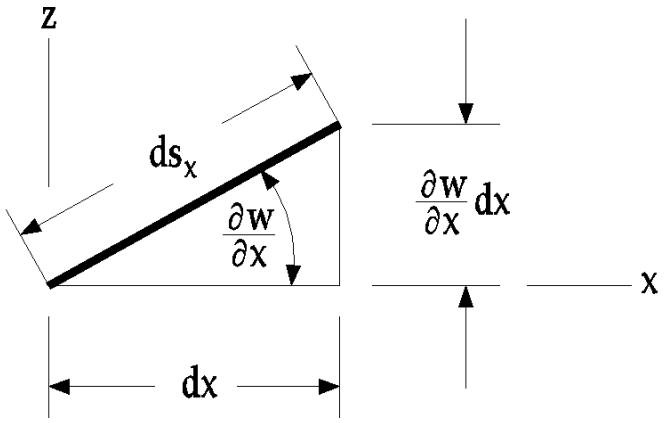

Figure 4.2: Displaced Element in the x-z Plane

When in this displaced position, the initial dimension of the element, dx, is stretched to the size ds_x. Using the Pythagorean relationship for sides of right triangles, ds_x is expressed as

$$ds_x = dx\sqrt{1 + \left(\frac{\partial w}{\partial x}\right)^2} \tag{4.4}$$

If the same displaced element is viewed in the y-z plane, as in Figure 4.3, the stretched length ds_y is found to be

$$ds_y = dy\sqrt{1+\left(\frac{\partial w}{\partial y}\right)^2} \tag{4.5}$$

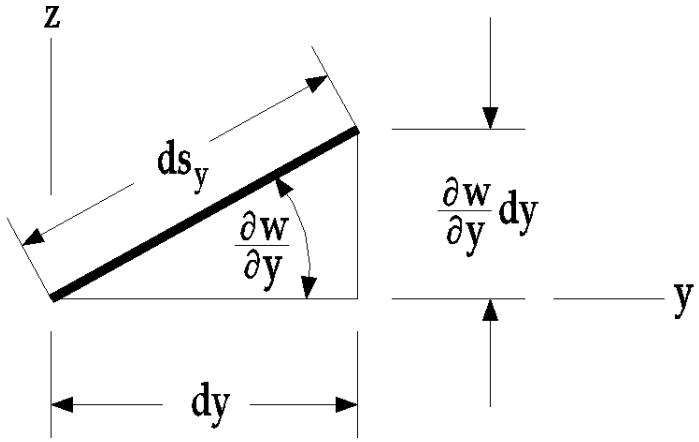

Figure 4.3: Displaced Element in the *y*-*z* Plane

Since the present study is concerned only with small amplitude vibrations, the slopes $\frac{\partial w}{\partial x}$ and $\frac{\partial w}{\partial y}$ are assumed to remain much smaller than one. Thus, Eq. (4.4) and Eq. (4.5) can be approximated using a binomial expansion where only the first two terms in the series are retained giving

$$ds_x \approx dx\left[1+\frac{1}{2}\left(\frac{\partial w}{\partial x}\right)^2\right] \tag{4.6}$$

$$ds_y \approx dy\left[1+\frac{1}{2}\left(\frac{\partial w}{\partial y}\right)^2\right] \tag{4.7}$$

From before, the strain energy density in the differential element is known to be the tension multiplied by the amount of stretch. Integrating over the entire area of the membrane sums the contribution of each differential element. With that, the potential energies due to stretching in the *x* and *y* directions on a rectangular membrane are

$$U_x = \iint P_x\left(ds_x - dx\right)dy \tag{4.8}$$

$$U_y = \iint P_y\left(ds_y - dy\right)dx \tag{4.9}$$

The total potential energy of the membrane is simply the sum of energy created by stretching in the *x* and *y* directions. Thus,

$$U = \iint P_x \left(ds_x - dx\right)dy + P_y \left(ds_y - dy\right)dx \tag{4.10}$$

Upon substitution of the approximations from Eq. (4.6) and Eq. (4.7) and algebraic simplification, the expression for total potential energy becomes

$$U = \frac{1}{2}\iint \left[P_x \left(\frac{\partial w}{\partial x}\right)^2 + P_y \left(\frac{\partial w}{\partial y}\right)^2 \right] dxdy \tag{4.11}$$

A more useful version of Eq. (4.11) is found by employing the proportional relationship between the tensions in the *x* and *y* directions as shown in Eq. (2.12). With that, Eq. (4.11) becomes

$$U = \frac{1}{2}\iint P_x \left[\left(\frac{\partial w}{\partial x}\right)^2 + \kappa \left(\frac{\partial w}{\partial y}\right)^2 \right] dxdy \tag{4.12}$$

4.2.3 Hamilton's Principle:

With expressions for the total kinetic and potential energies given by Eq. (4.2) and Eq. (4.12), respectively, one can employ Hamilton's Principle, which states, in the absence of externally applied forces,

> *Of all possible paths of motion to be taken between two instants of time t_1 and t_2, the actual path taken by the system gives a stationary (extremum) value to the integral*
>
> $$I = \int_{t_1}^{t_2} (K - U)\, dt \tag{4.13}$$
>
> *where K-U is considered conservative, that is, one in which [energy dissipation] is neglected* [Magrab 1979].

The integrand of Eq. (4.13), *K-U*, is commonly referred to as the Lagrangian of the system. With the energy expressions from Eq. (4.2) and Eq. (4.12), Hamilton's Principle yields the functional

$$I = \int_{t_1}^{t_2} \iint \frac{\rho}{2}\left(\frac{\partial w}{\partial t}\right)^2 - \frac{P_x}{2}\left[\left(\frac{\partial w}{\partial x}\right)^2 + \kappa\left(\frac{\partial w}{\partial y}\right)^2\right] dxdydt \tag{4.14}$$

4.2.4 Variational Methods to Determine Equation of Motion:

According to Hamilton's Principle, the equation of motion and boundary conditions for the rectangular membrane of interest in this chapter corresponds to an extremum value of Eq. (4.14). If *I* were a function of only a single variable, critical points would be found by using the calculus of one variable to find locations at which the first derivative of *I* is equal to zero. However, *I* is a function of other functions and is referred to as a functional. Thus, the calculus of variations must be used to determine stationary points of Eq. (4.14). Instead of locations where the first derivative equals zero, as for single variable calculus, variational methods require locations where the first variation is zero. Under standard notation of variational calculus, the first variation of a functional is denoted $\delta^{(1)}$ hence, Hamilton's Principle requires that

$$\begin{gathered} \delta^{(1)}[I] = 0 \\ or \\ \delta^{(1)}\left[\int_{t_1}^{t_2} \iint \frac{\rho}{2}\left(\frac{\partial w}{\partial t}\right)^2 - \frac{P_x}{2}\left[\left(\frac{\partial w}{\partial x}\right)^2 + \kappa\left(\frac{\partial w}{\partial y}\right)^2\right] dxdydt\right] = 0 \end{gathered} \tag{4.15}$$

The functional *I* is a function of one dependent variable, *w*, functions of *w* and three independent variables, *x, y* and *t* and can be expressed generally as

$$\begin{gathered} I(w) = \int_{t_1}^{t_2} \iint F\left(x, y, t, w, \dot{w}, w_x, w_y\right) dxdydt \\ where \quad \dot{w} = \frac{\partial w}{\partial t}, \quad w_x = \frac{\partial w}{\partial x}, \quad w_y = \frac{\partial w}{\partial y} \end{gathered} \tag{4.16}$$

The variational calculus for a functional of this form, while difficult, is fairly well illustrated in many texts. Thus, the details of taking the first variation of Eq. (4.14) are omitted. Instead, the findings of Magrab [1979] are employed in the following fashion. For a rectangular membrane aligned with a Cartesian

coordinate system, as seen in Figure 3.7, the first variation of Eq. (4.16) set equal to zero is

$$\delta^{(1)}[I(w)] = \int_{t_1}^{t_2} \left[\iint_D \eta(\Im_1(w) - \Im_2(\dot{w}))dD + \int_S \eta B_1(w) ds \right] dt = 0 \tag{4.17}$$

where

$$\Im_1(w) = F_w - \frac{\partial F_{w_x}}{\partial x} - \frac{\partial F_{w_y}}{\partial y}, \quad \Im_2(\dot{w}) = \frac{\partial F_{\dot{w}}}{\partial t},$$

$$B_1(w) = F_{w_n}, \quad D = Surface, \quad S = boundaries$$

At this point, it is necessary to explain the notation employed in Eq. (4.17). A subscript on either *F* or *w* denotes a partial derivative of *F* or *w* with respect to the subscripted variable. This also applies to subscripts on subscripts. Figure 4.4 explains this notation in mathematical form.

$$F_w = \frac{\partial F}{\partial w}, \quad F_{w_x} = \frac{\partial F}{\partial\left(\frac{\partial w}{\partial x}\right)}, \quad \frac{\partial F_{w_x}}{\partial x} = \frac{\partial \frac{\partial F}{\partial w_x}}{\partial x} = \frac{\partial\left(\frac{\partial F}{\partial\left(\frac{\partial w}{\partial x}\right)}\right)}{\partial x}$$

Figure 4.4: Explanation of Subscript Notation

When the first variation shown in Eq. (4.17) is set equal to zero as in Eq. (4.15), an extremum point can be found. The function η is arbitrary, but must be continuous, twice differentiable and equal to zero for all *x* and *y* at t_1 and t_2. In addition, η is subject to physical boundary conditions such as free or fixed as discussed shortly. With that, Eq. (4.17) can be satisfied only if the following conditions are met:

$$\begin{aligned} &(a)\ \Im_1(w) - \Im_2(\dot{w}) = 0 \quad \textit{membrane interior} \\ &(b)\ \oint_S \eta\, B_1(w) ds = 0 \quad \textit{membrane boundary} \end{aligned} \tag{4.18}$$

With F defined in the integrand of Eq. (4.14), one can take the necessary partial derivatives to form

$$\begin{aligned} \Im_1(w) &= P_x\left(\frac{\partial^2 w}{\partial x^2}\right) + P_x\kappa\left(\frac{\partial^2 w}{\partial y^2}\right) \\ \Im_2(\dot{w}) &= \rho\left(\frac{\partial^2 w}{\partial t^2}\right) \end{aligned} \tag{4.19}$$

These two expressions can then be substituted into Eq. (4.18) (a) and simplified to

$$P_x\left[\left(\frac{\partial^2 w}{\partial x^2}\right) + \kappa\left(\frac{\partial^2 w}{\partial y^2}\right)\right] = \rho\left(\frac{\partial^2 w}{\partial t^2}\right) \tag{4.20}$$

If the constant c_1 from Eq. (3.14) is employed, Eq. (4.20) becomes

$$\begin{aligned} c_1{}^2\left(\frac{\partial^2 w}{\partial x^2} + \kappa\frac{\partial^2 w}{\partial y^2}\right) &= \frac{\partial^2 w}{\partial t^2} \\ \textit{where } c_1{}^2 &= \frac{P_x}{\rho} \end{aligned} \tag{4.21}$$

One clearly recognizes Eq. (4.21) to be identical to Eq. (3.14), the equation of motion for the bare membrane of interest in this chapter. As expected, derivation of the equation of motion using energy methods produced the same result as derivation by Newton's Method as detailed in Chapter 3.

Eq. (4.18) (b) is used to specify the boundary conditions. With the definition of $B_1(w)$ from Eq. (4.17), the boundary condition in Eq. (4.18) (b) can be rewritten as

$$\oint_S \eta\, F_{w_n}\, ds = 0 \tag{4.22}$$

In order for Eq. (4.22) to be satisfied, at least one of the terms in the integrand must be zero. If the first term, η, which is simply the variation of w, is zero, then w must be a known value. Therefore, one writes for the membrane boundary S,

$$\eta = 0, \ \textit{thus } w = \textit{presribed value} \tag{4.23}$$

This type of boundary condition is referred to as *essential* [Reddy 1984] or *kinematic* [Shames 1985]. Most often, boundaries are said to be *fixed*, in which case the displacement w is prescribed to be zero as well. The second term of the

integrand in Eq. (4.22), written in expanded form in Eq. (4.24), could also equal zero:

$$\frac{\partial F}{\partial\left(\frac{\partial w}{\partial \mathbf{n}}\right)} = 0 \tag{4.24}$$

In Eq. (4.24), **n** refers to the normal direction along the membrane boundary S. For a rectangular membrane aligned with a Cartesian coordinate system, **n** and the tangent direction s combine to form four pairs of boundary conditions. For the edges parallel to the y-axis at x_1 and x_2, **n** becomes x while s becomes y. For the other two edges, which are parallel to the x-axis at y_1 and y_2, **n** becomes y while s becomes x. For the rectangular element shown in Figure 3.7 with one corner at the origin, x dimension of a and y dimension of b, one can take the two partial derivatives indicated Eq. (4.24) (for **n** equal to x and then y) and show that the *natural* [Reddy 1984] boundary conditions become

$$\begin{aligned} &P_x\left(\frac{\partial w}{\partial x}\right) = 0 \; along \; x = 0 \; and \; x = a \\ &and \; P_x \kappa\left(\frac{\partial w}{\partial y}\right) = 0 \; along \; y = 0 \; and \; y = b \end{aligned} \tag{4.25}$$

Eq. (4.25), also referred to as a *free* boundary condition, requires that there be no component of the direction-dependent tension in the transverse direction along the membrane edges [Shames 1985].

Along each boundary of the membrane, one of these boundary conditions, Eq. (4.23) or Eq. (4.25), must be met. Furthermore, it is noted that these *fixed* and *free* boundary conditions, which arose from using Hamilton's Principle, make sense physically, since a fixed edge will have zero out-of-plane displacement, and a free edge will not support any force transverse to the plane of the membrane.

4.2.5 Rayleigh-Ritz Method:

Now that a differential equation of motion has been found, Eq. (4.20), one could attempt to solve for an expression that relates the out-of-plane displacement to the spatial variables x and y as well as time, namely, $w(x,y,t)$. In Chapter 3, a closed-form solution was found to Eq. (4.21); however, not all physical configurations have such precise solutions. The Rayleigh-Ritz method is a way to approximate the natural frequencies and mode shapes without solving the differential equation of motion [Meirovitch 1967]. This method is first described in general and then applied to the bare membrane with different tensions in the x and y directions.

4.2.5.1 Rayleigh-Ritz for a General System:

As mentioned previously, the Rayleigh-Ritz method requires one to select comparison functions u_i that satisfy the boundary conditions of the problem. One can then approximate the eigenfunctions w_n as a linear combination of these comparison functions such that

$$w_n = \sum_{i=1}^{n} a_i u_i \tag{4.26}$$

The constants a_i in Eq. (4.26) are unknown at this point, but can be found later as part of the solution to a finite dimensional eigenvalue problem. When the eigenfunctions are approximated as in Eq. (4.26), the general form of Rayleigh's Quotient can be written in terms of L and M as

$$R(w_n) = \frac{\int_D w_n L[w_n]\, dD}{\int_D w_n M[w_n]\, dD} = \frac{Num(w_n)}{Den(w_n)} \tag{4.27}$$

In Eq. (4.27), L and M are differential operators that are discussed in more detail later for the specific membrane of interest and D is the surface area of the membrane. The numerator and denominator of Eq. (4.27), $Num(w_n)$ and $Den(w_n)$, respectively, are both positive for a positive definite system [Meirovitch 1967].

Furthermore, in this form the Rayleigh Quotient will give an upper bound on the eigenvalue, thus

$$R(w_n) \geq \lambda_n \tag{4.28}$$

The equality portion of Eq. (4.28) is true only if the selected comparison functions are the true eigenfunctions of the system. Thus, for approximate eigenfunctions, the predicted eigenvalue is always higher than the actual value. As a result, minimizing the Rayleigh Quotient will tend to converge to the true eigenvalue from above. This is done by first substituting Eq. (4.26) into Eq. (4.27), and then minimizing Eq. (4.27) through variational methods, which require that

$$\frac{\partial R(w_n)}{\partial a_r} = 0 \quad r = 1, 2, \ldots n \tag{4.29}$$

Using the quotient rule for derivatives, this partial derivative of the Rayleigh Quotient becomes

$$\frac{\partial R(w_n)}{\partial a_r} = \frac{Den(w_n)\left(\frac{\partial Num(w_n)}{\partial a_r}\right) - Num(w_n)\left(\frac{\partial Den(w_n)}{\partial a_r}\right)}{Den^2(w_n)} = 0 \quad r = 1, 2, \ldots n \tag{4.30}$$

If the minimum estimated value of $R(w_n)$ is denoted ${}^n\Lambda$, Eq. (4.30) reduces to

$$\left(\frac{\partial Num(w_n)}{\partial a_r}\right) - {}^n\Lambda\left(\frac{\partial Den(w_n)}{\partial a_r}\right) = 0 \quad r = 1, 2, \ldots n \tag{4.31}$$

The approximate eigenfunctions of Eq. (4.26) are now substituted into the definitions of $Num(w_n)$ and $Den(w_n)$ and simplified to

$$\begin{aligned} Num &= \int_D \sum_{i=1}^{n} a_i u_i L\left[\sum_{j=1}^{n} a_j u_j\right] dD = \sum_{i=1}^{n}\sum_{j=1}^{n} a_i a_j \int_D u_i L[u_j]\, dD \\ Den &= \int_D \sum_{i=1}^{n} a_i u_i M\left[\sum_{j=1}^{n} a_j u_j\right] dD = \sum_{i=1}^{n}\sum_{j=1}^{n} a_i a_j \int_D u_i M[u_j]\, dD \end{aligned} \tag{4.32}$$

At this point, one can define the stiffness and mass matrix entries, respectively as

$$\begin{aligned} k_{ij} &= \int_D u_i L[u_j]\, dD \\ m_{ij} &= \int_D u_i M[u_j]\, dD \end{aligned} \tag{4.33}$$

For self-adjoint systems, these matrices are symmetric, thus k_{ij} equals k_{ji} and m_{ij} equals m_{ji} [Meirovitch 1967]. With these new but familiar terms, *Num* and *Den* simplify considerably to

$$\begin{aligned} Num &= \sum_{i=1}^{n}\sum_{j=1}^{n} k_{ij} a_i a_j \\ Den &= \sum_{i=1}^{n}\sum_{j=1}^{n} m_{ij} a_i a_j \end{aligned} \tag{4.34}$$

Taking the necessary derivatives of *Num* and *Den* as required by Eq. (4.31) produces

$$\sum_{j=1}^{n} \left(k_{rj} - {}^{n}\Lambda m_{rj}\right) a_j = 0 \quad r = 1, 2, \ldots n \tag{4.35}$$

Eq. (4.35) represents a system of n equations with n unknowns, namely a_j. Changing to matrix notation, Eq. (4.35) becomes the traditional matrix eigenvalue problem of the form

$$\left([k] - {}^{n}\Lambda[m]\right)\{a\} = 0 \tag{4.36}$$

Here, the prefix superscript n on Λ represents the number of terms used to approximate the eigenfunction. This equation is solved for the nontrivial case when the determinate of the term in parentheses equals zero. By setting this determinate equal to zero, one can solve for the eigenvalues, which are the square of the natural frequencies. This equation will be revisited in the next section for a system consisting of a rectangular membrane with different x and y tensions.

4.2.5.2 Rayleigh-Ritz for Rectangular Membrane:

Despite the fact that a closed-form solution exists for Eq. (4.20), the Rayleigh-Ritz method will be employed here to establish its validity and proper implementation as this system has a known solution. In the previous section, the Rayleigh Quotient for a general system was given from Meirovitch [1967]. However, it is in the interest of completeness to understand where this

expression comes from for the system of interest in this section. First, the conservation of energy principle is invoked requiring that the sum of kinetic and potential energies for free vibration of a system (e.g. total energy) remain constant. From this, it can be shown that

$$U_{\max} = K_{\max} \tag{4.37}$$

For a system undergoing harmonic motion in a natural mode W_n with a natural frequency ω_n, the out of plane displacement, w, can be written as

$$w(x,y,t) = W_n(x,y)\cos(\omega_n t) \tag{4.38}$$

Here, W_n represents the maximum displacement at a point (x,y) and the cosine function depicts the harmonic time-dependent motion. With the expression for kinetic energy from Eq. (4.2), one can differentiate Eq. (4.38) as required to show that

$$K = \frac{\omega_n{}^2 \sin^2 \omega_n t}{2} \iint \rho\, W_n{}^2 dxdy \tag{4.39}$$

Eq. (4.39) attains a maximum value when the trigonometric function equals one. Thus,

$$K_{\max} = \frac{\omega_n{}^2}{2} \iint \rho\, W_n{}^2 dxdy \tag{4.40}$$

By the same argument, one can use the expression for potential energy, Eq. (4.12), with the displacement from Eq. (4.38) to show that the potential energy has a maximum given by

$$U_{\max} = \frac{1}{2} \iint P_x \left[\left(\frac{\partial W_n}{\partial x} \right)^2 + \kappa \left(\frac{\partial W_n}{\partial y} \right)^2 \right] dxdy \tag{4.41}$$

Using these expressions for maximum potential and kinetic energies, ω_n is found to be

$$\omega_n{}^2 = \frac{\iint P_x \left[\left(\frac{\partial W_n}{\partial x} \right)^2 + \kappa \left(\frac{\partial W_n}{\partial y} \right)^2 \right] dxdy}{\iint \rho\, W_n{}^2 dxdy} = R(W_n) \tag{4.42}$$

As before, the eigenfunctions are approximated in the form of Eq. (4.26). However, for the two-dimensional case of a rectangular membrane, a dual summation is required. For a rectangular membrane in a Cartesian coordinate system with one corner at the origin and the other at (*a*,*b*), the approximated eigenfunctions w_i are

$$w_i = \sum_{i=1}^{M*N} a_i u_i = \sum_{m=1}^{M}\sum_{n=1}^{N} a_{mn} \sin\left(\frac{m\pi x}{a}\right)\sin\left(\frac{n\pi y}{b}\right) \tag{4.43}$$

Since the selected approximate eigenfunctions are identical to the exact eigenfunctions from the closed form solution, Eq. (3.52), one expects the Rayleigh Quotient to produce exact values for the natural frequencies and mode shapes. Next, Eq. (4.42) can be rewritten in the form of Eq. (4.27):

$$\omega_{ij}^{\ 2} = \Lambda_{ij} = \frac{\int_0^b \int_0^a w_i L[w_j]\, dxdy}{\int_0^b \int_0^a w_i M[w_j]\, dxdy}$$

$$where \quad L = -P_x\left[\left(\frac{\partial^2}{\partial x^2}\right) + \kappa\left(\frac{\partial^2}{\partial y^2}\right)\right] \tag{4.44}$$

$$and \quad M = \rho$$

Here, *L* is a second order linear differential operator while *M* is a zero order linear differential operator. Each is obtained most directly from the equation of motion, Eq. (4.20). With *L* and *M* defined for the system under consideration, Eq. (4.33) can be applied to construct stiffness and mass matrices, from which one can formulate and solve the traditional eigenvalue problem shown in Eq. (4.36). To demonstrate the accuracy of this procedure, a one-term approximation (*M* and *N* equal one) is used for Eq. (4.43), and the corresponding stiffness and mass terms are formulated. This one-term method is classically known as *Rayleigh's Method.* The resulting comparison function, u_1 is

$$u_1 = \sin\left(\frac{\pi x}{a}\right)\sin\left(\frac{\pi y}{b}\right) \tag{4.45}$$

From that, L and M are calculated in Eq. (4.46). Since M is a zero order operator, ρ is just multiplied by the comparison function, as the zero order derivative of u_1 is simply u_1. With that, L and M are found to be

$$\begin{aligned} L[u_1] &= P_x\left[\frac{\pi^2}{a^2}\sin\left(\frac{\pi x}{a}\right)\sin\left(\frac{\pi y}{b}\right)+\kappa\left(\frac{\pi^2}{b^2}\sin\left(\frac{\pi x}{a}\right)\sin\left(\frac{\pi y}{b}\right)\right)\right] \\ M[u_1] &= \rho\sin\left(\frac{\pi x}{a}\right)\sin\left(\frac{\pi y}{b}\right) \end{aligned} \tag{4.46}$$

For the rectangular membrane under consideration, the stiffness and mass surface integrals suggested by Eq. (4.33) are

$$\begin{aligned} k_{11} &= \int_0^b\int_0^a u_1 L[u_1]\,dxdy \\ m_{11} &= \int_0^b\int_0^a u_1 M[u_1]\,dxdy \end{aligned} \tag{4.47}$$

With the comparison function u_1 from above, the stiffness and mass entries are

$$\begin{aligned} k_{11} &= \frac{P_x\pi^2\left(b^2+\kappa a^2\right)}{4ab} \\ m_{11} &= \frac{ab\rho}{4} \end{aligned} \tag{4.48}$$

For these one-term stiffness and mass matrices, the eigenvalue problem expressed in Eq. (4.36) reduces such that

$$\begin{aligned} {}^1\Lambda &= \frac{k_{11}}{m_{11}} = \frac{P_x\pi^2\left(b^2+\kappa a^2\right)}{a^2b^2\rho} \\ &or \\ \omega_{11} &= \pi\sqrt{\frac{P_x}{\rho}\left(\left(\frac{1}{a}\right)^2+\kappa\left(\frac{1}{b}\right)^2\right)} \end{aligned} \tag{4.49}$$

One quickly notes that Eq. (4.49) is identical to Eq. (3.49), the natural frequency equation from the closed form solution for the case of m and n equal to one. As expected, when the true eigenfunctions are used as comparison functions, the Rayleigh Quotient provides exact results matching the closed-form solution.

Likewise, the eigenfunction corresponding to the eigenvalue from Eq. (4.49) is of course

$$w_{11} = a_{11} \sin\left(\frac{\pi x}{a}\right)\sin\left(\frac{\pi y}{b}\right) \tag{4.50}$$

As usual, the constant a_{11} can take any value to scale the mode shape as desired. Various normalization schemes exist to find expressions for a_{mn}; however, exact quantities are not of primary concern to the current research effort. This section used M and N equal to one in Eq. (4.43) so that a one-term approximation for the mode shape was employed to obtain the fundamental frequency of the membrane of interest. In general, M times N natural frequencies are obtained from the procedure outlined above. While the one-term approximation of the eigenfunction was useful for showing the accuracy of the Rayleigh-Ritz method, Section 4.4 uses larger values of M and N to expand Eq. (4.43) so that more natural frequencies can be approximated.

4.3 Finite Element Method for Bare Membrane:

As mentioned previously, the finite element software package ANSYS was used to analyze a prestressed rectangular membrane with fixed edges. However, up to this point, the derivations have been valid for a general set of rectangular membranes. That is, all of the geometric and physical properties of the membrane were left as variables. Even the tensions on the rectangle, derived from torus pressure vessel theory, were for any location on a torus of any size. For analytical expressions, it is preferable to have such general expressions for tensions, natural frequencies and the like so that results can easily be obtained and compared for a variety of torus geometries, coupon locations and sizes. However, finite elements are not applicable to such a broad range of solutions, rather they require geometric and physical properties to be specified numerically. At this point, one must select a specific torus to apply the stress analysis discussed in Chapter 2. Furthermore, a point at a specific radial location

on the torus R must be selected and finite sized rectangular coupon defined at that point.

4.3.1 Torus Geometry, Calculated Tensions and Coupon Selection:

Since the focus of this research is on satellites resembling the Spartan 207 seen in Figure 1.1, the geometric properties of this satellite presented in Coleman [1998] will be used, as presented in Table 4.1.

Table 4.1: Definition of Torus Variables

Variable	Definition	Value for Analysis	Units
r_t	Radius of revolution for toroidal shell	40	inches
r_1	Radius of torus	3	inches
R	Distance in radial direction	variable (37 to 43)	inches
t	Wall thickness	0.003	inches
p	Internal pressure	0.5	psi

As seen in Table 4.1, the radial location on the torus R can be selected as desired, with possible integer values being presented in Table 4.2.

Table 4.2: Radial Locations and κ Values

R, in.	κ
37	2.0811
38	2.0526
39	2.0256
40	2.0000
41	1.9756
42	1.9524
43	1.9302

From Eq. (2.12), the proportional relationship between the tensions κ presented in Table 4.2, depends only on radial location R and r_t from Table 4.1. For finite element verification, R is chosen to be forty inches was selected resulting in κ equal to 2.0. With these values, Eq. (2.11) is used to calculate P_x and P_y, the tensions in the x and y directions illustrated in Figure 2.7. The resulting values are

$$P_x = 0.75 \frac{lb}{in}$$
$$P_y = 1.5 \frac{lb}{in} \tag{4.51}$$

The last geometric properties of interest are the length and width of the rectangular coupon selected around the point where R equals forty inches on the torus, as seen in Figure 4.5.

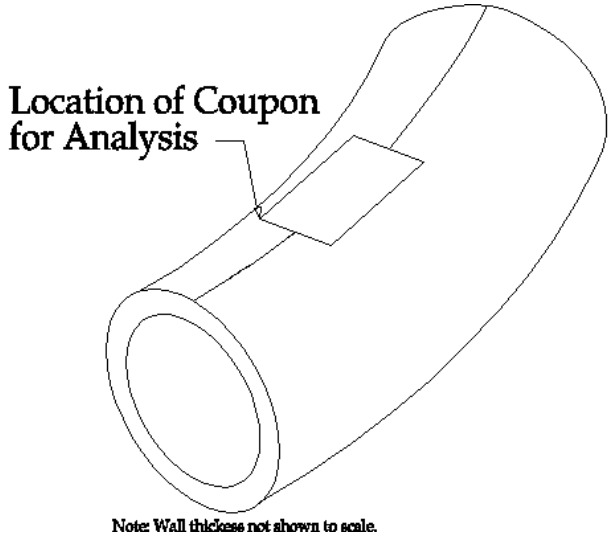

Figure 4.5: Location of Coupon for Finite Element Analysis

The dimensions of this element were arbitrarily chosen to be five inches by two and a half inches (a and b, respectively, per Figure 3.7). This is a reasonable size should experimental verification of the results be desired. Furthermore, when a PVDF patch is considered in Chapter 5, these dimensions are thought to be adequate to represent the material behavior far away from the patch. Choosing a

coupon of finite size requires the presumption that P_x and P_y are constant over their respective edges despite the slight variation of R. This is a reasonable presumption for the torus geometry of interest because the proportional relationship between the tensions, κ, varies by only about three percent in Table 4.2 for the values of R surrounding the selected value of forty inches.

4.3.2 Material Properties:

In addition to numerical values for the coupon size and tensions, finite element software requires the user to specify some basic material properties that are representative of the real member under consideration. As reported in Coleman [1998], the torus, and thus the coupon selected for analysis, is made from the polyimide film Kapton®, which is made from a polycondensation reaction between pyrometallic dianhydride and 4,4' diaminodiphenyl ether [DuPont GS-96-7]. It is a homogenous, isotropic material presumed to act in a linear-elastic manner for the low stress ranges of interest. Thus, the properties required to perform a modal analysis in ANSYS are displayed in Table 4.3 for Type HN film with 0.003 inch (3 mil) thickness at room temperature.

Table 4.3: Kapton® Material Properties for ANSYS

Property, symbol	Value	Units
Mass Density, ρ_m	1.328E-04	$lb\text{-}s^2/in^4$
Modulus of Elasticity, E	370000	psi
Poisson's Ratio, ν	0.34	-

4.3.3 ANSYS Finite Element Model:

The first step in creating the ANSYS finite element model was to define the five-inch by two-and-a-half-inch rectangle, similar to that of Figure 3.7. Next, the rectangle was meshed, that is, divided into connected elements of specified size. The effects of element size are discussed in Section 4.3.4. All of these elements were then defined to be membrane SHELL41 elements possessing the material

properties seen in Table 4.3. SHELL41 elements have no bending stiffness and three translational degrees of freedom at each node. A static solution was first performed to alter the original stiffness matrix to include the prestress effects of the tension in the membrane. Since the boundary conditions of interest are fixed, the static model, shown schematically in Figure 4.6, has the nodes along the *x*-axis restricted from translation in the *y* or *z* directions, while the nodes along the *y*-axis are restricted from translation in the *x* and *z* directions.

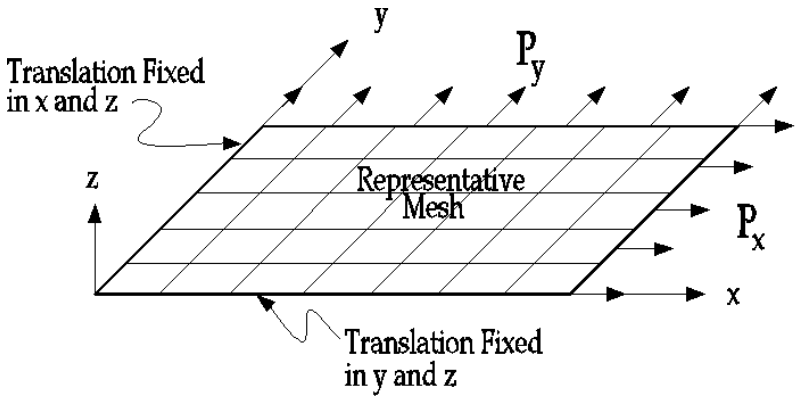

Figure 4.6: Static Model of Membrane with Unequal Tensions

While Figure 4.6 does not represent symmetric loading conditions, the reaction forces at the fixed lines will be equivalent to the applied tensions because the lines with applied tensions will remain linear after deformation. However, all deformation will occur away from the fixed lines. For a truly symmetric model, the center point would be fixed and all deformation would occur away from this stationary point. Symmetric loads become more important in Chapter 5 when the membrane does not deform uniformly along the edges. The unequal tensions P_x and P_y calculated in Eq. (4.51) were applied as pressures to the edges as shown. Application of a pressure load to a line implies units of force per unit length, which is the same as a tension applied to edge. The static solution was then found along with "prestress effects." After running the static solution, one could use the post-processor to ensure uniform linear deformation or check the

stress distribution within the material to show agreement with the pressure vessel analysis from Chapter 2.

After obtaining the prestressed stiffness matrix, the line pressures were removed and the nodes on every edge were restricted from translation in the x, y and z directions as shown in Figure 4.7.

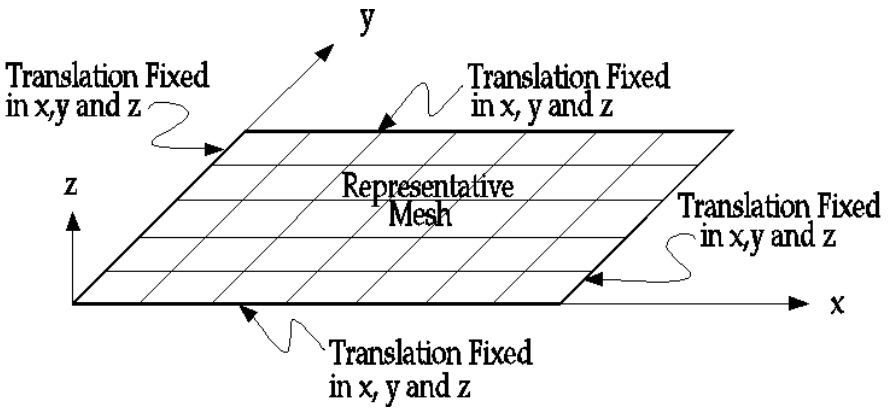

Figure 4.7: Dynamic Model of Prestressed Membrane

Next, a modal analysis solution was run with the "include prestress effects" option enabled. This option ensured that the software used the prestressed stiffness matrix obtained from the static solution. The first twenty natural frequencies and mode shapes were extracted and expanded. The natural frequencies were written to a separate file for printing, while the mode shapes were viewed in the post-processor. As expected, the mode shapes were combinations of sine waves identical to those produced from a three-dimensional plot of Eq. (3.50). These membrane mode shapes are well known and presented in most vibration texts.

4.3.4 Convergence of ANSYS Finite Element Model:

When using finite element software, it is critical to ensure that the desired results have converged. This is accomplished by first running test cases with fairly course meshing to ensure the model is properly constructed. Then the mesh is

gradually refined so that more elements are used in the solution. With each solution, the new results are compared to the previous case. As the number of elements is increased, the accuracy of the results will increase, as will the time required for the computer to perform the calculations. Eventually, increasing the number of elements will no longer change the results significantly, at which time the results are said to have converged. The procedure described in the previous section was followed several times for models with increasing number of elements. Figure 4.8 shows the four ANSYS models with an increasing number of elements.

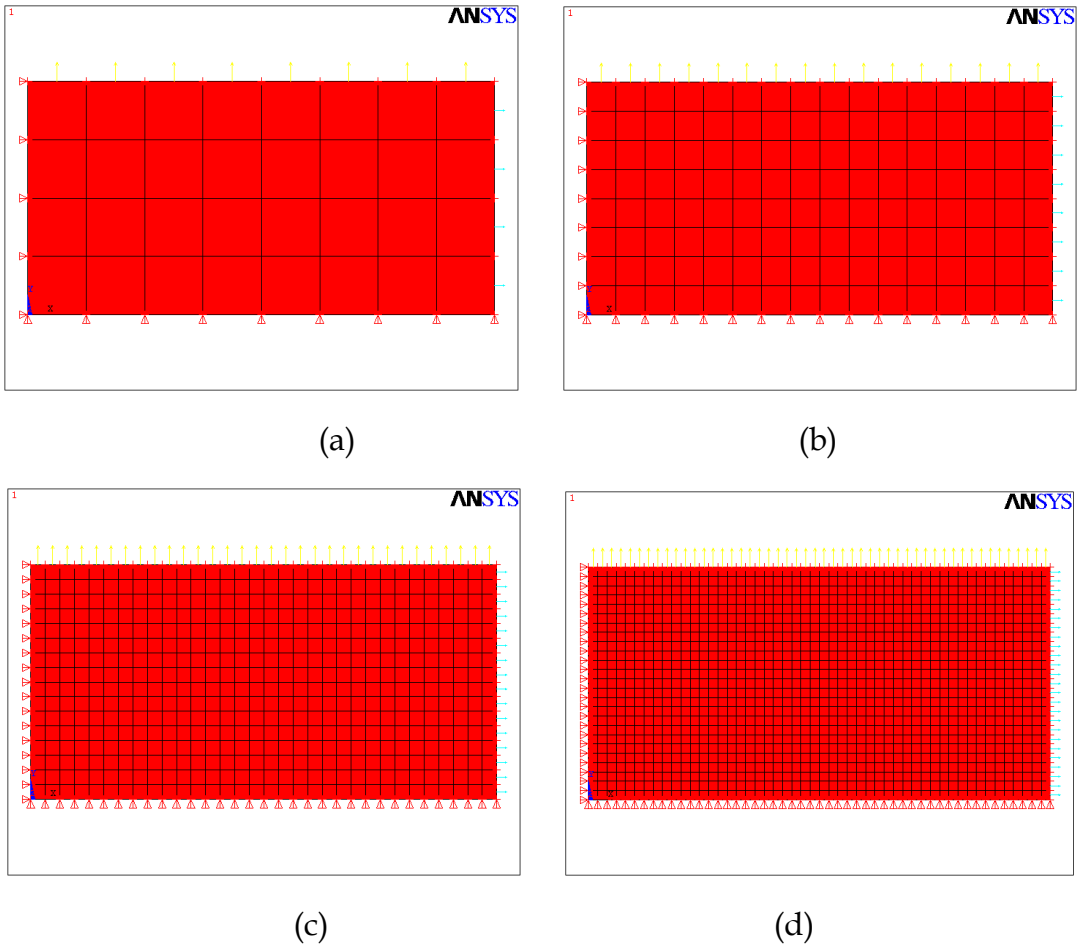

Figure 4.8: ANSYS Finite Element Model with (a) 32 Elements, 97 DOF (b) 128 Elements, 385 DOF (c) 512 Elements, 1533 DOF (d) 1250 Elements, 3747 DOF

Table 4.4 presents the first ten natural frequencies of the prestressed membrane for an increasing number of elements.

Table 4.4: Natural Frequencies of Prestressed Bare Membrane from ANSYS

Frequency Number	Number of Elements				Percent Change 512-1250
	32	128	512	1250	
	Natural Frequency, f, Hz				
1	421.44	414.11	412.28	412.07	0.051%
2	487.66	478.42	476.13	475.84	0.061%
3	590.22	571.86	567.31	566.62	0.122%
4	724.48	685.33	675.51	673.83	0.249%
5	867.03	808.12	793.23	790.60	0.333%
6	885.95	813.79	794.63	791.17	0.437%
7	901.07	842.89	828.22	825.63	0.314%
8	960.46	899.22	883.79	881.08	0.308%
9	1048.30	954.92	921.34	915.10	0.682%
10	1061.10	975.31	956.85	953.57	0.344%

From the small percent change values in the last column of Table 4.4, it is clear that the results have converged for a model containing 1250 elements. Therefore, the results from the 1250 element model will be used to compare with the other methods of analysis for this membrane.

4.4 Numerical Assessment of Approximation Methods:

At this point, three methods for analyzing the free-vibration characteristics of a bare membrane with fixed edges and tensions that vary by a constant factor in the x and y directions are presented. Chapter 3 uses Newton's Method to formulate the differential equation of motion for which an exact closed-form solution was found. In Chapter 4, energy methods are used along with variational calculus to determine the differential equation of motion for the same membrane as in Chapter 3. As expected, the equations of motion from Chapters 3 and 4 are identical. However, in Chapter 4, the Rayleigh-Ritz method was used

to approximate the natural frequencies and mode shapes without solving the equation of motion. Also Chapter 4 discusses the finite element software ANSYS that was used to construct a model of a particular membrane at a specific location on the torus described by Coleman [1998]. ANSYS was able to provide converged natural frequencies and mode shapes for the specific membrane of interest. Even though the results converged, the finite element method is still an approximation, as the membrane is not considered a continuous system, but rather a collection of many connected, discreet systems. Since an exact solution is readily available for the bare membrane, it is straightforward at this point to evaluate the accuracy of the two approximations methods.

Using Eq. (3.51), one can calculate the exact natural frequencies in radians per second for the a, b, P_x and κ values used in the previous section for the ANSYS finite element model. The density per unit area ρ from Eq. (3.51) is the mass density ρ_m from Table 4.3 times the membrane thickness t from Table 4.1, or

$$\rho = 3.9828x10^{-7}\,\frac{lb-s^2}{in^3} \tag{4.52}$$

With that, Table 4.5 is constructed with the exact results for the eight lowest natural frequencies from Chapter 3 appearing in the third column after conversion to Hz. A *Mathematica* notebook, shown in Appendix 2, was written with M and N equal to five to form the stiffness and mass matrices and solve for the eigenvalues per the Rayleigh-Ritz method of Section 4.2.5.2. While this computer code provided twenty-five (M times N) natural frequencies, only the lowest eight are presented in the fourth column of Table 4.5. The sixth column in Table 4.5 reports the eight lowest natural frequencies obtained from the 1250 element ANSYS model discussed in Section 4.3.

Even though twenty or more natural frequencies were calculated from the three methods used to form Table 4.5, only the first eight are presented in the interest

of brevity. In addition, the higher modes are not typically considered to be of much use or accuracy given the nature of the assumptions used to define such analytical models. Examples of these notions are small deflections, linear-elastic behavior and constant tensions in the x and y directions along the membrane edges [Meirovitch 1967].

Table 4.5: Numerical Comparison of Approximate and Exact Results

m	n	Natural Frequency, f_{mn}, Hz				
		Exact Solution	Rayleigh-Ritz Method[1]	Rayleigh-Ritz Percent Error	Finite Element Method[2]	Finite Element Percent Error
1	1	411.678	411.678	0.0000%	412.07	0.095%
2	1	475.365	475.365	0.0000%	475.84	0.100%
3	1	565.797	565.797	0.0000%	566.62	0.145%
4	1	672.267	672.267	0.0000%	673.83	0.232%
5	1	788.303	788.303	0.0000%	790.60	0.291%
1	2	788.303	788.303	0.0000%	791.17	0.364%
2	2	823.356	823.356	0.0000%	825.63	0.276%
3	2	878.675	878.675	0.0000%	881.08	0.274%

[1]25 Term Rayleigh-Ritz Approximation
[2]1250 Element Model

To assess the accuracy of the approximate methods, columns five and seven were constructed. These columns represent the percent error of the Rayleigh-Ritz and finite element approximation methods, respectively. Since the exact eigenfunctions were used as the comparison functions in Eq. (4.43), the Rayleigh-Ritz error is essentially zero. Column seven shows that the converged ANSYS finite element model predicted the eight lowest natural frequencies to within about one-third of one percent. Since the finite element method essentially uses a Rayleigh-Ritz type procedure with a different method for selecting comparison functions, the finite element predictions are slightly greater than the exact values. This trend is in agreement with the discussion following Eq. (4.28), demonstrating that the goal of minimizing the Rayleigh Quotient and thus converging onto the natural frequency from above has been achieved.

Another basis for comparison is the time and complexity involved in using these three methods. The closed-form solution, when possible is somewhat complicated but only takes a small amount of computer time to calculate numerical results. However, exact results are obtained. Similarly, the Rayleigh-Ritz method is complicated but requires about sixteen hours of computer calculation time for twenty-five frequencies with an extremely high level of accuracy. Lastly, the finite element analysis was much easier and straightforward for an experienced ANSYS user. Setup and computer calculation time for converged answers was completed in less than two hours. However, the results, while still highly accurate, displayed more error than the other two more complicated and time-consuming methods. As is the case with all engineering problems, there is a tradeoff between time invested and level of accuracy obtained.

Despite the questionable practical value of higher natural frequencies, it should be noted that the Rayleigh-Ritz and finite element methods produced natural frequencies to within one percent of the exact solution for their first twenty modes.

4.5 Summary:

Chapter 4 presents two popular methods for approximating the natural frequencies and mode shapes of a bare rectangular membrane with unequal direction dependent tension and fixed edges. Section 4.2 describes the energy methods and variational calculus that were used to develop the equation of motion and then derived and employed the Rayleigh-Ritz method to approximate the natural frequencies and mode shapes of the membrane. Section 4.3 describes the software package ANSYS that was used to construct a finite element model of a five-inch by two-and-a-half-inch membrane at a radial location R equal to forty inches on the torus. The unequal tensions in the

membrane were calculated from the pressure vessel analysis described in Chapter 2. A modal analysis was performed on finite element models with an increasing number of elements until the natural frequencies had converged. Section 4.4 summarizes the numerical results of the closed-form solution, the Rayleigh-Ritz method and the finite element software. The natural frequencies resulting from the two approximate methods were compared with those from the exact closed-form solution. While they involve differing amounts of complexity and time, both the Rayleigh-Ritz and finite element methods were found to predict the natural frequencies and mode shapes of the specific membrane described earlier with an extremely high degree of accuracy. Therefore, having demonstrated their proper implementation and accuracy, Chapter 5 applies both of these approximation methods to a system without a readily available closed-form solution, namely, a rectangular membrane with unequal x and y tensions, fixed edges and a passive PVDF attachment.

Chapter 5

Approximation Methods for Membrane with Passive PVDF Attachment

5.1 Introduction:

Chapter 4 discusses two popular methods that were used to approximate the natural frequencies and mode shapes of a bare rectangular membrane with fixed edges and unequal tensions in the x and y directions. Both the Rayleigh-Ritz and finite element methods were seen to produce highly accurate results. Chapter 5 discusses energy methods that were again used to develop an equation of motion for a similar rectangular membrane, only for this chapter, a PVDF patch was attached to the center of the membrane. It will be rigorously shown that traditional membrane theory is unable to account for the added stiffness of the PVDF patch. However, the additional mass of the patch is included in the model and its effects on the natural frequencies and mode shapes are investigated using the Rayleigh-Ritz method. In addition, the finite element software ANSYS is employed again to make a numerical assessment on the effects of the PVDF patch on the natural frequencies and mode shapes of the membrane. At this point, no wires will be attached to the piezopolymer patch, thus rendering the

PVDF passively attached to the base layer. Chapter 6 investigates the piezoelectric behavior of the patch.

5.2 Energy and Rayleigh-Ritz Methods for Membrane with PVDF Patch:

As seen in Chapter 4, derivation of the Rayleigh-Ritz method stems from deriving the equation of motion from energy expressions. Since only free vibrations are being considered currently, kinetic and potential energy expressions will be found for the rectangular membrane with a PVDF attachment shown in Figure 5.1.

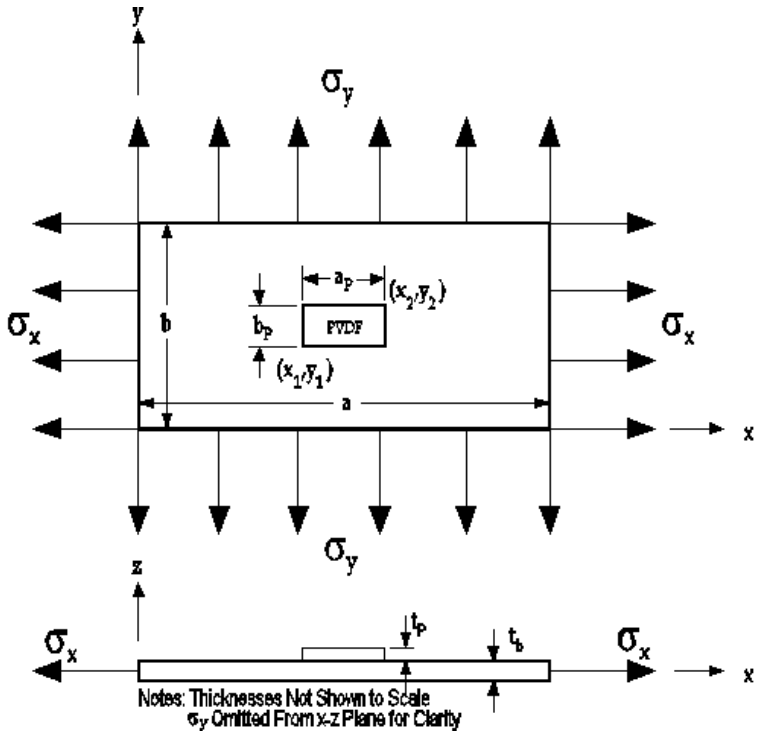

Figure 5.1: Rectangular Membrane with PVDF Attachment

Figure 5.1 is made under the presumption that the patch is attached to the structure prior to inflation. This is a reasonable presumption, lest the patch would have to be bonded and wired by an astronaut in orbit. Achieving a "perfect" bond between a piezoelectric device and a metal structure in a benign laboratory setting is difficult. Attempting to perform the attachment to an

inflated structure in a space suit while orbiting earth is clearly unreasonable with the current epoxy bonding techniques. If the patches are attached on the ground and the structure is inflated in orbit, the patch will also have some initial stress due to its being bonded to the satellite. It is under this presumption that Chapters 5 and 6 proceed.

With the potential and kinetic energy expressions, Hamilton's Principle in the form of Eq. (4.13) will again be employed. As was the case with the bare membrane in Chapter 4, the tension in the membrane shown in Figure 5.1 will be presumed different in two orthogonal directions. Furthermore, one recalls that tension is simply equal to a stress times the thickness of the material over which the stress is applied. Also, the PVDF patch is considered to have isotropic mechanical properties and behave in a linear elastic manner. Lastly but of equal importance is the presumption that the PVDF patch is rigidly and perfectly bonded to the base membrane layer. This presumption has two requirements that are critical to the subsequent energy analysis. First, the patch and base layer must have the same out-of-plane displacement $w(x,y,t)$ on the area over which the patch is applied. Second, similar to the requirements for Classical Laminated Plate Theory, the patch and the portion of the base membrane beneath the patch must deform alike along the interface between them in order to remain bonded together [Jones 1999]. Both of these requirements will be revisited and utilized in the derivation of the kinetic and potential energies.

5.2.1 Kinetic Energy:

As is typically the case for most dynamic systems, formulation of the kinetic energy expression for the layered membrane shown in Figure 5.1 is somewhat trivial. The total kinetic energy is simply the sum of the kinetic energies of the patch and the base membrane, with the latter being found in Eq. (4.2). The kinetic energy for the patch has a similar form with the density per unit area, ρ_P,

times the square of the velocity being integrated over the area of the patch only. As stated above, the base layer and patch must have the same out-of-plane displacement and consequently the same velocity, which appears as the partial derivative of w with respect to time in Eq. (5.1). Thus, the kinetic energy is

$$K = \int_0^b \int_0^a \frac{\rho}{2}\left(\frac{\partial w}{\partial t}\right)^2 dxdy + \int_{y_1}^{y_2} \int_{x_1}^{x_2} \frac{\rho_P}{2}\left(\frac{\partial w}{\partial t}\right)^2 dxdy \tag{5.1}$$

While this expression is mathematically correct, it is oftentimes more convenient to express energies in terms of a single integral over the entire domain of the system. Since the patch does not necessarily cover the entire base layer, Heaviside's function, $H(x\text{-}x_1)$, is used to mathematically size and locate the patch in the proper location. Heaviside's function is simply a unit step function that is equal to zero when its argument is negative and one when its argument is greater than or equal to zero. Heaviside's function has the ability to alter the limits of integration such that

$$\int_{-\infty}^{\infty} f(x)[\mathrm{H}(x-x_1)]dx = \int_{x_1}^{\infty} f(x)dx \tag{5.2}$$

Application of Heaviside's function alters the kinetic energy expression to

$$K = \int_0^b \int_0^a \left(\frac{\rho + \rho_P[\mathrm{H}(x-x_1)-\mathrm{H}(x-x_2)][\mathrm{H}(y-y_1)-\mathrm{H}(y-y_2)]}{2}\right)\left(\frac{\partial w}{\partial t}\right)^2 dxdy \tag{5.3}$$

From Eq. (5.3), it is clear that using Heaviside's function effectively "turns on" ρ_P over the patch area yet ignores this term while integrating over the rest of the base layer area. While Heaviside's function simplifies the mathematics conceptually and is included in most mathematical software packages, it is not usually numerically efficient, thus requiring excessive computer calculation time. Therefore, it is important to understand both forms of the kinetic energy expression when numerical calculations are performed later in this chapter.

5.2.2 Stress Distribution, Equilibrium and Strain Analysis:

From Section 4.2.2, it is known that a membranes potential energy is the surface integral over the membrane area of the tension times the stretching due to deflection. Using membrane theory to model an arbitrary coupon on the torus from Chapter 2 requires some simplifying presumptions that must be revisited at this point. In addition to having a constant value of tension in all directions, the traditional membrane analysis presented in most vibration texts assumes that the membrane consists of only one layer having uniform thickness and density. However, the system in Figure 5.1 consists of two membrane layers composed of potentially two different materials and sizes. This unequally sized layered configuration presents a much more complicated scenario that requires a modified set of presumptions. Clearly, the change in thickness and material properties in the area of the patch must be addressed, as this presents a deviation from traditional membrane analysis. Likewise, the tension will no longer have a constant value along the x and y-directions, but rather vary due to the ability of the attachment to sustain some of the loading. The stress acting at the outer edges of the larger base layer is due to the internal pressure loading as calculated in Chapter 2. However, the stress in the patch arises from being rigidly attached to the base layer. Understanding how the stress varies over this layered system is crucial to formulating the tensions required for the potential energy expressions.

With these points in mind, one develops the idea that the stress in the base layer is essentially the same as at the edges except in the region of the patch. In the area under the patch, the stress in the base layer drops as some of the load is transferred to the patch. According to the requirements set forth at the beginning of Section 5.2, the load must be split between the layers such that equal deformations take place in order to ensure the layers remain bonded together.

This idea about the stress distribution in the layers seems reasonable, but before proceeding with a force analysis, a simple static ANSYS finite element model was built to assess the stress distribution in the base layer. The base layer and loads were modeled exactly as in Section 4.3. The PVDF patch was one-inch by one-half-inch by 0.0005-inch thick and centered on the base layer as suggested by Figure 5.1. SHELL41 membrane elements possessing the material properties shown in Table 5.1 were used to represent the patch.

Table 5.1: PVDF Material Properties for ANSYS

Property, symbol	Value	Units
Mass Density, ρ_{mP}	1.664E-04	lb-s^2/in^4
Modulus of Elasticity, E_P	435113	psi
Poisson's Ratio, υ_P	0.33	-

The mass density is not needed for static analysis but required in Section 5.3 when a modal analysis is preformed. The documented value of Poisson's Ratio tends to vary between 0.3 and 0.33. However, these extreme values produce calculated stresses that vary by less than two percent. Figures 5.2 and 5.3, respectively, show the *x* and *y* stress distributions in the base layer.

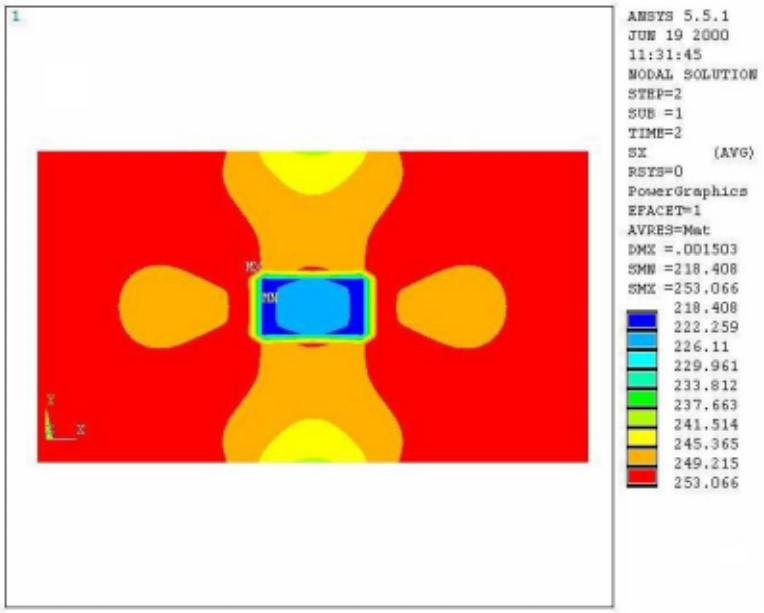

Figure 5.2: *x* Stress Distribution in Base Layer

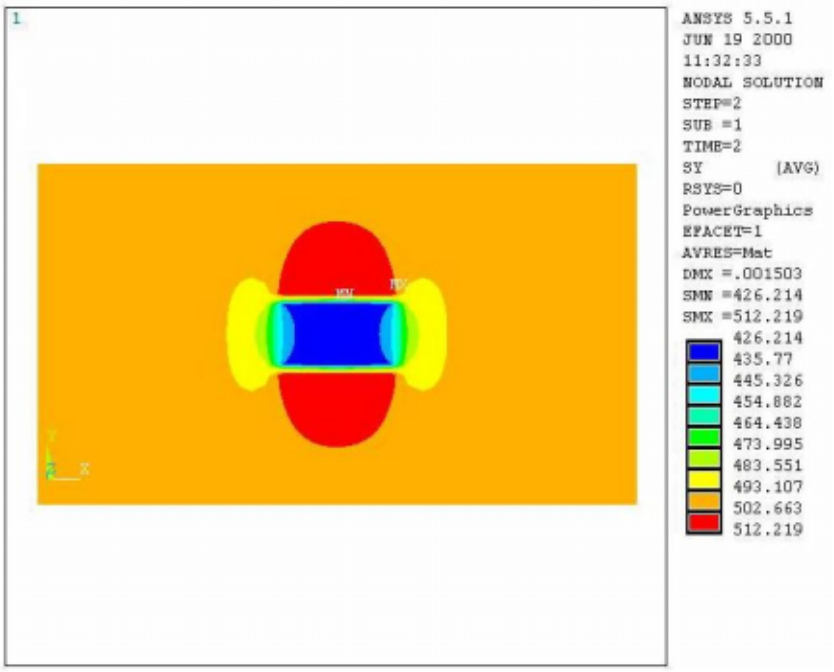

Figure 5.3: *y* Stress Distribution in Base Layer

Figures 5.4 and 5.5 show an enlarged view of the *x* and *y* stress distributions, respectively, in the patch.

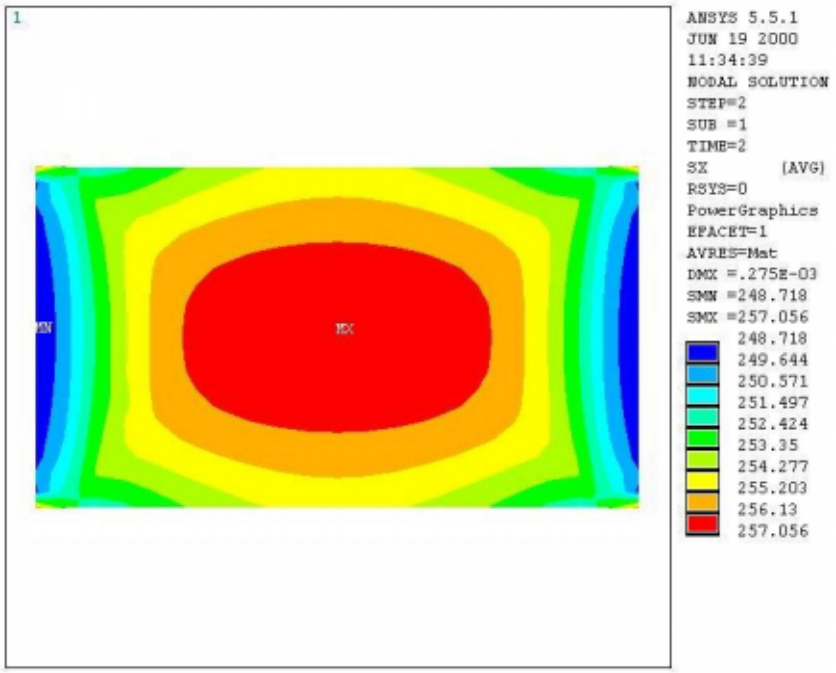

Figure 5.4: *x* Stress Distribution in the Patch

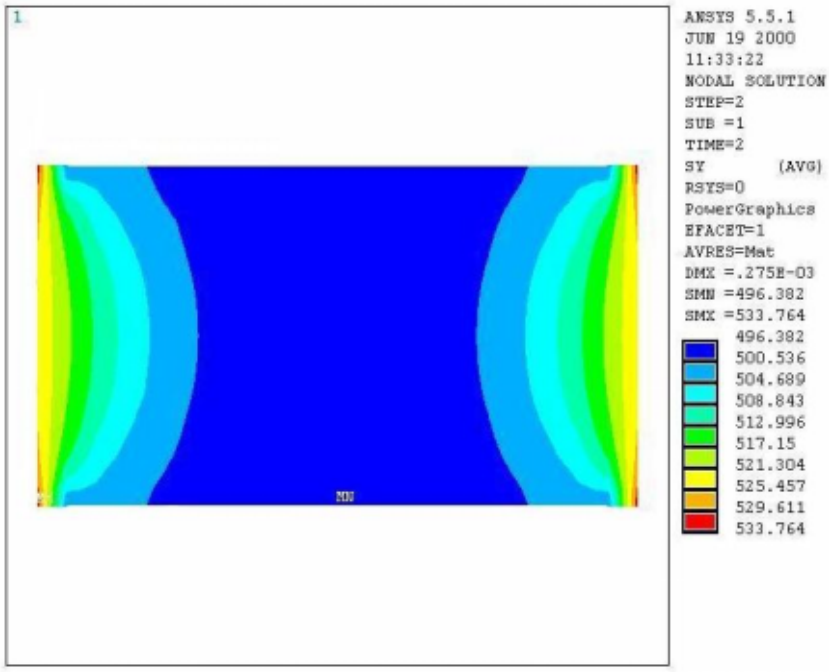

Figure 5.5: *y* Stress Distribution in the Patch

These finite element results support the stress distribution described above. While there is a gradual change in stress in the base layer around the patch, it is quite abrupt. Likewise, the patch stresses increase very rapidly from zero where there is no patch to fairly constant values over most of its area. With the force analysis that follows and the same numerical quantities used for the ANSYS finite element analysis, Figures 5.6 and 5.7 can be constructed to numerically assess the validity of presuming a step change in stress around the patch. From these figures, it is clear that modeling the stress changes using step functions closely predicts the stress variations in both the patch and base membrane layers.

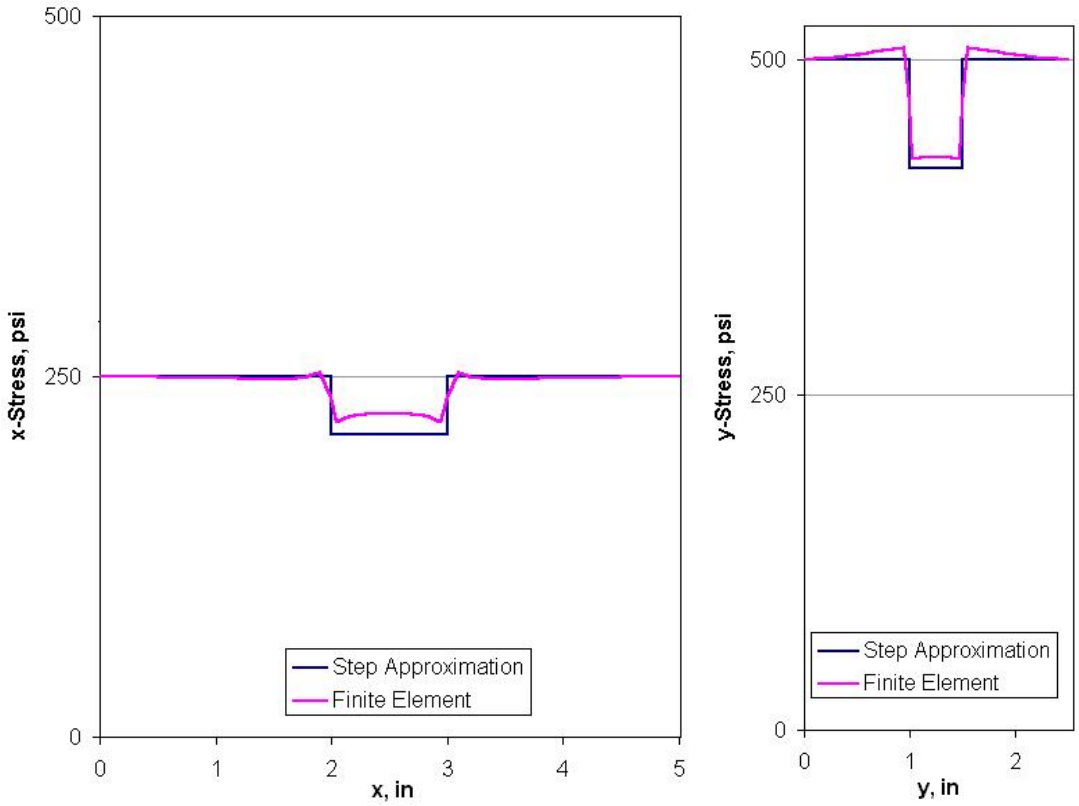

(a) (b)

Figure 5.6: Presumed Base Layer Stress Distribution and Finite Element Stress Prediction Along the Line

(a) $y=\frac{b}{2}$ (b) $x=\frac{a}{2}$

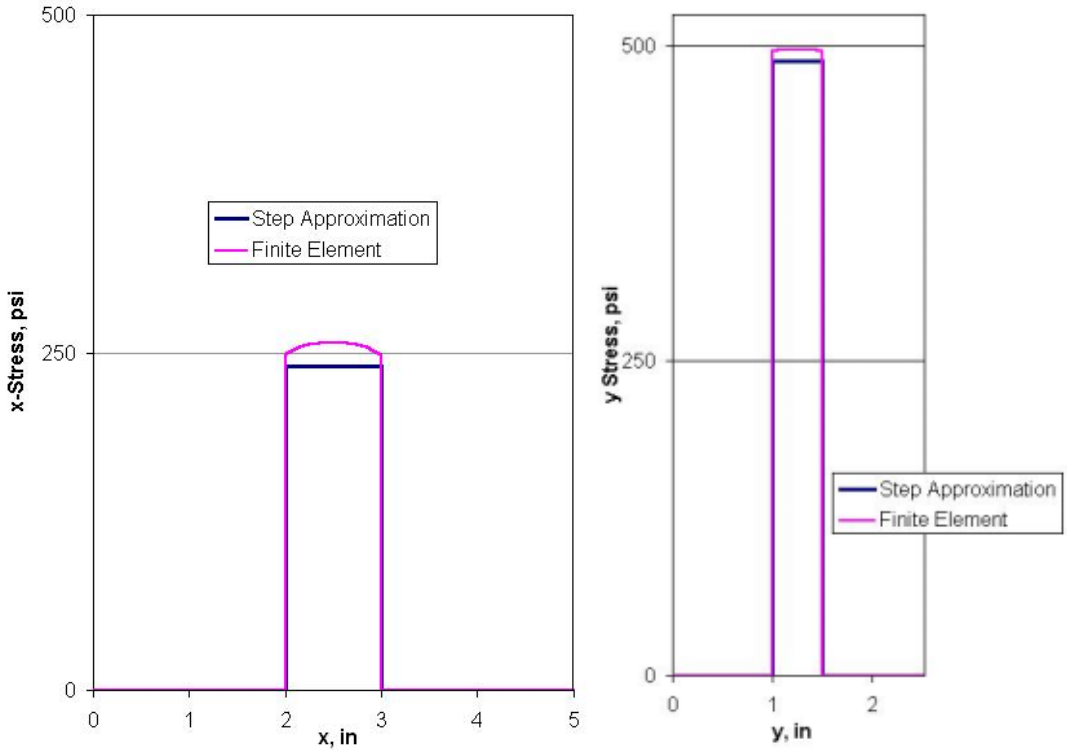

(a) (b)

Figure 5.7: Presumed Patch Layer Stress Distribution and Finite Element Stress Prediction Along the Line

(a) $y=\frac{b}{2}$ (b) $x=\frac{a}{2}$

Now that the stress distribution in the base layer and patch layer has been determined, the system can be sectioned and free body diagrams constructed. These fundamental yet critical engineering tools will allow expressions for the tensions acting at various locations in the two layers to be found. Each resultant force is simply the stress within the material times the cross sectional area over which the stress acts. After slicing the membrane system in Figure 5.1 through the middle of the centered patch parallel to the y-axis, Figure 5.8 reveals the forces acting in the x direction.

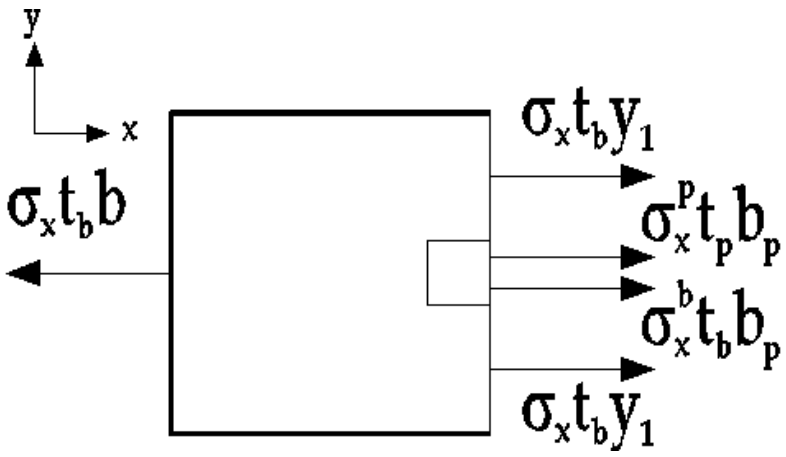

Figure 5.8: Free Body Diagram Showing *x* Direction Forces

To satisfy static equilibrium requirements, these forces must sum to zero:

$$\sum F_x = 0 : \sigma_x t_b b = 2\sigma_x t_b y_1 + \sigma_x^b t_b b_P + \sigma_x^P t_P b_P$$
$$where \sigma_x^b = x\ stress\ in\ base\ layer\ under\ patch \qquad (5.4)$$
$$and\ \sigma_x^P = x\ stress\ in\ patch$$

Next, the system in Figure 5.1 can be divided in half parallel to the *x*-axis to reveal forces acting in the *y* direction as shown in Figure 5.9.

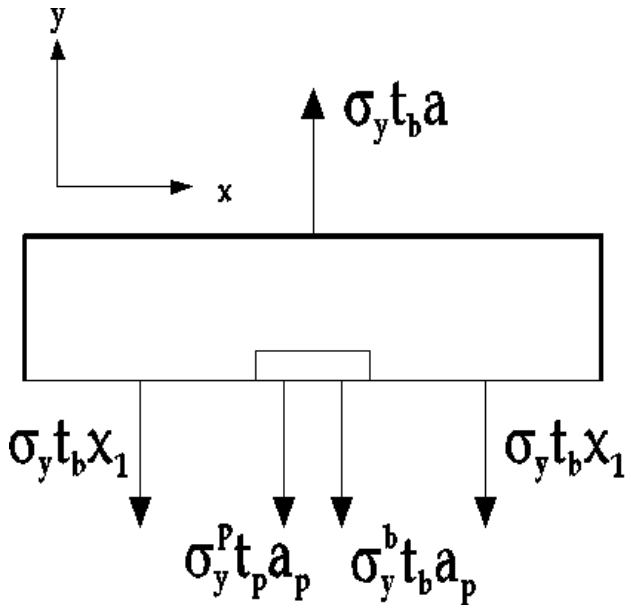

Figure 5.9: Free Body Diagram Showing *y* Direction Forces

Again, these forces must sum to zero:

$$\sum F_y = 0 : \sigma_y t_b a = 2\sigma_y t_b x_1 + \sigma_y^b t_b a_P + \sigma_y^P t_P a_P$$
$$\text{where } \sigma_y^b = y \text{ stress in baselayer under patch} \qquad (5.5)$$
$$\text{and } \sigma_y^P = y \text{ stress in patch}$$

At this point, enforcing static equilibrium in the *x* and *y* directions has yielded two equations and four unknowns, namely the *x* and *y* stresses in the patch and the base layer directly under the patch as indicated in Figures 5.6 and 5.7. The remaining variables are either stresses shown in Figure 5.1 and calculated from the pressure vessel analysis in Chapter 2 or geometric properties defined in Figure 5.1. Unfortunately, satisfying equilibrium does not offer any insight into how the load is distributed between the patch and the base layer. As is the case for most structures with more unknown forces than equilibrium equations, one must turn to a deformation analysis to obtain more information. In this case, it is known from a study of laminated materials that the deformation in the patch must equal the deformation in the base layer under the patch. Since these regions have the same dimensions, it suffices to say that their strains must be equal. In mechanics, Hooke's Law is generally used to relate stress and strain through a constitutive relationship. As seen in the stress distributions of Figures 5.6 and 5.7, the internal pressure of the torus creates a biaxial state of stress in both the patch and the base layer. Therefore, Hooke's Law must be applied in its biaxial form to account for Poisson contraction effects [Dowling 1999], shown generally to be

$$\varepsilon_x = \frac{1}{E}\left(\sigma_x - \nu\sigma_y\right)$$
$$\varepsilon_y = \frac{1}{E}\left(\sigma_y - \nu\sigma_x\right) \qquad (5.6)$$
$$\text{where } \nu = \text{Poisson's Ratio}$$

where ν is Poisson's ratio for the material of interest. With that, the strain in the *x* and *y* directions for each layer can be written and equated as

$$\varepsilon_x \to \frac{1}{E_b}\left(\sigma_x^b - \nu_b \sigma_y^b\right) = \frac{1}{E_P}\left(\sigma_x^P - \nu_P \sigma_y^P\right) \tag{5.7}$$

$$\varepsilon_y \to \frac{1}{E_b}\left(\sigma_y^b - \nu_b \sigma_x^b\right) = \frac{1}{E_P}\left(\sigma_y^P - \nu_P \sigma_x^P\right) \tag{5.8}$$

From this deformation analysis, there are now four equations, Eq. (5.4), Eq. (5.5), Eq. (5.7) and Eq. (5.8), and four unknowns that can be solved simultaneously to yield explicit equations for the desired stresses. This tedious exercise in linear algebra was performed in *Mathematica* with the following results:

$$\sigma_x^b = \frac{E_b t_b \left(a_P (b-2y_1)\left(E_P t_P (\nu_b \nu_P - 1) + E_b t_b \left(\nu_P^2 - 1\right)\right)\sigma_x - E_P b_P t_P (a-2x_1)(\nu_b - \nu_P)\sigma_y\right)}{a_P b_P \left(E_P^2 t_P^2 \left(\nu_b^2 - 1\right) + 2E_b E_P t_b t_P (\nu_b \nu_P - 1) + E_b^2 t_b^2 \left(\nu_P^2 - 1\right)\right)} \tag{5.9}$$

$$\sigma_y^b = \frac{E_b t_b \left(-a_P E_P t_P (b-2y_1)(\nu_b - \nu_P)\sigma_x + b_P (a-2x_1)\left(E_P t_P (\nu_b \nu_P - 1) + E_b t_b \left(\nu_P^2 - 1\right)\right)\sigma_y\right)}{a_P b_P \left(E_P^2 t_P^2 \left(\nu_b^2 - 1\right) + 2E_b E_P t_b t_P (\nu_b \nu_P - 1) + E_b^2 t_b^2 \left(\nu_P^2 - 1\right)\right)} \tag{5.10}$$

$$\sigma_x^P = \frac{E_P t_P \left(a_P (b-2y_1)\left(E_P t_P \left(\nu_b^2 - 1\right) + E_b t_b (\nu_b \nu_P - 1)\right)\sigma_x - E_b b_b t_b (a-2x_1)(\nu_b - \nu_P)\sigma_y\right)}{a_P b_P \left(E_P^2 t_P^2 \left(\nu_b^2 - 1\right) + 2E_b E_P t_b t_P (\nu_b \nu_P - 1) + E_b^2 t_b^2 \left(\nu_P^2 - 1\right)\right)} \tag{5.11}$$

$$\sigma_y^P = \frac{E_P t_P \left(a_P E_b t_b (b-2y_1)(\nu_b - \nu_P)\sigma_x + b_P (a-2x_1)\left(E_P t_P \left(\nu_b^2 - 1\right) + E_b t_b (\nu_b \nu_P - 1)\right)\sigma_y\right)}{a_P b_P \left(E_P^2 t_P^2 \left(\nu_b^2 - 1\right) + 2E_b E_P t_b t_P (\nu_b \nu_P - 1) + E_b^2 t_b^2 \left(\nu_P^2 - 1\right)\right)} \tag{5.12}$$

As they are somewhat tedious, these equations will not be used explicitly in subsequent derivations, but were used to obtain numerical results for Figures 5.6 and 5.7. Continuing with $\sigma_x^P, \sigma_y^P, \sigma_x^b$ and σ_y^b will offer the greatest benefit in terms of brevity as well as assist in uncovering an important simplification as one progresses into the potential energy derivation.

5.2.3 Potential Energy:

Now knowing the x and y stresses in the patch and base layer, one can readily calculate the tensions in the two layers at various locations and thus proceed with the derivation of the potential energy expressions. Since the tension at the base layer edge is not the same in the x and y directions, the potential energy in these directions will be considered independently as in Section 4.2.2. From these, it is known that potential energy is the surface integral of tension times the stretching due to deflection. Since the layers are rigidly bonded, they must stretch together, thus the binomial approximation for stretching in the x and y directions, Eq. (4.6) and (4.7) respectively, apply to both layers.

5.2.3.1 Potential Energy Derivation:

Considering the x direction first and carefully bounding the surface integrals over areas with the same tension, the potential energy in the x direction are expressed as

$$\begin{aligned} U_x = &\int_0^b \int_0^{x_1} \sigma_x t_b \left(ds_x - dx\right) dy + \int_0^{y_1} \int_{x_1}^{x_2} \sigma_x t_b \left(ds_x - dx\right) dy + \\ &\int_{y_1}^{y_2} \int_{x_1}^{x_2} \left(\sigma_x^b t_b + \sigma_x^P t_P\right)\left(ds_x - dx\right) dy + \int_{y_2}^{b} \int_{x_1}^{x_2} \sigma_x t_b \left(ds_x - dx\right) dy + \\ &\int_0^b \int_{x_2}^{a} \sigma_x t_b \left(ds_x - dx\right) dy \end{aligned} \tag{5.13}$$

Similarly, the potential energy due to tension in the y direction can be written as

$$\begin{aligned} U_y = &\int_0^b \int_0^{x_1} \sigma_y t_b \left(ds_y - dy\right) dx + \int_0^{y_1} \int_{x_1}^{x_2} \sigma_y t_b \left(ds_y - dy\right) dx + \\ &\int_{y_1}^{y_2} \int_{x_1}^{x_2} \left(\sigma_y^b t_b + \sigma_y^P t_P\right)\left(ds_y - dy\right) dx + \int_{y_2}^{b} \int_{x_1}^{x_2} \sigma_y t_b \left(ds_y - dy\right) dx + \\ &\int_0^b \int_{x_2}^{a} \sigma_y t_b \left(ds_y - dy\right) dx \end{aligned} \tag{5.14}$$

At this point, the equations from equilibrium, Eq. (5.4) and Eq. (5.5), are revisited and repeated here for clarity:

$$\sum F_x = 0 : \sigma_x t_b b = 2\sigma_x t_b y_1 + \sigma_x^b t_b b_P + \sigma_x^P t_P b_P \tag{5.4}$$

$$\sum F_y = 0 : \sigma_y t_b a = 2\sigma_y t_b x_1 + \sigma_y^b t_b a_P + \sigma_y^P t_P a_P \tag{5.5}$$

From the centered patch geometry defined in Figure 5.1, one can express the base layer dimensions as

$$b = 2y_1 + b_p \tag{5.15}$$

$$a = 2x_1 + a_p \tag{5.16}$$

Upon substitution of Eq. (5.15) into the left-hand side of Eq. (5.4) and Eq. (5.16) into the left-hand side of Eq. (5.5), the equilibrium equations simplify algebraically to

$$\sigma_x t_b = \sigma_x^b t_b + \sigma_x^P t_P \tag{5.17}$$

$$\sigma_y t_b = \sigma_y^b t_b + \sigma_y^P t_P \tag{5.18}$$

Under close inspection, one notes that the right hand side of Eq. (5.17) and Eq. (5.18) appears in the integrand of the third integral in each of the potential energy expressions, Eq. (5.13) and Eq. (5.14), respectively. Making these substitutions, the potential energy expressions become

$$\begin{aligned} U_x = &\int_0^b \int_0^{x_1} \sigma_x t_b \left(ds_x - dx\right) dy + \int_0^{y_1} \int_{x_1}^{x_2} \sigma_x t_b \left(ds_x - dx\right) dy + \int_{y_1}^{y_2} \int_{x_1}^{x_2} \sigma_x t_b \left(ds_x - dx\right) dy + \\ &\int_{y_2}^{b} \int_{x_1}^{x_2} \sigma_x t_b \left(ds_x - dx\right) dy + \int_0^b \int_{x_2}^{a} \sigma_x t_b \left(ds_x - dx\right) dy \end{aligned} \tag{5.19}$$

$$\begin{aligned} U_y = &\int_0^b \int_0^{x_1} \sigma_y t_b \left(ds_y - dy\right) dx + \int_0^{y_1} \int_{x_1}^{x_2} \sigma_y t_b \left(ds_y - dy\right) dx + \int_{y_1}^{y_2} \int_{x_1}^{x_2} \sigma_y t_b \left(ds_y - dy\right) dx + \\ &\int_{y_2}^{b} \int_{x_1}^{x_2} \sigma_y t_b \left(ds_y - dy\right) dx + \int_0^b \int_{x_2}^{a} \sigma_y t_b \left(ds_y - dy\right) dx \end{aligned} \tag{5.20}$$

At this point, the integrands of all five terms in each respective direction are seen to be identical, that is, having the same tension and stretching. Since the bounds on the surface integrals were written to cover the entire area of the base layer, the

potential energy in each direction can be written as a single surface integral bounded by the outer edges of the base layer so that

$$U_x = \int_0^b \int_0^a \sigma_x t_b \left(ds_x - dx\right) dy \tag{5.21}$$

$$U_y = \int_0^b \int_0^a \sigma_y t_b \left(ds_y - dy\right) dx \tag{5.22}$$

The stretching terms, in parentheses, can be simplified as in Section 4.2.2 using Eq. (4.6) and Eq. (4.7), respectively. Also, the tension terms, $\sigma_x t_b$ and $\sigma_y t_b$, are identical to P_x and P_y from previous chapters. Making these substitutions, along with constant relationship between P_x and P_y from Eq. (3.14), the total potential energy is expressed as the sum of the energies in the x and y directions, or

$$U = \int_0^b \int_0^a \frac{P_x}{2} \left[\left(\frac{\partial w}{\partial x} \right)^2 + \kappa \left(\frac{\partial w}{\partial y} \right)^2 \right] dx dy \tag{5.23}$$

5.2.3.2 Discussion of Potential Energy Expression:

Remarkably, Eq. (5.23) is the same potential energy expression as for the bare membrane seen in Eq. (3.14). From Section 4.2.5.2 it is known that the stiffness matrix will ultimately arise from this expression for potential energy. Thus, it has been shown that using membranes to model layered systems does not afford one the ability to account for the added stiffness of a patch. This situation arises from one of the fundamental membrane assumptions: the stress is constant along a given direction. In this context, constant means that the tension does not vary in a given direction, but of course, it can be different in other directions. However, the stress, and consequently the tension, in the base layer *cannot* be constant with a patch attachment, as verified in the stress analysis of Section 5.2. In addition, the aforementioned variation in Poisson's Ratio will not have any effect on the dynamic response of the layered system. To account for the added stiffness of an attached layer, one must instead use thin-plate theory with applied in-plane loading. However, the added mass of the patch is accounted for in the

expression for kinetic energy, Eq. (5.3). While this added mass does not affect the static properties of the system, it does alter the dynamic response. With this inherent limitation of membrane theory in mind, one can proceed to study the impact of the added mass of the patch on the natural frequencies and mode shapes of the layered system.

5.2.4 Hamilton's Principle:

At this point, one can employ Hamilton's Principle as discussed in Section 4.2.3. With the kinetic and potential energy expression in Eq. (5.3) and Eq. (5.23), respectively, application of Hamilton's Principle, Eq. (4.13), yields the functional

$$I = \int_{t_1}^{t_2}\int_0^b\int_0^a \left[\left(\frac{\rho+\rho_P\left[\mathrm{H}(x-x_1)-\mathrm{H}(x-x_2)\right]\left[\mathrm{H}(y-y_1)-\mathrm{H}(y-y_2)\right]}{2}\right)\left(\frac{\partial w}{\partial t}\right)^2 - \frac{P_x}{2}\left[\left(\frac{\partial w}{\partial x}\right)^2+\kappa\left(\frac{\partial w}{\partial y}\right)^2\right]\right] dxdydt \tag{5.24}$$

As before, the equation of motion will produce an extremum value to Eq. (5.24). Again, variational calculus will be used to find the partial differential equation of motion.

5.2.5 Variational Methods to Determine Equation of Motion:

Similar to Section 4.2.4, Eq. (5.24) has an extremum value when its first variation equals zero:

$$\delta^{(1)}\left(\int_{t_1}^{t_2}\int_0^b\int_0^a \left[\left(\frac{\rho+\rho_P\left[\mathrm{H}(x-x_1)-\mathrm{H}(x-x_2)\right]\left[\mathrm{H}(y-y_1)-\mathrm{H}(y-y_2)\right]}{2}\right)\left(\frac{\partial w}{\partial t}\right)^2 - \frac{P_x}{2}\left[\left(\frac{\partial w}{\partial x}\right)^2+\kappa\left(\frac{\partial w}{\partial y}\right)^2\right]\right] dxdydt\right) = 0 \tag{5.25}$$

Since the functional I has the same general form as the functional in Eq. (4.16), repeated here for clarity, the procedure of Section 4.2.4 will be followed as found in Magrab [1979]:

$$I(w)=\int_{t_1}^{t_2}\iiint F\left(x,y,t,w,\dot{w},w_x,w_y\right)dxdydt$$
$$where \quad \dot{w}=\frac{\partial w}{\partial t}, \quad w_x=\frac{\partial w}{\partial x}, \quad w_y=\frac{\partial w}{\partial y} \tag{4.16}$$

For the rectangular system depicted in Figure 5.1, the first variation of Eq. (4.16) is shown from Eq. (4.17) as

$$\delta^{(1)}\left[I(w)\right]=\int_{t_1}^{t_2}\left[\iint_D \eta\left(\Im_1(w)-\Im_2(\dot{w})\right)dD+\int_S \eta B_1(w)ds\right]dt=0 \tag{4.17}$$

where

$$\Im_1(w)=F_w-\frac{\partial F_{w_x}}{\partial x}-\frac{\partial F_{w_y}}{\partial y}, \quad \Im_2(\dot{w})=\frac{\partial F_{\dot{w}}}{\partial t},$$
$$B_1(w)=F_{w_n}, \quad D=Surface, \quad S=boundaries$$

In order to satisfy Eq. (4.17) and consequently find the desired extremum point, the following two conditions must be met:

$$(a)\ \Im_1(w)-\Im_2(\dot{w})=0 \quad membrane\ interior$$
$$(b)\ \oint_S \eta\, B_1(w)ds=0 \quad membrane\ boundary \tag{4.18}$$

With *F* defined in the integrand of Eq. (5.24), one can take the partial derivative specified in Eq. (4.17) to form the two terms of Eq. (4.18) (a):

$$\Im_1(w)=P_x\left(\frac{\partial^2 w}{\partial x^2}\right)+P_x\kappa\left(\frac{\partial^2 w}{\partial y^2}\right)$$
$$\Im_2(\dot{w})=\left(\rho+\rho_P\left[\mathrm{H}(x-x_1)-\mathrm{H}(x-x_2)\right]\left[\mathrm{H}(y-y_1)-\mathrm{H}(y-y_2)\right]\right)\left(\frac{\partial^2 w}{\partial t^2}\right) \tag{5.26}$$

Now, Eq. (4.18) (a) yields the equation of motion for the layered membrane system:

$$\left(\rho+\rho_P\left[\mathrm{H}(x-x_1)-\mathrm{H}(x-x_2)\right]\left[\mathrm{H}(y-y_1)-\mathrm{H}(y-y_2)\right]\right)\left(\frac{\partial^2 w}{\partial t^2}\right)=$$
$$P_x\left[\left(\frac{\partial^2 w}{\partial x^2}\right)+\kappa\left(\frac{\partial^2 w}{\partial y^2}\right)\right] \tag{5.27}$$

In the same manner as Section 4.2.4, Eq. (4.18) (b) is used to specify the boundary conditions with the definition of $B_1(w)$ from Eq. (4.17). Repeating from Eq. (4.22):

$$\oint_S \eta F_{w_n} ds = 0 \tag{4.22}$$

Just as before, one of the two terms inside the integral must be zero for this equation to be satisfied. If η equals zero, the fixed kinematic boundary condition results again as

$$\eta = 0, \ \textit{thus } w = \textit{presribed value} \tag{4.23}$$

If the second term equals zero, the result is the same free boundary condition,

$$\begin{aligned} &P_x\left(\frac{\partial w}{\partial x}\right) = 0 \ \textit{along } x = 0 \ \textit{and } x = a \\ &\textit{and } P_x \kappa\left(\frac{\partial w}{\partial y}\right) = 0 \ \textit{along } y = 0 \ \textit{and } y = b \end{aligned} \tag{4.25}$$

Again, either Eq. (4.23) or Eq. (4.25) must be met at each point on the membrane boundary. Even though the system under consideration consists of two layers, the added patch has no effect on the boundary conditions as would be expected. Physically, it stands to reason that the addition of a patch would not change a membrane edge from being either fixed or free.

5.2.6 Rayleigh-Ritz Method:

Section 4.2.5 presents a thorough derivation and application of the Rayleigh-Ritz method as it applies to membrane vibrations. Instead of repeating this, only the information necessary to formulate the mass and stiffness matrices required to solve the eigenvalue problem is presented. The first step is to select a set of comparison functions that form the basis of the approximated eigenfunctions. Since the membrane with the PVDF attachment is expected to vibrate in a manner somewhat similar to the bare membrane, the exact eigenfunctions of the bare membrane are selected and written as

$$w_i = \sum_{i=1}^{M*N} a_i u_i = \sum_{m=1}^{M}\sum_{n=1}^{N} a_{mn} \sin\left(\frac{m\pi x}{a}\right)\sin\left(\frac{n\pi y}{b}\right) \quad i = 1, 2, \ldots M * N \tag{4.43}$$

From the derivation leading to Eq. (4.44), the eigenvalues for the out-of-plane vibrations of the system in Figure 5.1 are given by

$$\omega_{ij}{}^2 = \Lambda_{ij} = \frac{\int_0^b \int_0^a w_i L[w_j]\,dxdy}{\int_0^b \int_0^a w_i M[w_j]\,dxdy}$$

$$where \quad L = -P_x\left[\left(\frac{\partial^2}{\partial x^2}\right) + \kappa\left(\frac{\partial^2}{\partial y^2}\right)\right] \tag{5.28}$$

$$and \quad M = (\rho + \rho_P[\mathrm{H}(x-x_1) - \mathrm{H}(x-x_2)][\mathrm{H}(y-y_1) - \mathrm{H}(y-y_2)])$$

While this form is correct, using mathematical software to perform such computations could require a great deal of time. In the interest of forthcoming numerical calculations, two M operators will be defined. M^b will represent the base layer's mass properties and M^P will cover the patch layer's mass properties, allowing the denominator to be broken up into two integrals without using Heaviside's functions. With that, the eigenvalues are defined as

$$\omega_{ij}{}^2 = \Lambda_{ij} = \frac{\int_0^b \int_0^a w_i L[w_j]\,dxdy}{\int_0^b \int_0^a w_i M[w_j]\,dxdy + \int_{y_1}^{y_2} \int_{x_1}^{x_2} w_i M[w_j]\,dxdy} \tag{5.29}$$

$$where \quad L = -P_x\left[\left(\frac{\partial^2}{\partial x^2}\right) + \kappa\left(\frac{\partial^2}{\partial y^2}\right)\right] \quad M^b = \rho \text{ and } M^P = \rho_P$$

As suggested by Eq. (4.33), the entries in the mass and stiffness matrices for the system with natural frequencies presented in Eq. (5.29) are

$$\begin{aligned} k_{ij} &= \int_0^b \int_0^a u_i L[u_j]\,dxdy \\ m_{ij} &= \int_0^b \int_0^a u_i M^b[u_j]\,dxdy + \int_{y_1}^{y_2} \int_{x_1}^{x_2} u_i M^P[u_j]\,dxdy \end{aligned} \tag{5.30}$$

With the comparison functions from Eq. (4.43) and the definitions for L, M^b and M^P from Eq. (5.29), the mass and stiffness matrices can be constructed per Eq. (5.30). With these matrices in hand, one can use one of the many methods for solving the traditional eigenvalue problem presented in Eq. (4.36), repeated here as

$$\left([k]-{}^{n}\Lambda[m]\right)\{a\}=0 \tag{4.36}$$

This equation can be used to first find the eigenvalues by setting the determinate of the term in parentheses equal to zero and solving for the different Λ values. Once the eigenvalues are known, they can be substituted back into Eq. (4.36) and the eigenvectors, $\{a\}$ can be found.

Since a closed-form solution is not available to the equation of motion, Eq. (5.27), continuing symbolically with even a one-term eigenvalue approximation as in Section 4.2.5.2 would not help validate the derivation presented above. Instead, the equations in this section will be employed to make a numerical comparison with the finite element model analyzed in the following section.

5.3 Finite Element Method for Membrane with PVDF Patch:

The finite element software package ANSYS was used to analyze a rectangular membrane with fixed edges, tensions that are different in two orthogonal directions and a PVDF patch rigidly attached and centered.

5.3.1 Geometric and Material Properties:

As discussed in Section 4.3, numerical values for all geometric and material properties are required for a finite element analysis. For the sake of making a comparison between the bare membrane and the membrane with a PVDF attachment, the same torus geometry was used for both finite element models as defined in Table 4.1. Also, the point selected for analysis was again at R equal to forty inches, as seen in Figure 4.5, and the coupon sized to be five inches by two and a half inches. With these quantities defined numerically, σ_x and σ_y as illustrated in Figure 2.6 are found from Eq. (2.8) and Eq. (2.9), respectively, to be

$$\begin{aligned}\sigma_x &= 250\ psi\\ \sigma_y &= 500\ psi\end{aligned} \tag{5.31}$$

The tension, P_x and P_y are found by multiplying the appropriate stress times the thickness of the base layer. For the numerical values being used presently, these tensions are

$$P_x = 0.75 \frac{lb}{in}$$
$$P_y = 1.5 \frac{lb}{in} \tag{5.32}$$

The material properties for the Kapton® base membrane are specified in Table 4.3, while the PVDF patch properties are given in Table 5.1. The patch was selected to be one-fifth the size of the base layer and centered. From the notation defined in Figure 5.1, Table 5.2 presents the selected dimensions and location for the PVDF patch.

Table 5.2: PVDF Patch Geometry and Location

Dimension	Value	Units
a_p	1.0	inch
b_p	0.5	inch
t_p	0.0005	inch
x_1	2.0	inches
y_1	1.0	inch

These values represent a one-fifth sized patch in the center of the base layer.

5.3.2 ANSYS Finite Element Model:

The first step in creating the layered ANSYS finite element model was to define the nine areas shown in Figure 5.10.

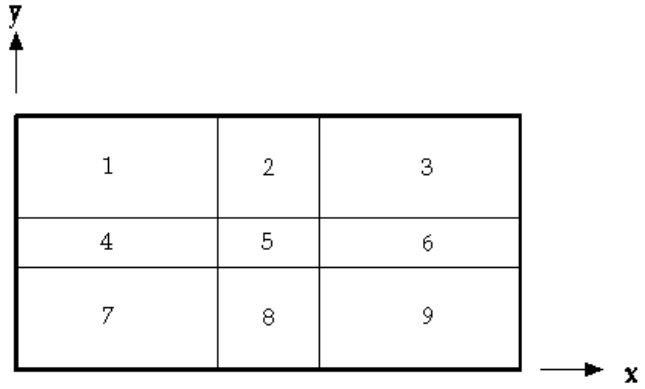

Figure 5.10: Areas Required to Represent Membrane with PVDF Patch

Each of these nine internal rectangles was then meshed with SHELL41 membrane elements to represent the base layer. Thus, Kapton® material properties were specified along with the thickness of the base layer from Table 4.1. This meshing procedure automatically created nodes at the corners of every element. SHELL41 membrane elements with PVDF material and geometric properties were then created over top of the elements in area 5 from Figure 5.10 but defined to share nodes with the base layer in this region. Forcing these elements to share nodes ensures that the two layers are rigidly bonded together. Again, a static solution was sought first to alter the original stiffness matrix to include the effects of the tension loading in the membrane. A quarter model with symmetric boundary conditions could be used for the static analysis to save computation time. However, the entire layered system is relatively simple from a finite element software point of view and requires less than thirty seconds to solve even the most refined model used. Furthermore, selecting the proper symmetric boundary conditions for such reduced models for modal analysis is often difficult leading to undesirable results. With the entire system defined as described above, the boundary conditions are now reconsidered as they differ from those in Section 4.3.3 since the layered system will not deform uniformly. Since the patch lowers the load in the base layer under the patch, one expects less deformation in the middle of the edges. Thus, all nodes along two edges cannot

be restricted from motion in the *x*-y plane as in Figure 4.6. Instead, the center node is fixed in the *x* and *y* directions and the middle node along the right edge is fixed in the *y* direction. All edges are then fixed in the *z* direction since out-of-plane deflections are not possible for in-plane tensions in a static sense. These boundary conditions are shown schematically in Figure 5.11.

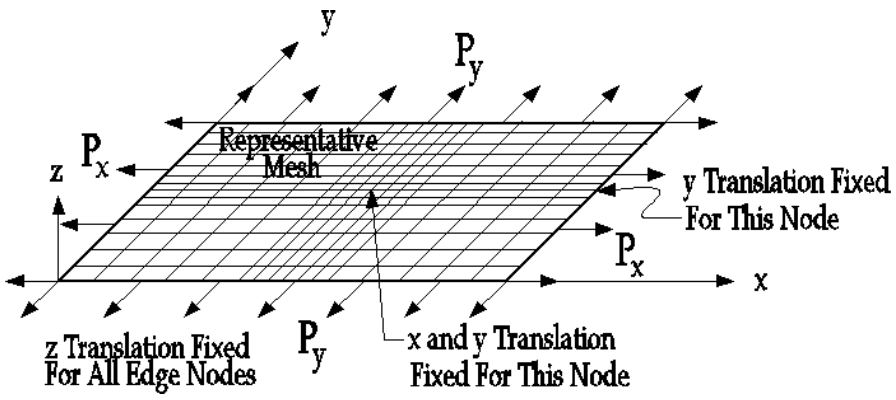

Figure 5.11: Static Model of Membrane with PVDF Attachment

The center node will not move as it lies on two lines of symmetry, one parallel to the *x*-axis and the other parallel to the *y*-axis. Fixing this node as indicated restricts rigid body motion in the *x* and *y* directions. The other node that is fixed in the *y* direction will only move in the *x* direction, as it is also on the line of symmetry parallel to the *x*-axis. Fixing this node as such restricts rigid body rotation in the *x*-*y* plane. After running the static solution to account for prestress effects, the post processor was consulted to ensure a symmetric deflection and stress distribution as shown in Figures 5.2 through 5.5. Next, the static boundary conditions and tensions were removed and all edge nodes fixed in the *x*, *y* and *z* directions as shown schematically in Figure 5.12.

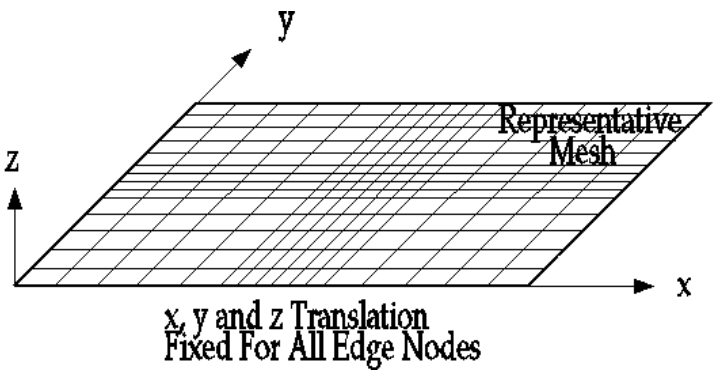

Figure 5.12: Dynamic Model of Membrane with PVDF Attachment

At this point, a modal analysis was performed with the "include prestress effects" option enabled. This ensured that the prestressed matrix generated by the static solution was used in the dynamic analysis. The first ten modes were extracted and expanded, and the natural frequencies were written to a separate file for printing. The mode shapes were viewed in the post-processor as found to be quite similar to those of the bare membrane. This adds credibility to the assumed eigenvectors for the Rayleigh-Ritz method from Eq. (4.43) in Section 5.2.6.

5.3.3 Convergence of ANSYS Finite Element Model:

As described in Section 4.3.4, the finite element model of the layered system considered in Section 5.3 was run multiple times with an increasing number of elements until the natural frequencies were seen to converge. Figure 5.13 shows three ANSYS models with an increasing number of elements.

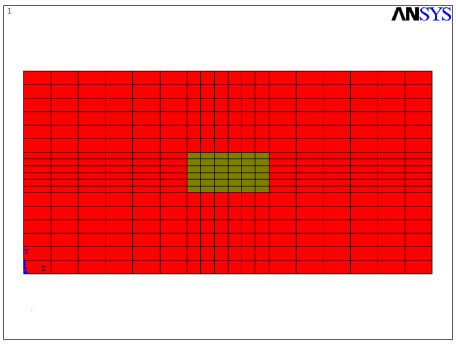

(a)

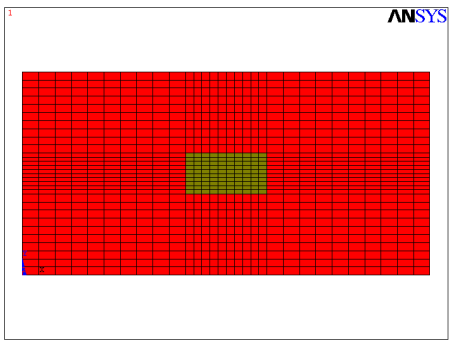

(b)

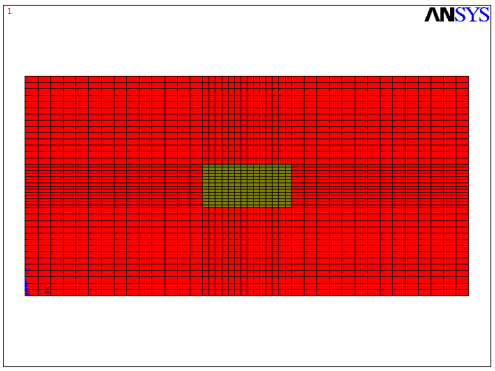

(c)

Figure 5.13: ANSYS Finite Element Model with (a) 360 Elements, 855 DOF (b) 1000 Elements, 2511 DOF (c) 1960 Elements, 5031 DOF

Table 5.3 presents the first ten natural frequencies of the prestressed membrane with a one-fifth sized PVDF attachment and fixed edges for an increasing number of elements obtained from ANSYS. The particularly small percent change values seen in the column at the far right of Table 5.3 reveal that the natural frequency results have converged for a model with 1960 elements. Thus, the frequencies from the 1960 elements column will be used to compare with the bare membrane and the Rayleigh-Ritz method for the layered system.

Table 5.3: Natural Frequencies of Membrane with PVDF Patch

Frequency Number	Number of Elements			Percent Change 1000-1960
	360	1000	1960	
	Natural Frequency, f, Hz			
1	405.94	405.63	405.54	0.022%
2	475.66	474.71	474.45	0.055%
3	563.98	561.44	560.73	0.127%
4	680.13	672.71	670.67	0.304%
5	792.45	788.99	787.35	0.208%
6	806.32	791.41	788.04	0.428%
7	827.76	824.05	823.04	0.123%
8	885.26	880.61	879.32	0.147%
9	941.10	916.90	910.04	0.754%
10	962.03	953.89	951.65	0.235%

5.4 Numerical Comparison of Rayleigh-Ritz and Finite Element Methods:

Section 5.2 describes the development of the equation of motion for a membrane with a passive PVDF patch using energy methods. While membrane theory was unable to account for the extra stiffness of the patch, the additional mass of the patch was considered. This equation of motion is valid for an arbitrary coupon size and location on the torus structure as well as arbitrary patch size and location on the coupon. From this equation, the Rayleigh-Ritz method was used to formulate the appropriate mass and stiffness matrices for the layered system. After forming these matrices, a traditional eigenvalue problem can be set up and solved. Thus the natural frequencies and mode shapes are obtained without directly solving the partial differential equation of motion. Also, Section 5.3 describes using ANSYS to predict the natural frequencies and mode shapes of the layered membrane.

To compare the results of these two methods, the numerical values for a, b, P_x, κ, x_1, x_2, y_1 and y_2 discussed in Section 5.3 and used to create the finite element model were used to form the mass and stiffness matrices derived from the Rayleigh-Ritz method in Section 5.2.6. Again, care must be taken to apply the mass densities from Table 4.3 and Table 5.1 on a per-unit-area basis. This is accomplished simply by multiplying by the thickness of the appropriate layer. The values corresponding to the numerical comparison at hand are

$$\rho = 3.984x10^{-7}\ \frac{lb-s^2}{in^3}$$
$$\rho_P = 8.3204x10^{-8}\ \frac{lb-s^2}{in^3} \tag{5.33}$$

A *Mathematica* code was written to formulate the approximate eigenfunctions from Eq. (4.43), calculate the L, M^b and M^P operators and compute the entries of the mass and stiffness matrices per Eq. (5.30). This program, shown in Appendix 3, also solved the eigenvalue problem of Eq. (4.36) and transformed the results into natural frequencies and mode shapes of the layered system. Table 5.4

presents a numerical comparison of the two methods. A twelve term (M=6, N=2) expansion of the eigenfunctions approximated by Eq. (4.43) was used to produce the Rayleigh-Ritz column. A 1960 element ANSYS model was used to produce the Finite Element Method column.

Table 5.4: Comparison of Rayleigh-Ritz and Finite Element Methods

		f_{mn}, Hz		
m	n	Rayleigh-Ritz Method[1]	Finite Element Method[2]	Percent Difference (RR-FEA)
1	1	405.192	405.54	-0.086%
2	1	474.416	474.45	-0.007%
3	1	559.365	560.73	-0.244%
4	1	668.084	670.67	-0.387%
5	1	782.471	787.35	-0.624%
1	2	786.735	788.04	-0.166%
2	2	823.151	823.04	0.013%
3	2	877.355	879.32	-0.224%
6	1	902.126	910.04	-0.877%
4	2	949.988	951.65	-0.175%

[1]12 Term Rayleigh-Ritz Approximation
[2]1960 Element Model

The fractions of a percent difference seen in the far right column indicate that both approximation methods agree remarkably well. This leads to the realization that neither the Rayleigh-Ritz nor the finite element solution was able to account for the added stiffness of the patch. Since membrane elements were specified in ANSYS for both the base and patch layer, one gains additional confidence in the types of predefined elements in this software package. As both of the methods used in Chapter 5 are approximations and no exact solution is available, neither results column can be said to converge from above. One can only say that the exact natural frequencies are less than the ones presented in Table 5.4. If one compares these results to the natural frequencies of the bare membrane in Table 4.5, an appreciable yet small amount of difference is noted. The significance of these changes is addressed formally in Chapter 7. Also, while

no formal comparison was made between the mode shapes of the two systems, a visual assessment showed practically identical shapes.

As in Section 4.4, the time and complexity involved in applying these two methods form another basis for comparison. Since, all of the results were approximations and in close agreement, it is fair to say that both methods produce equally accurate answers in a practical sense. However, the Rayleigh-Ritz method is extremely time intensive to derive and code in *Mathematica*. In addition, the code took about one hour of computer calculation time to produce twelve frequencies. On the other hand, setup of the finite element model in ANSYS took much less time even for a novice user. Also, twelve natural frequencies were calculated in less than one minute. While it is fair to say that both methods have a tremendous learning curve, using finite element software produced equally accurate results with much less complexity, setup time and computation time than the Rayleigh-Ritz method. It is for this reason that many problems in industry are solved primarily with such software.

5.5 Summary:

Chapter 5 used the Rayleigh-Ritz and finite element methods as developed and verified in Chapter 4 to approximate the natural frequencies and mode shapes of a rectangular membrane with a passive PVDF attachment, fixed edges and unequal tensions in the x and y directions. After analyzing the state of stress in the base layer and patch, energy methods and variational calculus were employed in Section 5.2 to develop the partial differential equation of motion for the layered system. The expression for kinetic energy added the mass effects of the patch. However, the stress and deformation analysis used to formulate the potential energy of the system revealed that membrane theory was unable to account for the added stiffness of the PVDF patch. Also in Section 5.2, the Rayleigh-Ritz method was used to express the terms of the mass and stiffness

matrices. With these matrices known, one can readily formulate and solve the traditional eigenvalue problem from Eq. (4.36). Section 5.3 discusses the creation and convergence of ANSYS finite element models that represent the layered system with membrane elements. The numerical comparison between the Rayleigh-Ritz and finite element methods made in Section 5.4 agreed to within one percent. Since membrane elements were used to create the ANSYS model, this high degree of correlation supports the contention that membrane theory can account for the change in mass but not additional stiffness added by the piezoelectric patch. Specifically, membrane theory presumes small deflections such that the tension in a given direction does not change as the system undergoes out-of-plane vibrations. Even with step changes in the base layer stress, the state of stress in the Kapton® membrane is constant with respect to time and displacement. It is in this simplification that the ability to account for the added stiffness of the patch using membrane theory is lost. Despite this deficiency, membrane theory was still able to account for the mass added by the patch and subsequently used to show that the layered system had different natural frequencies than the bare membrane. The mode shapes appeared to be very similar however. A more thorough comparison of these two systems is made in Chapter 7. First, however, Chapter 6 addresses the piezoelectric behavior of the PVDF patch.

Chapter 6

Membrane with Active PVDF Attachment

6.1 Introduction:

Chapter 5 describes the Rayleigh-Ritz and finite element methods that were used to analyze the free vibration characteristics of a system consisting of a rectangular base layer membrane with unequal tensions in the x and y directions and having a passive PVDF attachment. It was rigorously shown that the restrictions of traditional membrane theory render it unable to account for the stiffness of the patch. However, the mass added by the PVDF was represented and shown to alter the natural frequencies by an appreciable amount. While a more detailed numerical comparison is made in Chapter 7 between the bare membrane and the layered system, this chapter focuses on using the piezoelectric properties of the PVDF patch. From Chapter 1, it is known that piezoelectric materials develop a charge proportional to an applied mechanical load and conversely, exhibit a mechanical strain when subjected to an applied electric field. Both of these phenomena will be investigated for the layered system considered in Chapter 5 in terms of the interaction between the active patch and the base layer membrane.

6.2 Piezoelectric Basics:

As is the traditional starting point for most engineering problems, the study of the piezoelectric effect begins with an illustration. Figure 6.1 shows the piezopolymer patch from Figure 5.1 now configured to be used as an active device.

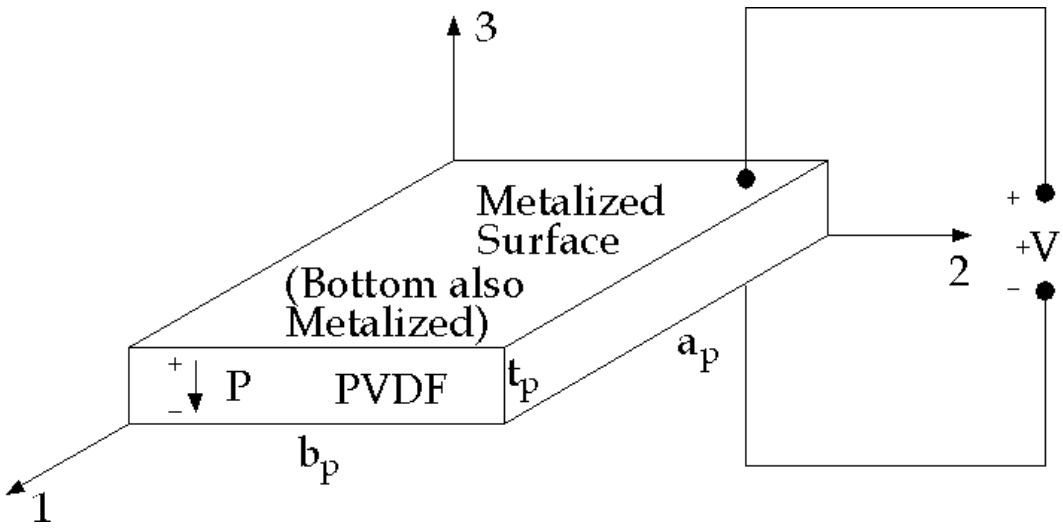

Figure 6.1: Active PVDF Patch and Definition of Material Axes

While PVDF is considered to be a piezoelectric polymer, it is actually a semi-crystalline polymer. Since it is not a perfectly symmetric crystalline material (centrosymmetrical), PVDF lacks a center of symmetry, thus allowing it to exhibit piezoelectric behavior with electrical properties that are direction-dependent, or anisotropic. The key concept to understanding piezoelectric relationships and dealing with this anisotropy is the definition of the coordinate system. For a rectangular patch, a three-dimensional Cartesian coordinate system is typically employed, where 1, 2 and 3 correspond to the global *x, y* and *z* coordinates from Figure 5.1. The polar or 3 axis is always parallel to the polarization direction established in the material during processing. As seen in Figure 6.1, the poling direction points from the positive to negative metalized poling electrode. Despite the fact that piezoelectricity is a well-developed science, there still exists some discrepancy between which direction the positive 3 axis points. For the

purposes of this work, the positive 3 axis is parallel to but opposite the poling direction. As described by Collins [1990], PVDF is drawn (stretched) a great deal during manufacturing prior to the poling procedure to enhance its piezoelectric properties by increasing its molecular orientation. For uniaxial stretching, the degree of electrical anisotropy is increased as the 1 direction is defined as the drawing direction. However, PVDF film can be drawn biaxially, in which case the 1 and 2 directions are interchangeable (for equal amounts of stretching) and a state of in-plane isotropy exists. The effects of drawing on the material behavior will be better understood in terms of the piezoelectric constants discussed shortly. In addition to defining the material directions, one must establish a convention for applied or induced electrical charges. As shown in the figure above, a voltage across the piezoelectric, whether applied or induced, is taken as positive when the positive poling metalized surface corresponds to the positive terminal of the voltage across the material. This positive voltage is defined to cause an increase in thickness and a decrease in width and length. As will be seen shortly, this definition will give the piezoelectric strain constants d_{31} and d_{33} negative and positive values, respectively. Also, an applied voltage is typically expressed as an electric field, which is simply the voltage divided by the thickness over which the voltage is applied. With respect to Figure 6.1, a tensile stress is taken as positive and considered to produce a positive strain (increase in size). Lastly, while PVDF subjected to extreme voltages and loads can exhibit hysteresis, these higher order effects are ignored as the piezopolymer is presumed to behave in a linear fashion for the scope of the present study.

6.2.1 Review of General Elastic Behavior:

In Chapter 5, the mechanical properties of PVDF were presumed to be the same in all directions, or isotropic. However, for the formulation at hand to be applicable to the most general fully anisotropic case, the constitutive relationship between stress and strain (Hooke's Law), is given by

$$\begin{aligned} \sigma_{ij} &= C_{ijkl}\varepsilon_{kl} \quad or \\ \varepsilon_{ij} &= S_{ijkl}\sigma_{kl} \qquad i,j,k,l = 1,2,3 \end{aligned} \tag{6.1}$$

where C_{ijkl} is the material stiffness tensor and S_{ijkl} is the material compliance tensor. Despite this complicated indicial notation, equilibrium conditions and planes of isotropy will be used to reduce the degree of anisotropy. Since stress and strain are both second order tensors, they are related by fourth order tensors such, i.e., stiffness or compliance. Using this many subscripts is oftentimes cumbersome; the stiffness and compliance tensors have 81 (3^4) components each. Therefore, I.E.E.E. contracted notation is often employed, reducing the number of indices on the stiffness and compliance tensors to two, while increasing their range from three to nine. In contracted notation, the generalize form of Hooke's Law is

$$\begin{aligned} \sigma_i &= C_{ij}\varepsilon_j \quad or \\ \varepsilon_i &= S_{ij}\sigma_j \qquad i,j = 1,2...9 \end{aligned} \tag{6.2}$$

The relationship between stresses and strains in tensor and contracted notation is shown in Table 6.1.

Table 6.1: Tensor versus Contracted Notation for Stresses and Strains

Stresses		Strains	
Tensor Notation	Contracted Notation	Tensor Notation	Contracted Notation
σ_{11}	σ_1	ε_{11}	ε_1
σ_{22}	σ_2	ε_{22}	ε_2
σ_{33}	σ_3	ε_{33}	ε_3
$\sigma_{23}=\tau_{23}$	σ_4	$2\varepsilon_{23}=\gamma_{23}$	ε_4
$\sigma_{31}=\tau_{31}$	σ_5	$2\varepsilon_{31}=\gamma_{31}$	ε_5
$\sigma_{12}=\tau_{12}$	σ_6	$2\varepsilon_{12}=\gamma_{12}$	ε_6
$\sigma_{32}=\tau_{32}$	σ_7	$2\varepsilon_{32}=\gamma_{32}$	ε_7
$\sigma_{13}=\tau_{13}$	σ_8	$2\varepsilon_{13}=\gamma_{13}$	ε_8
$\sigma_{21}=\tau_{21}$	σ_9	$2\varepsilon_{21}=\gamma_{21}$	ε_9

This contracted notations does come at a small price. The number of indices is no longer indicative of the order of the tensor. Also, the range of the indices no

longer represents the number of spatial dimensions. Additionally, there are still 81 (9^2) components of both the stiffness and compliance tensors. However, in this form, it is easier to visualize using matrix notation and operations as well as straightforward to apply some basic symmetry conditions to reduce the range of the two indices. First, in the absence of body couples, the stress and strain tensors are symmetric such that

$$\begin{aligned} \sigma_{ij} &= \sigma_{ji} \\ \varepsilon_{ij} &= \varepsilon_{ji} \qquad i, j = 1,2,3 \end{aligned} \tag{6.3}$$

From this simplification, the contracted notation shown in Table 6.1 reduces further as shown in Table 6.2.

Table 6.2: Contracted Stresses and Strains After Reduction from Symmetry

Stresses		Strains	
Tensor Notation	Contracted Notation	Tensor Notation	Contracted Notation
σ_{11}	σ_1	ε_{11}	ε_1
σ_{22}	σ_2	ε_{22}	ε_2
σ_{33}	σ_3	ε_{33}	ε_3
$\sigma_{23}=\sigma_{32}$	σ_4	$2\varepsilon_{23}=2\varepsilon_{32}=\gamma_{23}=\gamma_{32}$	ε_4
$\sigma_{31}=\sigma_{13}$	σ_5	$2\varepsilon_{31}=2\varepsilon_{13}=\gamma_{31}=\gamma_{13}$	ε_5
$\sigma_{12}=\sigma_{21}$	σ_6	$2\varepsilon_{12}=2\varepsilon_{21}=\gamma_{12}=\gamma_{21}$	ε_6

With the range of the two indices now reduced to six, Hooke's Law can now be expressed as

$$\begin{aligned} \sigma_i &= C_{ij}\varepsilon_j \quad or \\ \varepsilon_i &= S_{ij}\sigma_j \qquad i, j = 1,2...6 \end{aligned} \tag{6.4}$$

It is important to note from Table 6.2 that ε_4, ε_5 and ε_6 as used in Eq. (6.4) are defined as the engineering shear strains, γ_{23}, γ_{31}, and γ_{12}, respectively, which are equal to twice the corresponding tensor shear strain. This factor of two will appear again when the compliance matrix is examined more closely. Since the number of independent stress and strain terms has been reduced, the number of independent stiffness and compliance terms required has also been reduced as

seen in Eq. (6.4), from 81 each to only 36 each (six by six matrices) for three-dimensional objects. According to Jones [1999], an excellent reference to which the reader is directed for a more formal treatment of tensors, the stiffness and compliance matrices are symmetric, further reducing the number of independent elastic constants to 21. Eq. (6.4) gives the stress-strain and strain-stress relationships for anisotropic materials, the most general case of linear elastic behavior. The exact expressions for the various compliance or stiffness terms will be presented as needed for the electromechanical coupling of the PVDF patch.

6.2.2 Piezoelectric Constitutive Relationships:

With the elastic behavior now thoroughly understood and quantified, the coupled electrical and mechanical responses are investigated. However, the science of piezoelectricity uses a different notation, specified by I.E.E.E., than that of traditional mechanics. Thus, from this point forward, the notation applicable to piezoelectric materials will be employed and deviation from the notation of mechanics clearly noted.

The charge produced in a piezoelectric device is a function of the applied mechanical stress and electric field and is given as

$$D_i = d_{ijk} T_{jk} + \varepsilon_{ij}^T E_j \qquad i, j, k = 1,2,3 \tag{6.5}$$

where D is the electric displacement (charge per unit area), d is the piezoelectric strain constant, T is the stress tensor (instead of σ from classical mechanics), ε^T is the permitivity of the material measured at constant stress (mechanically free, as denoted by superscript T), and E is the electric field across the material. The mechanical strain is a function of applied mechanical stress and electric field, such that

$$S_{ij} = s_{ijkl}^E T_{kl} + d_{kij} E_k \qquad i, j, k, l = 1,2,3 \tag{6.6}$$

where S is the mechanical strain and s^E is the elastic compliance measured at constant electric field (short circuit). Eq. (6.5) and Eq. (6.6) are written in tensor notation; however, planes of isotropy and some elements of crystal symmetry within the PVDF material will be used to reduce these equations to a more applicable and manageable matrix form.

First Eq. (6.5) is examined for potential simplifications. The electric displacement D is a vector whose length is three, corresponding to the 1, 2 and 3 directions on which charge could be developed if electrodes are present. The piezoelectric strain constant d is a third order tensor with 27 (3^3), all of which are not independent. Equilibrium requires that

$$d_{ijk} = d_{ikj} \qquad i, j, k = 1,2,3 \tag{6.7}$$

so that only 18 independent constants remain in a three by six matrix:

$$d = \begin{pmatrix} d_{11} & d_{12} & d_{13} & d_{14} & d_{15} & d_{16} \\ d_{21} & d_{22} & d_{23} & d_{24} & d_{25} & d_{26} \\ d_{31} & d_{32} & d_{33} & d_{34} & d_{35} & d_{36} \end{pmatrix} \tag{6.8}$$

However, crystal symmetry for various materials reduces many of these 18 terms to zero. The crystalline portions of PVDF, have an orthorhombic crystal structure and point group mm2, the d tensor is simplified to the following matrix:

$$d = \begin{pmatrix} 0 & 0 & 0 & 0 & d_{15} & 0 \\ 0 & 0 & 0 & d_{24} & 0 & 0 \\ d_{31} & d_{32} & d_{33} & 0 & 0 & 0 \end{pmatrix} \tag{6.9}$$

Eq. (6.9) is valid for film that is uniaxially stretched prior to poling. If it is drawn equal amounts in a biaxial manner, the 1 and 2 directions are interchangeable, thus making the piezoelectric strain constants isotropic in the 1-2 plane and simplifying Eq. (6.9) to

$$d = \begin{pmatrix} 0 & 0 & 0 & 0 & d_{15} & 0 \\ 0 & 0 & 0 & d_{15} & 0 & 0 \\ d_{31} & d_{31} & d_{33} & 0 & 0 & 0 \end{pmatrix} \tag{6.10}$$

From Section 6.2.1, the stress tensor reduces to

$$T = \begin{pmatrix} \sigma_1 & \sigma_2 & \sigma_3 & \sigma_4 & \sigma_5 & \sigma_6 \end{pmatrix}^T \tag{6.11}$$

where the superscript T denotes the transpose of the stress matrix. The permitivity of the material is given as a nine-component tensor; however, PVDF develops a charge only in the direction across which a field is applied, making the permitivity tensor a diagonal matrix, as seen in Eq. (6.12):

$$\varepsilon^T = \begin{pmatrix} \varepsilon_{11} & 0 & 0 \\ 0 & \varepsilon_{11} & 0 \\ 0 & 0 & \varepsilon_{33} \end{pmatrix} \tag{6.12}$$

where the superscript T denotes a value measured at constant stress (mechanically free). The electric field E is also a vector of length three, again corresponding to the 1, 2 and 3 directions on which an electric field can be applied if electrodes are present. Combining Eq. (6.10), Eq. (6.11), Eq. (6.12) and the described nature of D and E per Eq. (6.5) yields the sensor form of the constitutive relationship for PVDF with isotropic d and ε values in the 1-2 plane:

$$\begin{pmatrix} D_1 \\ D_2 \\ D_3 \end{pmatrix} = \begin{pmatrix} 0 & 0 & 0 & 0 & d_{15} & 0 \\ 0 & 0 & 0 & d_{15} & 0 & 0 \\ d_{31} & d_{31} & d_{33} & 0 & 0 & 0 \end{pmatrix} \begin{pmatrix} \sigma_1 \\ \sigma_2 \\ \sigma_3 \\ \sigma_4 \\ \sigma_5 \\ \sigma_6 \end{pmatrix} + \begin{pmatrix} \varepsilon_{11} & 0 & 0 \\ 0 & \varepsilon_{11} & 0 \\ 0 & 0 & \varepsilon_{33} \end{pmatrix} \begin{pmatrix} E_1 \\ E_2 \\ E_3 \end{pmatrix} \tag{6.13}$$

Next, Eq. (6.6) is inspected closely, where the compliance tensor, s_{ijkl} is known to reduce to a six by six symmetric matrix having 21 independent elastic constants for a fully anisotropic material. However, it is reasonable to consider the mechanical properties of PVDF to be isotropic, in which case the compliance matrix has only two independent constants and is shown to be

$$s = \begin{pmatrix} s_{11} & s_{12} & s_{12} & 0 & 0 & 0 \\ s_{12} & s_{11} & s_{12} & 0 & 0 & 0 \\ s_{12} & s_{12} & s_{11} & 0 & 0 & 0 \\ 0 & 0 & 0 & 2(s_{11}-s_{12}) & 0 & 0 \\ 0 & 0 & 0 & 0 & 2(s_{11}-s_{12}) & 0 \\ 0 & 0 & 0 & 0 & 0 & 2(s_{11}-s_{12}) \end{pmatrix} \tag{6.14}$$

Of course, this matrix is defined as such for relating normal and engineering shear strains to normal and shear stresses, hence the factor of two appearing on the shear terms along the diagonal. This factor is consistent with contracted notation as defined in Table 6.2 and is in agreement with the discussion following Eq. (6.4). It should be noted that in Eq. (6.6), the required compliance is that which has been measured under short-circuit conditions. If the compliance is written in terms of engineering constants such as the elastic (Young's) and shear moduli and Poisson's ratio, then numerical values measured under short-circuit conditions can be used in a straightforward manner. Such numerical material properties are readily available for most piezoelectric materials in handbooks or literature supplied by manufacturers. From Jones [1999], the compliance matrix for a mechanically isotropic material is given in terms of engineering constants as

$$s = \begin{pmatrix} \frac{1}{Y} & -\frac{\nu}{Y} & -\frac{\nu}{Y} & 0 & 0 & 0 \\ -\frac{\nu}{Y} & \frac{1}{Y} & -\frac{\nu}{Y} & 0 & 0 & 0 \\ -\frac{\nu}{Y} & -\frac{\nu}{Y} & \frac{1}{Y} & 0 & 0 & 0 \\ 0 & 0 & 0 & \frac{1}{G} & 0 & 0 \\ 0 & 0 & 0 & 0 & \frac{1}{G} & 0 \\ 0 & 0 & 0 & 0 & 0 & \frac{1}{G} \end{pmatrix} \tag{6.15}$$

where the elastic modulus is now represented as Y (instead of E in classical mechanics), ν is Poisson's ratio and G is the shear modulus of the PVDF. Even

though there are three constants in Eq. (6.15), only two are independent, and according to the shear compliance terms in Eq. (6.14), G can be expressed as

$$G = \frac{Y}{2(1+\nu)} \tag{6.16}$$

The next term in Eq. (6.6) is the same vector of stress given by Eq. (6.11). While the d tensor in Eq. (6.5) was shown to reduce to the form of Eq. (6.10) for biaxially drawn PVDF, when the symmetric nature of Eq. (6.7) is applied to the d tensor in Eq. (6.6), a six by three matrix results, which is equal to the transpose of the d matrix in Eq. (6.8). After applying the crystal symmetry of PVDF to d^T (where the superscript T refers to the transpose of the matrix), the d tensor from Eq. (6.6) becomes

$$d^T = \begin{pmatrix} 0 & 0 & d_{31} \\ 0 & 0 & d_{31} \\ 0 & 0 & d_{33} \\ 0 & d_{15} & 0 \\ d_{15} & 0 & 0 \\ 0 & 0 & 0 \end{pmatrix} \tag{6.17}$$

This meets the requirements of matrix multiplication, as the electric field tensor E is again a vector of length three. With all of the terms simplified as much as possible for the given material, Eq. (6.6) becomes

$$\begin{pmatrix} S_1 \\ S_2 \\ S_3 \\ S_4 \\ S_5 \\ S_6 \end{pmatrix} = \begin{pmatrix} \frac{1}{Y} & -\frac{\nu}{Y} & -\frac{\nu}{Y} & 0 & 0 & 0 \\ -\frac{\nu}{Y} & \frac{1}{Y} & -\frac{\nu}{Y} & 0 & 0 & 0 \\ -\frac{\nu}{Y} & -\frac{\nu}{Y} & \frac{1}{Y} & 0 & 0 & 0 \\ 0 & 0 & 0 & \frac{1}{G} & 0 & 0 \\ 0 & 0 & 0 & 0 & \frac{1}{G} & 0 \\ 0 & 0 & 0 & 0 & 0 & \frac{1}{G} \end{pmatrix} \begin{pmatrix} \sigma_1 \\ \sigma_2 \\ \sigma_3 \\ \sigma_4 \\ \sigma_5 \\ \sigma_6 \end{pmatrix} + \begin{pmatrix} 0 & 0 & d_{31} \\ 0 & 0 & d_{31} \\ 0 & 0 & d_{33} \\ 0 & d_{15} & 0 \\ d_{15} & 0 & 0 \\ 0 & 0 & 0 \end{pmatrix} \begin{pmatrix} E_1 \\ E_2 \\ E_3 \end{pmatrix} \tag{6.18}$$

The electromechanical behavior of PVDF having isotropic mechanical properties and permitivity and isotropic electrical properties in the 1-2 plane is fully

described by Eq. (6.13) and Eq. (6.18). While this is the most popular and applicable form of the constitutive relationship for piezoelectric devices, other forms can be found in terms of different piezoelectric constants such as *g*, *h* or *e*. The reader is referred to Ikeda [1996] for such forms and relationships between constants. From the constitutive relationships formulated above, the piezoelectric strain constant d_{ij} couples the electrical and mechanical responses of the PVDF. The double subscripts correspond to the material coordinate system (1, 2 or 3) of Figure 6.1. The first subscript indicates to which axis the electrode is perpendicular. Thus, a 3 as the first subscript means that a metalized surface for either collecting or depositing charge is perpendicular to the 3 axis, as illustrated in Figure 6.1. The second subscript denotes the direction of applied mechanical stress or induced mechanical strain.

6.3 Application to Membrane with PVDF Patch:

Piezoelectric devices are often attached to an elastic structure for use as either a sensor or an actuator, and with special electrical circuitry, both simultaneously [Dosch, Inman and Garcia 1992]. For the current research effort, the capacity of the PVDF patch to act as either a sensor or an actuator when attached to a base layer membrane is investigated. The type of PVDF under consideration is that described by the constitutive relationships of Eq. (6.13) and Eq. (6.18) that is, having isotropic mechanical properties and permitivity and isotropic electrical properties in the 1-2 plane ($d_{32}=d_{31}$). Before applying these coupled electromechanical equations directly, they can be simplified further by realizing that PVDF is typically used as a thin film on the order of one-thousandth of an inch thick. Therefore, forming electrodes by metalizing the sides corresponding to the 1 and 2 directions is not feasible, so the only direction of applied electric field or developed electrical displacement is 3 as shown in Figure 6.1. This geometric limitation renders E_1 and E_2 zero. Furthermore, the stress analysis of the layered system seen in Figure 5.1 showed that a state of plane stress exists in

the patch, consisting of normal stress in the 1 and 2 directions resulting from the internal pressure of the torus from Chapter 2. Thus, σ_3, σ_4, σ_5 and σ_6 are all zero. With this simplified loading scenario and the presence of only one electrode as described above, Eq. (6.13) and Eq. (6.18) reduce to

$$D_3 = d_{31}(\sigma_1 + \sigma_2) + \varepsilon_{33} E_3 \tag{6.19}$$

$$S_1 = \frac{1}{Y}(\sigma_1 - \nu\sigma_2) + d_{31} E_3 \tag{6.20}$$

$$S_2 = \frac{1}{Y}(\sigma_2 - \nu\sigma_1) + d_{31} E_3 \tag{6.21}$$

$$S_3 = -\frac{\nu}{Y}(\sigma_1 + \sigma_2) + d_{33} E_3 \tag{6.22}$$

By simplifying the cumbersome constitutive relationship of Eq. (6.5) and Eq. (6.6) to the PVDF patch and application of interest to the current work, a much more manageable form has been found. Next, the ability, if any, of the PVDF patch to act as a sensor for measuring out-of-plane vibrations of the layered membrane system seen in Figure 5.1 will be assessed. Then, the ability of the patch to actuate the base layer membrane will be investigated.

6.3.1 Sensor Application of PVDF on Membrane:

To predict how the PVDF patch attached to the base layer membrane can be utilized in a sensor capacity, Eq. (6.19) is evoked. From the stress analysis of Section 5.2.2, the initial stresses applied to the patch in the 1 and 2 directions are known to be σ_x^P and σ_y^P as calculated in Eq. (5.11) and Eq. (5.12). In terms of Eq. (6.19), these stresses correspond to σ_1 and σ_2. Also, when used as a sensor, no electric field is applied; E_3 is also zero. Thus, the electric displacement resulting from the prestress in the patch due to internal pressure of the torus is simply

$$D_3 = d_{31}(\sigma_1 + \sigma_2) \tag{6.23}$$

The electrical displacement is defined as the charge developed per unit area of patch, but the voltage that this produces is a more useful output from a sensor. In general, the charge developed on an electrode, q, is written as

$$q = \int_A \boldsymbol{D} \cdot \mathbf{n}\, dA \tag{6.24}$$

where $\boldsymbol{D}$ is the vector of electrical displacements, $\mathbf{n}$ is the normal vector to the electrode on which the charge is desired and A is the surface area of the electrode (patch). However, $\boldsymbol{D}$ contains only D_3 from Eq. (6.23) and the normal vector is the 3-axis, thus the dot product required by Eq. (6.24) is one ($k \cdot k = 1$) and with Eq. (6.23), the charge is simply

$$q = \int_{y_1}^{y_2} \int_{x_1}^{x_2} d_{31}(\sigma_1 + \sigma_2)\, dxdy \tag{6.25}$$

However, membrane theory presumes that only small deflections occur such that the tension remains constant with respect to time. If this presumption is correct, then σ_1 and σ_2 in the patch are also constant with respect to x and y and can be removed from the integrand of Eq. (6.25). The remaining integral is simply the area of the patch, given as a_P times b_P from Figure 5.1. Thus, the charge is simply D_3 times the patch area, or

$$q = d_{31}(\sigma_1 + \sigma_2)\, a_P b_P \tag{6.26}$$

From elementary physics, the voltage across a capacitor is given as the charge divided by its capacitance. Piezoelectric materials act as capacitors as they have the ability to store charge, thus the voltage output from the PVDF sensor V is given as

$$V = \frac{d_{31}(\sigma_1 + \sigma_2)\, a_P b_P}{C_P} \tag{6.27}$$

where C_P is the capacitance of the PVDF material. Clearly, this voltage is going to be constant throughout any transverse deflections under the small deflection-constant tension restriction of membrane theory. As a result, membrane theory does not offer the ability to use a PVDF patch as a sensor for vibrations

transverse to the plane of equilibrium. For the above analysis to be applicable, the stress must be allowed to vary as a function of the out-of-plane displacement. Of course, this involves additional complications beyond the scope of membrane vibrations being covered in this work. While there is some charge developed for the static loading described above, piezoelectric devices make poor static measurement devices because they lose their accumulated charge rapidly. The slowest frequencies that piezoelectrics should be used to sense are on the order of 0.001 Hz.

6.3.2 Distributed Piezoelectric Actuators:

When a piezoelectric patch is bonded to a plate or beam and employed as an actuator, the strain developed in the active material is generally modeled as a force applied at a finite distance from the neutral axis of the structure. This force causes a bending moment to be applied to the host structure and deflection to occur as shown in Figure 6.2.

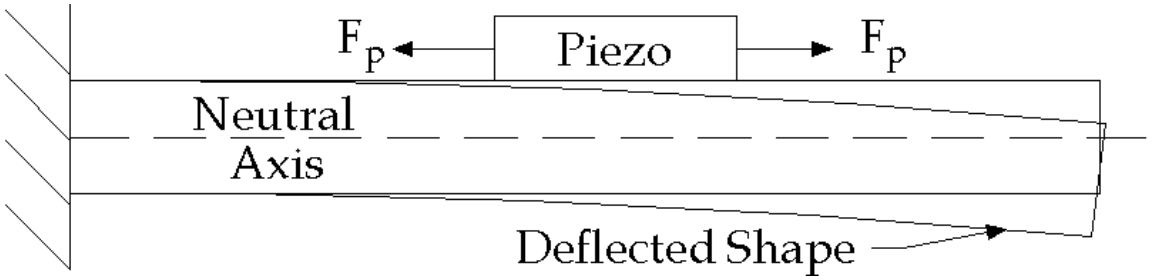

Figure 6.2: Piezoelectric Bending Actuator on a Beam

6.3.2.1 Actuator-Structure Interaction:

Since membranes have negligible bending stiffness, such application of a bending moment is not possible. However, when an electric field is applied across the PVDF patch in Figure 5.1, the resulting deformation of the PVDF patch can be modeled as an in-plane force applied to the membrane. In this case, the piezopolymer is able to actuate the structure by altering the tension in the membrane as a function of the applied electric field. Modeling the effects of the

piezoelectric patch on the host structure is oftentimes difficult. Many methods exist for representing such interactions, particularly for beams and plates with distributed actuators. Strain energy methods are often used and were considered for the current effort but became quite cumbersome for the initial state of biaxial tension present in the layered membrane system. The enhanced pin-force method is popular for modeling patch-structure interactions, but not applicable to membranes as this it considers applied bending moments. Perhaps the simplest model of such active structure relationships is the pin-force method, which considers the induced strain in the piezoelectric to cause only a force parallel to the plane of the structure. In his Master's thesis, Lummer [1998] provides a detailed derivation of these and other methods for bending actuators. Since the pin-force method ignores the bending stiffness of the actuator, there exist some limitations resulting in only rough behavior approximations for many cases. Furthermore, Lummer [1998] notes that severe inaccuracies arise when the patch is more than five times as stiff as the substrate, but the pin-force method is reasonably accurate when the base layer is much stiffer than the actuator. Nevertheless, the PVDF patch and Kapton® base layer are treated as membranes, which have negligible bending stiffness. With mismatches in structural stiffness no longer a concern, modeling the interaction between the base layer membrane and the perfectly bonded PVDF patch in a manner analogous to the pin-force method is expected to produce reasonable results.

6.3.2.2 PVDF Actuator Attached to Membrane:

The ability to predict the tension in the x and y directions of the base layer as a function of the voltage applied to the patch is the goal of this section. Since the patch is assumed to be bonded to the satellite prior to inflation during orbit, the patch is exposed to an initial state of plane stress as calculated in Eq. (5.11) and Eq. (5.12), where the x and y directions have been changed to 1 and 2, respectively, to correspond to the coordinate system for the PVDF patch defined

in Figure 6.1. In order to be utilized as an actuator, an electric field will be applied across the thickness of the patch. The interaction between these mechanical and electrical loads is taken from the constitutive relationships of Eq. (6.20) and Eq. (6.21):

$$S_1^P = \frac{1}{E_P}\left(\sigma_1^{P(i)} - \nu_P \sigma_2^{P(i)}\right) + \frac{d_{31}V}{t_P} \tag{6.28}$$

$$S_2^P = \frac{1}{E_P}\left(\sigma_2^{P(i)} - \nu_P \sigma_1^{P(i)}\right) + \frac{d_{31}V}{t_P} \tag{6.29}$$

where P and (i) denote the patch layer and initial stresses in the patch. Since there is no stress applied transverse to the patch (3 direction), Eq. (6.22) is disregarded as it only reveals strain due to Poisson contraction and does not offer any new information about the in-plane stresses. As for the base layer directly under the PVDF patch, Hooke's Law gives the x and y strains as

$$S_x^b = \frac{1}{E_b}\left(\sigma_x^b - \nu_b \sigma_y^b\right) \tag{6.30}$$

$$S_y^b = \frac{1}{E_b}\left(\sigma_y^b - \nu_b \sigma_x^b\right) \tag{6.31}$$

where b refers to the base layer. From the stress analysis of Section 5.2.2, the strains in the two layers must be equal to ensure perfect bonding. This deformation compatibility requires that

$$S_1^P = S_x^b \tag{6.32}$$

$$S_2^P = S_y^b \tag{6.33}$$

Substituting Eq. (6.28) through Eq. (6.31) into the proper locations in Eq. (6.32) and Eq. (6.33) yields two equations in two unknowns, σ_x^b and σ_y^b. Solving simultaneously yields the following base layer stresses:

$$\sigma_x^b = \frac{E_b}{E_P\left(\nu_b^2 - 1\right)}\left(\sigma_1^{P(i)}\left(\nu_P\nu_b - 1\right) + \sigma_2^{P(i)}\left(\nu_P - \nu_b\right)\right) + \frac{E_b d_{31} V}{t_P\left(1-\nu_b\right)} \tag{6.34}$$

$$\sigma_y^b = \frac{E_b}{E_P\left(\nu_b^2 - 1\right)}\left(\sigma_1^{P(i)}\left(\nu_P - \nu_b\right) + \sigma_2^{P(i)}\left(\nu_P\nu_b - 1\right)\right) + \frac{E_b d_{31} V}{t_P\left(1-\nu_b\right)} \tag{6.35}$$

A quick numerical substitution or lengthy algebraic manipulation shows that these equations are simply

$$\sigma_x^b = \sigma_x^{b(i)} + \frac{E_b d_{31} V}{t_P (1-\nu_b)} \tag{6.36}$$

$$\sigma_y^b = \sigma_y^{b(i)} + \frac{E_b d_{31} V}{t_P (1-\nu_b)} \tag{6.37}$$

Since the strains in the patch change as a function of voltage, the corresponding stresses in the patch are found using Hooke's Law with Eq. (6.28) and Eq. (6.29) to be

$$\sigma_1^P = \sigma_1^{P(i)} + \frac{E_P d_{31} V}{t_P (1-\nu_p)} \tag{6.38}$$

$$\sigma_2^P = \sigma_2^{P(i)} + \frac{E_P d_{31} V}{t_P (1-\nu_p)} \tag{6.39}$$

With the stress in the patch and base layer under the patch known as a function of the applied voltage, the next step is to assess how changing the voltage effects the tension in the base layer membrane away from the patch. The membrane under consideration in the current work has fixed edges. From the stress analysis of Section 5.2.2, there exists equal initial strain in the patch and base layer under the patch due to the internal pressure of the torus. Applying a voltage across the thickness of the patch will cause the strain in the patch and the base layer under the patch to change by an equal amount prescribed by the constitutive relationship in either Eq. (6.20) and Eq. (6.21) or Eq. (6.30) and Eq. (6.31). For instance, according to the sign convention adopted for the current work, application of a negative voltage to the patch will cause a positive change in the 1 and 2 direction dimensions as shown generally in Figure 6.3.

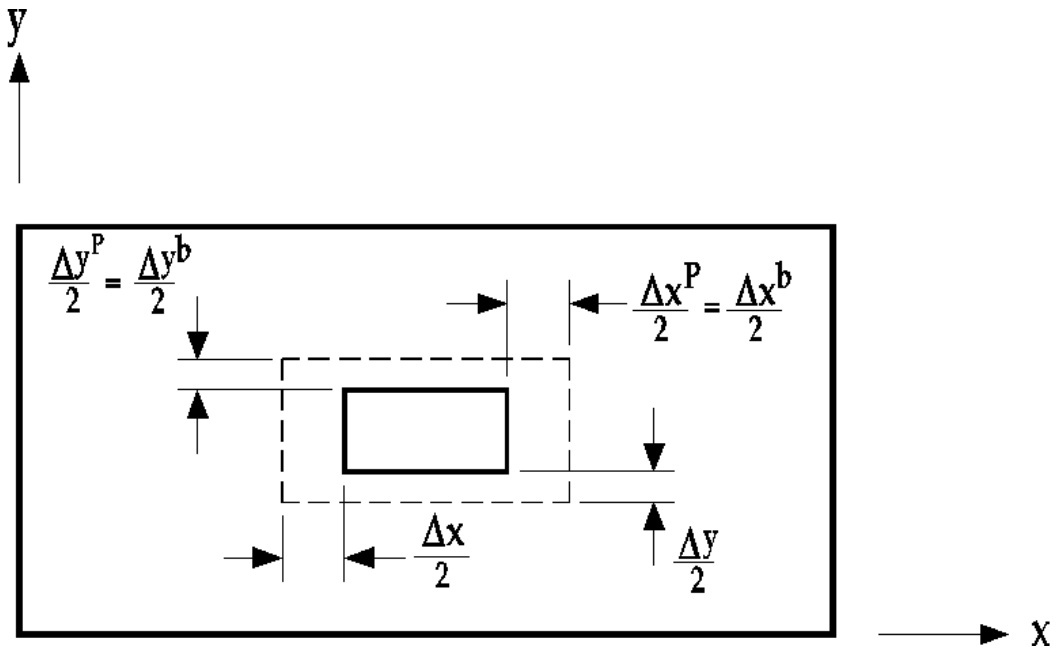

Figure 6.3: Deflections due to PVDF Actuation

Since the base layer must remain a continuous system, the material away from the patch must undergo a deflection equal in magnitude but opposite in sign to that of the patch and base layer under the patch. Thus

$$\Delta x^P = \Delta x^b = -\Delta x \tag{6.40}$$

$$\Delta y^P = \Delta y^b = -\Delta y \tag{6.41}$$

where Δx and Δy with superscripts P and b indicate a change in dimension of the patch and base layer under the patch, respectively, and the lack of a superscript on Δx and Δy refers to the change in size experienced by the base layer away from the patch. Since the constitutive relationships are in terms of stress and strain, the change in strain of the patch in the 1 direction under an applied voltage is

$$\Delta S_1^P = \frac{1}{E_P}\left(\left(\sigma_1^P - \nu_P \sigma_2^P\right) - \left(\sigma_1^{P(i)} - \nu_P \sigma_2^{P(i)}\right)\right) \tag{6.42}$$

while the change in strain of the patch in the 2 direction is given by

$$\Delta S_2^P = \frac{1}{E_P}\left(\left(\sigma_2^P - \nu_P \sigma_1^P\right) - \left(\sigma_2^{P(i)} - \nu_P \sigma_1^{P(i)}\right)\right) \tag{6.43}$$

The change in strain of the base layer under the patch in the x direction due to a voltage applied to the patch is

$$\Delta S_x^b = \frac{1}{E_b}\left(\left(\sigma_x^b - \nu_b \sigma_y^b\right) - \left(\sigma_x^{b(i)} - \nu_b \sigma_y^{b(i)}\right)\right) \tag{6.44}$$

while the change in strain of the base layer under the patch in the y direction is given by

$$\Delta S_y^b = \frac{1}{E_b}\left(\left(\sigma_y^b - \nu_b \sigma_x^b\right) - \left(\sigma_y^{b(i)} - \nu_b \sigma_x^{b(i)}\right)\right) \tag{6.45}$$

Of course, the strains in the patch and the base layer under the patch in the x and y directions must be equal lest the layers would break apart. However, these four changes in strain can be written as

$$\Delta S_1^P = \frac{\Delta x^P}{a_P} \quad \Delta S_2^P = \frac{\Delta y^P}{b_P} \quad \Delta S_x^b = \frac{\Delta x^b}{a_p} \quad \Delta S_y^b = \frac{\Delta y^b}{b_p} \tag{6.46}$$

According to Eq. (6.40) and Eq. (6.41), the deflections in the base layer away from the patch must be equal to but opposite in sign to the deflections of the patch and the base layer under the patch. The changes in strain of the base layer away from the patch are given by

$$\Delta S_x = \frac{\Delta x}{a - a_P} \quad \Delta S_y = \frac{\Delta y}{b - b_P} \tag{6.47}$$

and also from the constitutive relationship as

$$\Delta S_y = \frac{1}{E_b}\left(\left(\sigma_y - \nu_b \sigma_x\right) - \left(\sigma_y^{(i)} - \nu_b \sigma_x^{(i)}\right)\right) \tag{6.48}$$

$$\Delta S_y = \frac{1}{E_b}\left(\left(\sigma_y - \nu_b \sigma_x\right) - \left(\sigma_y^{(i)} - \nu_b \sigma_x^{(i)}\right)\right) \tag{6.49}$$

Solving for the deflections in the base layer under and away from the patch and substituting into Eq. (6.40) and Eq. (6.41) yields

$$a_P\left(\left(\sigma_x^b - \nu_b \sigma_y^b\right) - \left(\sigma_x^{b(i)} - \nu_b \sigma_y^{b(i)}\right)\right) = -\left(a - a_p\right)\left(\left(\sigma_x - \nu_b \sigma_y\right) - \left(\sigma_x^{(i)} - \nu_b \sigma_y^{(i)}\right)\right) \tag{6.50}$$

$$b_P\left(\left(\sigma_y^b - \nu_b \sigma_x^b\right) - \left(\sigma_y^{b(i)} - \nu_b \sigma_x^{b(i)}\right)\right) = -\left(b - b_p\right)\left(\left(\sigma_y - \nu_b \sigma_x\right) - \left(\sigma_y^{(i)} - \nu_b \sigma_x^{(i)}\right)\right) \tag{6.51}$$

This leaves two equations in two unknowns, σ_x and σ_y. Solving simultaneously for these unknowns yields

$$\sigma_x = \frac{a\,b_P\left(\left(\sigma_x^b - \nu_b\sigma_y^b\right) - \left(\sigma_x^{b(i)} - \nu_b\sigma_y^{b(i)}\right)\right) + a_P\left(b\,\nu_b\left(\left(\sigma_y^b - \nu_b\sigma_x^b\right) - \left(\sigma_y^{b(i)} - \nu_b\sigma_x^{b(i)}\right)\right) + b_P\left(\sigma_x^b + \sigma_x^{(i)} - \sigma_x^{b(i)}\right)\left(\nu_b^2 - 1\right)\right)}{a_P\,b_P\left(\nu_b^2 - 1\right)} \tag{6.52}$$

$$\sigma_y = \frac{a\,b_P\,\nu_b\left(\left(\sigma_x^b - \nu_b\sigma_y^b\right) - \left(\sigma_x^{b(i)} - \nu_b\sigma_y^{b(i)}\right)\right) + a_P\left(b\left(\left(\sigma_y^b - \nu_b\sigma_x^b\right) - \left(\sigma_y^{b(i)} - \nu_b\sigma_x^{b(i)}\right)\right) + b_P\left(\sigma_y^b + \sigma_y^{(i)} - \sigma_y^{b(i)}\right)\left(\nu_b^2 - 1\right)\right)}{a_P\,b_P\left(\nu_b^2 - 1\right)} \tag{6.53}$$

where the dimensions *a, b, a_P* and *b_P* are defined in Figure 5.1 and $\sigma_x^{(i)}$, $\sigma_y^{(i)}$ $\sigma_x^{b(i)}$, $\sigma_y^{b(i)}$, σ_x^b and σ_y^b are given by Eq. (2.8), Eq. (2.9), Eq. (5.9), Eq. (5.10), Eq. (6.36) and Eq. (6.37), respectively. However, application of σ_x^b and σ_y^b from Eq. (6.36) and Eq. (6.37) simplify the long expressions for base layer stress away from the patch considerably. After algebraic simplification the stresses become:

$$\sigma_x = \frac{a\,b_P\,d_{31}E_b\,V - a_P\left(b_P\left(\nu_b + 1\right)\left(d_{31}E_bV + t_P\sigma_x^{(i)}\left(1 - \nu_b\right)\right) - b\,d_{31}E_bV\nu_b\right)}{a_P b_P t_P\left(\nu_b^2 - 1\right)} \tag{6.54}$$

$$\sigma_y = \frac{a\,b_P\,d_{31}E_b\,V\nu_b - a_P\left(b_P\left(\nu_b + 1\right)\left(d_{31}E_bV + t_P\sigma_y^{(i)}\left(1 - \nu_b\right)\right) - b\,d_{31}E_bV\right)}{a_P b_P t_P\left(\nu_b^2 - 1\right)} \tag{6.55}$$

After further simplification and multiplication by the base layer thickness to convert to tension quantities,

$$P_x = \sigma_x^{(i)}t_b + \frac{t_b d_{31}E_bV}{t_P\left(\nu_b^2 - 1\right)}\left(\frac{a}{a_P} + \frac{\nu_b\,b}{b_P} - \left(\nu_b + 1\right)\right) \tag{6.56}$$

$$P_y = \sigma_y^{(i)}t_b + \frac{t_b d_{31}E_bV}{t_P\left(\nu_b^2 - 1\right)}\left(\frac{\nu_b\,a}{a_P} + \frac{b}{b_P} - \left(\nu_b + 1\right)\right) \tag{6.57}$$

At this point, it should be noted that the changes in deformations in the base layer away from the patch could have been equated, per Eq. (6.40) and Eq. (6.41), to the changes in dimension of the patch, obtained from the strain changes in Eq. (6.42) and Eq. (6.43). This form of the tensions in the base layer away from the

patch is fairly simple, yet required a great deal of analysis to derive. It is easy to reason that the voltage dependent tensions are essentially the sum of the initial tension and the change in tension due to actuating the PVDF patch, where the size of the base layer and patch and Poisson effects are considered.

6.3.2.3 Numerical Assessment and Voltage Limitations:

To assess the validity and limitations of Eq. (6.56) and Eq. (6.57), a numerical example is considered. The same coupon from the torus analyzed in Section 4.3 is considered again, with geometric properties of interest found in Table 4.1. The material properties of Kapton® and PVDF are again taken from Table 4.3 and Table 5.1, respectively, and the thickness of the actuator patch is again taken to be 0.0005 inches. Typical values for the electrical properties of PVDF are given in Table 6.3. While the yield strength is not an electrical property, it will be used shortly as a limiting factor for the maximum allowable voltage.

Table 6.3: Typical Electrical Properties for 0.5 mil Thick PVDF Film (from MSI)

Symbol	Definition	Value	Units
d_{31}	Piezoelectric Strain Constant	-9.055×10^{-10}	inches per Volt
d_{33}	Piezoelectric Strain Constant	1.299×10^{-9}	inches per Volt
C_p	Capacitance	2.452×10^{-9}	Farads per square inch
ε	Permitivity	2.794×10^{-12}	Farads per inch
	Maximum Operating Voltage	375	Volts
	Breakdown Voltage	1000	Volts
	Yield Strength	7252	psi

Inspection of Eq. (6.56) and Eq. (6.57) shows simple linear equations in the form

$$y = b + mx \tag{6.58}$$

where the independent variable is V, the dependent variable is the voltage dependent tension, the intercept b is the initial tension and m is made up of various geometric and material constants for the layered system. Thus, in the absence of an applied voltage, the calculated tensions should be the same as the initial values for the selected coupon and patch analyzed numerically in Chapter 5. This simple check of soundness shows the tensions P_x and P_y at zero voltage to be

$$P_x = .75 \frac{lb}{in} \tag{6.59}$$

$$P_y = 1.5 \frac{lb}{in} \tag{6.60}$$

As expected, these values are consistent with the initial values of membrane tension in the x and y direction.

Next, the linear relationship between tension and applied voltage is plotted in *Mathematica* as shown in Figure 6.4.

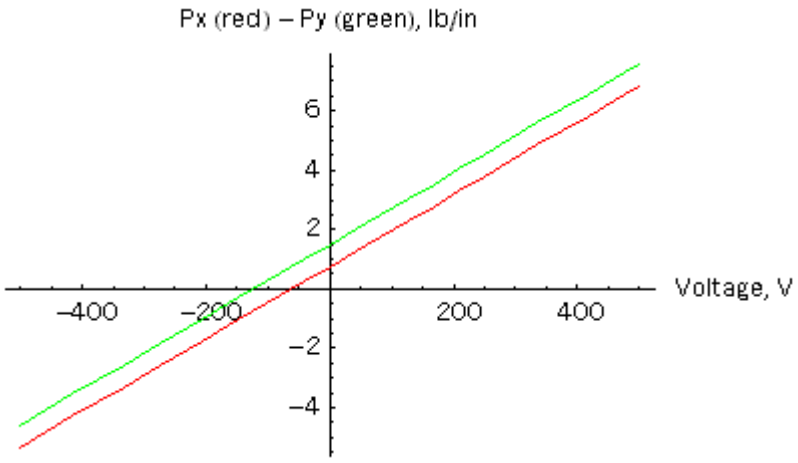

Figure 6.4: x and y Tensions versus Voltage Applied to PVDF Actuator

Despite this linear relationship that continues on theoretically forever, there are some practical limitations that must be evaluated. The most important limitation that must be applied to Figure 6.4 is the inability of a membrane to have a negative tension. By definition, membranes must have a positive tension, as any compressive loading would cause wrinkling and introduce nonlinear behavior beyond the scope of the current work. Thus, the portion of the red and green lines below the voltage axis is not physically possible. As the red line corresponds to the x direction tension, solving Eq. (6.56) with P_x equal to zero shows that –61.56 volts will cause wrinkling in the membrane. Consequently, the tension in the y direction will never be allowed to approach zero due to the -61.56 volt limitation from the x direction tension. Using Eq. (6.56) with this voltage, the minimum possible value of P_y is 0.75 pounds per inch. In addition to practical limitation stemming from the tension-only nature of membranes, restrictions involving the voltage applied to the actuator must be considered. First, adding a negative voltage to the patch will cause the stress to increase per Eq. (6.38) and Eq. (6.39). From the yield strength given in Table 6.3, the voltage required to yield the material is –5954 volts. This would lead one to think that extremely high voltages can be applied without damaging the material, but this not only violates the –61.56 volt minimum to sustain the tension in the membrane, but also Table 6.3 specifies the breakdown voltage as 1000 volts. If this breakdown voltage is exceeded, the material will become completely depoled and will no longer exhibit any piezoelectric behavior. A further restriction is given by the maximum operating voltage of 375 volts. If a voltage in excess of this magnitude is applied to the patch, arcing, overheating or slight depoling effects could result. Clearly, the maximum positive voltage is limited to 375 volts by the maximum operating voltage and the maximum negative voltage is limited to –61.56 volts by the inability of the membrane to support compressive loading. With these limitations in mind, Figure 6.5 shows the allowable operating voltage and possible tension values.

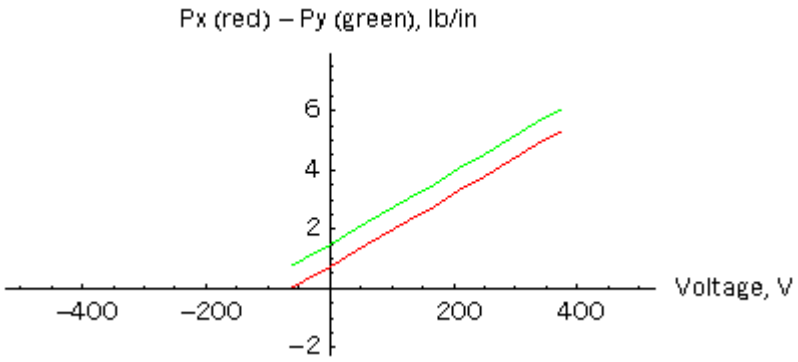

Figure 6.5: Allowable Operating Voltages and Possible Tension Values

From this figure, most of the ability to alter the tension in the membrane is in response to a positive voltage, which would cause the patch to decrease in size according to the sign convention adopted for the current work. Although one may wish to decrease the tension, attempts to reduce vibrations of the system will likely require an increase in the tension, for which the only limitation is the maximum operating voltage of the PVDF. Thus the patch is seen to have a considerable ability to change the tension in the base layer membrane. However, the limitations on applied voltages are critical to control system designers, as they often want to apply as much voltage as possible in order to maximize the possible actuation authority.

6.4 Summary:

Chapter 6 has thoroughly investigated the behavior of a membrane with fixed edges and an active PVDF attachment. After introducing the basics of piezoelectric material and their useful electromechanically coupled performance, a review of general elastic behavior was presented. From this complex tensor relationship, simplifications were made using contracted notation and the symmetric nature of the stress and strain tensors due to equilibrium requirements. These simplifications also reduced the number of independent elastic constants. With the mechanical behavior of any linear elastic body fully

understood, the constitutive relationship for piezoelectric materials was presented, first in general tensor notation. The tensor notation was then simplified a great deal by applying symmetry due to equilibrium and the crystal structure of PVDF. PVDF is also considered to be isotropic with respect to mechanical behavior and its permitivity. Lastly, the thin film nature and plane stress loading conditions for the layered membrane system under consideration in the current work were used to reduce the constitutive piezoelectric relationship to the relatively simple form shown in Eq. (6.19) through Eq. (6.22). Next, another limitation of membrane theory was uncovered when the PVDF was employed as a sensor for out-of-plane displacements. It was found that the use of membrane theory does not allow one to sense out-of-plane displacements with PVDF, as the restriction to small deflections for the membrane renders the direction dependent tensions constant with respect to transverse deflections. However, it was shown how the PVDF patch is modeled as an actuator to alter the tension in the membrane away from the patch. Using an approach analogous to the pin-force method, a fairly simple relationship between the x and y tensions and the voltage applied to the PVDF patch was found and presented in Eq. (6.56) and Eq. (6.57), respectively. A numerical example was presented using the same torus geometry, selected coupon and material properties as in other numerical and finite element simulations throughout this work. While a linear relationship between the tensions and voltage was predicted, some practical limitations were found that restrict the range of allowable voltages to between –61.56 and 375 volts in order to ensure positive tension in the base layer and safe operation of the PVDF actuator. These restrictions on allowable voltages will be crucial to control system designers in the future. Next, Chapter 7 presents some additional results from this research effort, summarizes the findings and conclusions and makes recommendations for future work dealing with the active control of inflatable satellites.

Chapter 7

Results, Conclusions and Future Work

7.1 Introduction:

This thesis has thoroughly investigated the use of traditional membrane theory to model the dynamic behavior of a coupon section from an inflated satellite constructed with a thin film material such as Kapton®. In addition, the change in vibration characteristics of the selected coupon with a passive piezopolymer attachment were investigated, as was the ability of the active patch to sense and reduce out-of-plane deflections. This final chapter begins with a brief summary of the analytical work performed. Then, additional key numerical results and trends stemming from the previous chapters are presented, followed by a summary of the conclusions and contributions offered by this work. Lastly, suggestions for future work are offered so this project can assist forthcoming researchers.

7.2 Brief Summary of Thesis:

This section summarizes the current research in an attempt to facilitate future scholars' understanding of its contents. The first chapter presents the inflatable

satellites of interest and the problems associated with such structures. A literature review is given to cover the fundamental concepts and current state of the art in the areas of inflatable satellite vibrations, membrane vibrations and piezoelectric materials in the context of intelligent structures. Chapter 2 presents a thorough discussion of the stresses developed in the material of an internally pressurized structure. In particular, the state of stress at a specific point on an inflated toroidal shell is discussed, and a flat coupon section of the torus was selected as the basis for the subsequent membrane vibration analysis. Understanding the nature of the stresses arising from the pressure used to inflate and sustain the torus section of the satellite is critical as these stresses form the basis of the tensions in the coupon required for the study of membranes. With the ability to calculate tensions in hand, summation of out-of-plane forces using Newton's Method in Chapter 3 resulted in a partial differential equation of motion for the rectangular coupon. This equation was solved in closed form using the separation of variables approach and fixed boundary conditions, giving explicit formulae for natural frequencies and mode shapes. Having an exact solution for a relatively simple system, Chapter 4 employed two popular approximation techniques, the Rayleigh-Ritz and finite element methods, to obtain natural frequencies and mode shapes for the same bare coupon section of the torus. A numerical comparison of these approximation methods showed close agreement, thus verifying their proper implementation and accuracy. With two reliable methods to approximate natural frequencies and mode shapes for a relatively simple membrane, the more complicated system consisting of the base layer coupon and a passive PVDF patch attachment was considered in Chapter 5. After a stress analysis of this layered system, a severe limitation of traditional membrane theory was encountered during the strain energy analysis. Specifically, traditional membrane theory was unable to predict the change in stiffness of the system due to the addition of the patch. This limitation is discussed in more detail shortly. Despite this drawback, the additional mass of

the patch was included in the model of the layered membrane system, which was found to have different natural frequencies but mode shapes similar to that of the single membrane layer. After assessing these changes in dynamic properties, the piezoelectric behavior of the patch bonded to the membrane base layer was investigated for potential application as an intelligent structure. Following a review of linear elasticity and basic electromechanical coupling behavior (piezoelectricity) of such materials, it was found that using traditional membrane theory to model the PVDF patch as a sensor for out of plane vibrations was not possible. However, the ability of the patch to actuate the base layer membrane by altering its tension as a function of applied voltage was quantified. The important results and trends alluded to above are summarized in the following section.

7.3 Key Results:

In Chapter 3, explicit expressions were found for the natural frequencies and mode shapes of the flat rectangular coupon with unequal tensions in the x and y directions. In subsequent chapters, a great deal of effort was spent in the calculation, approximation and analysis of the natural frequencies of the bare and layered membrane systems. Even though the mode shapes of a membrane are fairly well known, it is in the interest of completeness and uninformed readers that the first four mode shapes of the bare membrane analyzed numerically in Chapter 4 are shown in Figure 7.1.

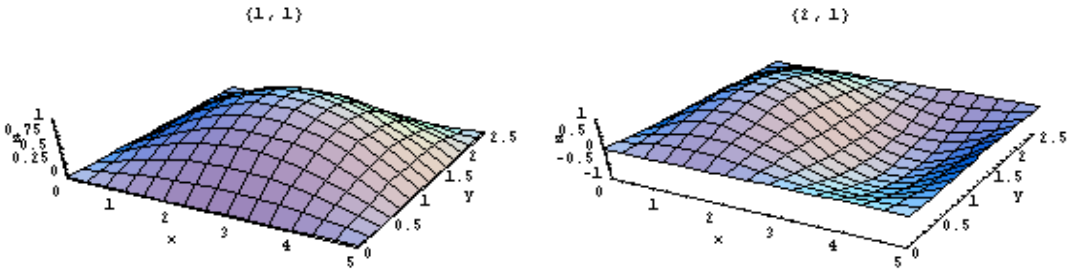

(a) (b)

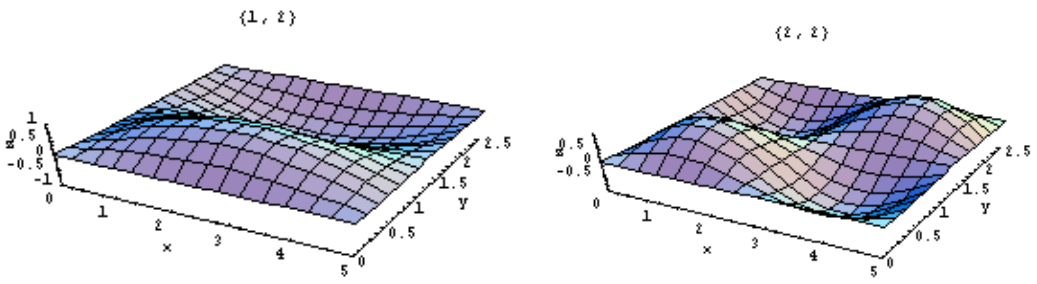

(c) (d)

Figure 7.1: Mode Shapes of Bare Membrane Numerically Examined in Chapter 4 with Exact Natural Frequencies (a) 411.678 Hz (b) 475.365 Hz (c) 788.303 Hz (d) 823.356 Hz

In Chapter 5, numerical results were presented for a membrane similar to that of Chapter 4, only with the addition of a one-fifth sized passive PVDF film attachment having a thickness of 0.0005 inch. After membrane theory was shown not to account for the added stiffness of the patch, the layered system, with the additional mass of the patch, was seen to have lower natural frequencies than the analogous bare membrane. Table 7.1 shows the decrease in natural frequencies.

Table 7.1: Comparison of Natural Frequencies for Bare and Layered Membranes

Wave Number		Natural Frequency, f, Hz		
x Dir.	y Dir.	Bare Membrane[1]	Membrane with PVDF Patch[2]	Percent Difference[3]
1	1	411.678	405.192	1.575%
2	1	475.365	474.416	0.200%
3	1	565.797	559.365	1.137%
4	1	672.267	668.084	0.622%
5	1	788.303	782.471	0.740%
1	2	788.303	786.735	0.199%
2	2	823.356	823.151	0.025%
3	2	878.675	877.355	0.150%
6	1	910.254	902.126	0.893%
4	2	950.730	949.988	0.078%

[1]Exact Solution
[2]12 Term Rayleigh-Ritz Solution
[3](Bare-Patch)/Bare

While the small patch considered for Table 7.1 produced slightly lower frequencies than the bare membrane, the effects of larger and thicker patches were also investigated. Table 7.2 shows the resulting natural frequencies when the size of the patch relative to the base layer was increased.

Table 7.2: Natural Frequencies for Various Amounts of Patch Coverage

Natural Frequency, *f*, Hz					
Frequency Number	Percent Coverage				
	4%	16%	36%	64%	100%
1	405.192	391.377	380.29	375.241	374.422
2	474.415	464.339	446.18	434.566	432.345
3	559.365	553.606	538.5	519.446	514.593
4	668.084	651.076	642.46	620.019	611.428
5	782.471	766.927	740.29	720.687	716.963
6	786.735	770.294	750.86	730.847	716.963
7	823.151	814.672	782.27	754.73	748.843
8	877.355	870.328	844.63	808.717	799.156
9	902.126	889.665	862.39	846.899	827.877
10	949.988	937.227	918.25	878.855	864.69

Table 7.3 shows the percent change in frequency from the initial one-fifth sized patch (4% coverage) to higher amounts of coverage for the ten lowest natural frequencies.

Table 7.3: Percent Decrease in Frequency from Initial One-Fifth Sized Patch

Frequency Number	Percent Decrease in Frequency from 4% Coverage to:			
	16%	36%	64%	100%
1	3.409%	6.145%	7.392%	7.594%
2	2.124%	5.952%	8.400%	8.868%
3	1.030%	3.730%	7.136%	8.004%
4	2.546%	3.835%	7.194%	8.480%
5	1.987%	5.391%	7.896%	8.372%
6	2.090%	4.560%	7.104%	8.869%
7	1.030%	4.967%	8.312%	9.027%
8	0.801%	3.730%	7.823%	8.913%
9	1.381%	4.405%	6.122%	8.230%
10	1.343%	3.341%	7.488%	8.979%

As expected, the added mass causes a decreasing trend in frequency. This trend is depicted graphically in Figure 7.2 for only the five lowest frequencies.

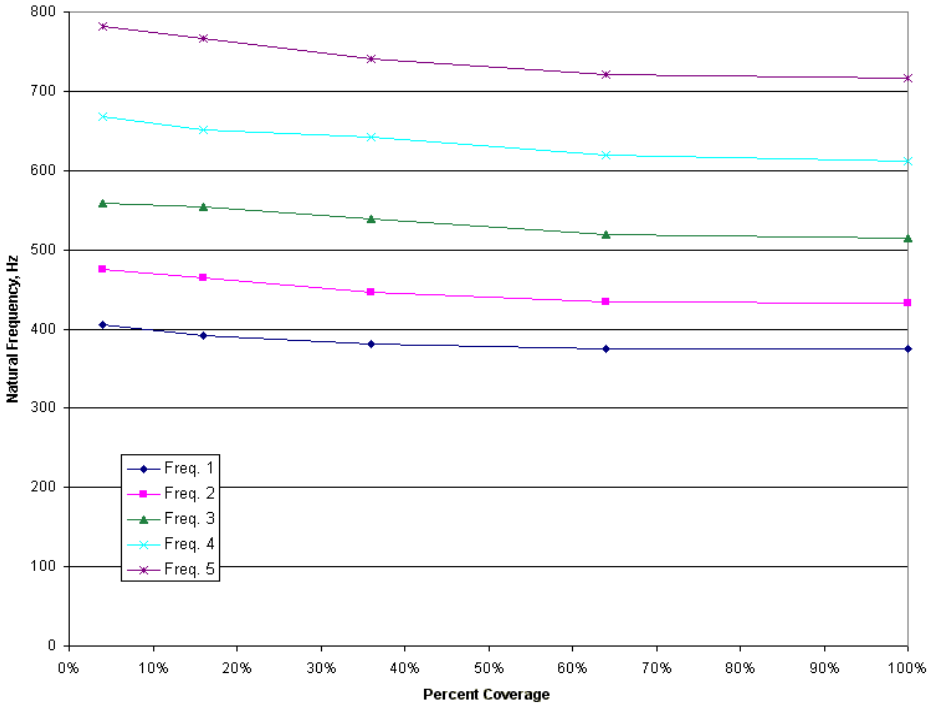

Figure 7.2: Decrease in First Five Frequencies for Increased Percent Coverage

In addition to investigating the changes in natural frequency due to varying the percent coverage of the base layer by the patch, mass was added to the system by increasing the thickness of the PVDF film. Table 7.4 illustrates the effects of increasing the thickness of the patch on the natural frequencies of the layered system.

Table 7.4: Natural Frequencies for Various Patch Thicknesses

Natural Frequency, f, Hz						
Frequency Number	Thickness of Patch, t_p, inches					
	0.0005	0.001	0.002	0.003	0.004	0.005
1	405.192	398.664	385.714	373.183	361.276	350.084
2	474.415	473.434	471.375	469.186	466.86	464.397
3	559.365	553.769	544.667	537.726	532.348	528.098
4	668.084	663.875	655.446	647.101	638.947	631.071
5	782.471	777.552	769.682	763.613	758.731	754.667
6	786.735	785.132	781.825	778.395	774.854	771.216
7	823.151	822.943	822.519	822.084	821.636	821.175
8	877.355	876.082	873.672	870.903	861.778	854.058
9	902.126	894.71	881.751	871.441	869.38	867.48
10	949.988	949.242	947.742	946.23	944.707	943.174

Table 7.5 shows the percent decrease in frequency from the initial 0.0005 inch thickness to various patch thickness sizes up to 0.005 inch.

Table 7.5: Percent Decrease in Frequency from Initial 0.0005 inch Patch

Frequency Number	Percent Decrease in Frequency from 0.0005 inch Patch to:				
	0.001	0.002	0.003	0.004	0.005
1	1.611%	4.807%	7.900%	10.838%	13.600%
2	0.207%	0.641%	1.102%	1.592%	2.112%
3	1.000%	2.628%	3.868%	4.830%	5.590%
4	0.630%	1.892%	3.141%	4.361%	5.540%
5	0.629%	1.634%	2.410%	3.034%	3.553%
6	0.204%	0.624%	1.060%	1.510%	1.973%
7	0.025%	0.077%	0.130%	0.184%	0.240%
8	0.145%	0.420%	0.735%	1.775%	2.655%
9	0.822%	2.259%	3.401%	3.630%	3.840%
10	0.079%	0.236%	0.396%	0.556%	0.717%

This decreasing trend is shown graphically in Figure 7.3 for the five lowest natural frequencies.

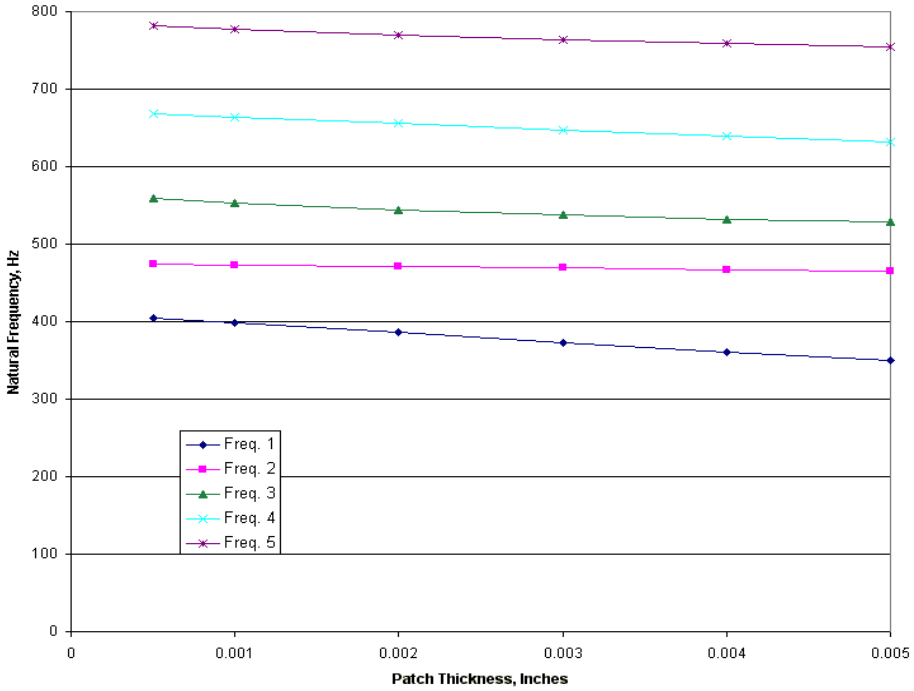

Figure 7.3: Decrease in First Five Frequencies for Increased Patch Thickness

It should be noted that doubling the mass by doubling the percent coverage does not produce the same change in frequency as doubling the mass of the patch by doubling its thickness. This is due to mass being more widely distributed when the percent coverage is increased. With some of the mass of the patch closer to the fixed edges, the velocity of that mass changes, which in turn alters its kinetic energy and contribution to the mass matrix given by Eq. (5.30).

In Chapter 6, Eq. (6.54) and Eq. (6.55) were derived to predict the tensions in the base layer away from the patch as a function of the voltage applied to the PVDF film actuator. Figure 6.5 showed graphically the restricted operating voltages and possible tension values for the layered membrane system analyzed numerically throughout Chapters 5 and 6. Table 7.5 recounts the range of voltages allowed to maintain a positive tension and safe operation of the membrane and the corresponding attainable tensions in the x and y directions.

Table 7.6: Voltage Restrictions and Corresponding Tensions

Minimum Voltage -250 Volts		Maximum Voltage 375 Volts	
P_x	0	P_x	5.32 lb/in
P_y	0.75 lb/in	P_y	6.07 lb/in

These limitations will be of key importance to control system designers in the future. When a positive voltage is applied, the tension in the membrane will increase, which will cause the membrane to appear stiffer thus having higher natural frequencies than when no voltage is applied to the patch.

7.4 Contributions and Conclusions:

At present, with the level of interest in inflatable space-based structures reaching an all time high, one of the top questions on the minds of researchers who work with these thin, lightweight high-tech devices is "can these structures be modeled as membranes?" From the results of the current research effort, the answer is "no." Within the stringent restrictions of traditional membrane theory, much of the detailed behavior of a layered film structure is lost. In this section, the contributions and conclusions drawn from the first six chapters of this work are specified.

While the vibration of membranes is routinely covered in most vibration texts, the treatment is often superficial and restricted to only the most simplified cases, such as sides of equal length and constant tension in all directions. In contrast, the present study has considered membranes where many of these restrictions have been relaxed. First, the coupon selected for numerical analysis from the torus was rectangular instead of a simple square. Also, the pressure vessel analysis in Chapter 2 showed that the tension in the torus material is not constant in all directions. As a result, this thesis details using both Newton's Method and

an energy approach to consider each direction of different tension independently and then combine the effects together to describe the behavior of the entire system.

In Chapter 5 when the addition of a passive PVDF patch was considered, the patch layer, in general, was smaller than the base layer. This mismatch in size required a more complex stress analysis and consideration of the interaction between the layers than the equal sized membranes considered by van Niekerk and Tongue [1995]. Despite the fact that the added mass of the patch was represented in the kinetic energy expression, derivation of the potential energy expression using traditional membrane theory for this layered system did not account for the added stiffness of the patch. An ANSYS finite element model using membrane elements substantiated this conclusion when the results were compared to the Rayleigh-Ritz approximation method. Specifically, membrane theory presumes small deflections such that the tension in a given direction does not change as the system undergoes out-of-plane vibrations. Even with step changes in the base layer stress, the state of stress in the Kapton® membrane is constant with respect to time and displacement. It is in this simplification that the ability to account for the added stiffness of the patch using membrane theory is lost.

Another limitation of traditional membrane theory was found when the PVDF patch was modeled as a sensor attached to the base layer membrane. Again, the small displacement-constant tension restriction rendered the PVDF film useless as a sensor for out-of-plane vibrations. In a static sense, a voltage is developed across the patch due to the initial state of stress arising from the internal pressure of the torus. However, piezoelectric materials make poor static sensors as the induced charge dissipates rapidly. Piezoelectric sensors should be used for dynamic measurements that occur at frequencies in excess of 0.001 Hz.

In contrast, the piezopolymer film found slightly more use as an actuator attached to the Kapton® substrate. Since both layers are considered to be membranes, application of a bending moment, as is the case with intelligent structures involving plates and beams, is not possible. The only way to model the interaction between the active patch and the host structure was through applied in-plane forces. With that, Eq. (6.54) and Eq. (6.55) give the tension in the base layer as a function of the voltage applied to the PVDF patch. While this could be used to attenuate transverse vibrational disturbances, modeling the actuator in this manner will not allow it to induce any vibrations in the membrane if it is at rest.

At the onset of this project, a coupon level investigation was selected to aid in understanding the amount of detail required when modeling the entire inflated torus structure with attached piezopolymer devices. This research effort has also shown that for the thin films used for such structures, the added mass of a PVDF device can affect the vibration behavior of the torus in the locations around a patch and should therefore be considered in a complete model of the torus as an intelligent structure. Further implications of this work on the modeling of the toroidal shell are presented in the next section.

7.5 Recommendations for Further Work:

While this work has served to better understand the applications and limitations of traditional membrane theory as it applies to thin layered film systems, there remains a great need for improved modeling techniques. As was rigorously shown in Chapter 5, membrane theory accounted for only the added mass of the PVDF patch, not its stiffness. Also, in Chapter 6, membrane theory was unable to model the piezopolymer as a sensor for out of plane vibrations of the base layer. To improve upon these limitations, a more advanced type of element, such as a thin plate, must be used to model the layered system. Thin plates are

considered to have a finite thickness and bending stiffness and the stress in the material is not constant, but rather a function of the out of plane displacement. These improvements add a level of complexity to the analysis but will allow one to predict changes in stiffness due to the patch layer and predict the voltage output from the patch when used as a sensor.

Since the patches have been shown to affect the dynamics of the torus, at least on a local level, the number of devices attached to the inflated structure to sense and reduce vibration levels should be minimized. Thus, some work should be done to model and design circuitry that utilizes the PVDF as both a sensor and an actuator simultaneously. This concept is known as self-sensing actuation.

In terms of the entire inflated satellite, some reduction in vibration transmission from the guidance and navigation hardware to the torus structure could be found through further investigation of the three inflated struts. They could be perhaps made out of fiber-reinforced composite laminates that cure after deployment and have either viscoelastic material layers or active fibers to reduce the transmission of vibrations.

Another area that has potential application to the inflated satellite of interest is the use of other types of active materials, such as shape memory alloys or active fiber composites. These types of material either are flexible like PVDF or can be manufactured to conform to the doubly curved surface of the toroidal shell. These materials could also be used on the membrane reflector for not only vibration suppression but also for static shape control.

References

1. Agnes, G. S. and Rogers, J. W., "Piezoelectric Excitation of Inflatable Space Structures for Modal Testing", SPIE Smart Materials and Structures Conference, March 2000.

2. Bambill, D. V., Gutierrez, R. H., Laura, P. A. A., and Jederlinic, V., 1997, "Vibrations of Composite, Doubly Connected Square Membranes," *Journal of Sound and Vibration*, Vol. 203, No. 3, pp. 542-545.

3. Banks, H. T., Smith, R. C., and Wang, Y., 1995, "The Modeling of Piezoceramic Patch Interactions with Shells, Plates, and Beams," *Quarterly of Applied Mathematics*, Vol. LIII, No. 2, pp. 353-381.

4. Briand, G., "Implementation of an Experiment to Find the Natural Frequencies of an Inflatable Structure with PVDF as Sensors", Summer Research Report, Center for Intelligent Material Systems and Structures, Virginia Polytechnic Institute and State University, 1999.

5. Coleman, A. D., "Solar Orbital Transfer Vehicle (SOTV), Pathfinder 3 Inflatable Concentrator Modal Survey Under Ambient Conditions TCP# SOTV-DEV-ED98-119," NASA, December 7, 1998.

6. Collins, S. A., Miller, D. W., and von Flotow, A. H., "Sensors for Structural Control Applications using Piezoelectric Polymer Film," Masters Thesis, Massachusetts Institute of Technology, October 1990.

7. Crawley, E.F., and de Luis, J., "Use of Piezoelectric Actuators as Elements of Intelligent Structures," *AIAA Journal*, Vol. 25, No. 10, pp. 1373-1385, October 1987.

8. Dosch, J. J., Inman, D. J., and Garcia, E., 1992, "A Self-Sensing Piezoelectric Actuator for Colocated Control," *Journal of Intelligent Material Systems and Structures*, Vol. 3, No. 1, pp. 166-85.

9. Dowling, N. E., *Mechanical Behavior of Materials*, Second Edition, Prentice Hall, New Jersey, 1999.

10. DuPont Films, "High Performance Films: Kapton General Specifications" Bulletin GS-96-7, http://www.dupont.com/corp/markets/aerospace/products/kapton.html.

11. Freeland, R. E., and Veal, G. R., "Significance of the Inflatable Antenna Experiment Technology," AIAA-98-2104, pp. 2789-2796.

12. Griffith, D. T. and Main, J. A., "Modal Testing of an Inflated Thin Film Polyimide Torus Structure," *Proceedings, XVIII International Modal Analysis Conference*, February 2000.

13. Hagood, N. W., Chung, W. H. and von Flotow, A., "Modelling of Piezoelectric Actuator Dynamics for Active Structural Control," *Proceedings, 31st AIAA/ASME/ASCE/AHS Structures, Structural Dynamics and Materials Conference, Long Beach, CA*, May, 1990, pp. 2242-2256.

14. Ikeda, T., *Fundamentals of Piezoelectricity*, Oxford Science Publications, New York, 1996.

15. Inman, D. J., *Engineering Vibration*, Prentice Hall, New Jersey, 1996.

16. Jones, R. M., *Mechanics of Composite Materials, Second Edition*, Taylor & Francis, 1999.

17. Ketner, G., "Survey of Historical Incidences with Controls-Structures Interaction and Recommended Technology Improvements Needed to Put Hardware in Space," Tech. Rep. PNL-8646, Pacific Northwest Laboratory, Operated for the U. S. Department of Energy by Battelle Memorial Institute, 1989.

18. Kulkarni, G. and Hanagud, S. V., 1991, "Modeling Issues in the Vibration Control with Piezoceramic Actuators," *Transactions of the ASME: Smart Structures and Materials* AD-Vol.24/AMD-Vol. 123.

19. Lam, M. J., "Hybrid Active/Passive Models With Frequency Dependent Damping," Ph.D. Dissertation, Virginia Polytechnic Institute and State University, October 1997.

20. Langley, R. S., 1995, "The Effect of Attachments on the Natural Frequencies of a Membrane," *Journal of Sound and Vibration*, Vol. 188, No. 5, pp. 760-766.

21. Lummer, D., "Theoretical and Experimental Investigations of Piezoelectric Bending Actuators," Masters Thesis, Virginia Polytechnic Institute and State University, December 1998.

22. Magrab, E. B., *Vibrations of Elastic Structural Members*, Sijthoff & Noordhoff, Maryland, 1979.

23. Main, J. A., Carlin, R. A., Garcia E., Peterson, S. W. and Strauss, A. M., 1995, "Dynamic analysis of space-based inflated beam structures," *Journal of the Acoustical Society of America*, Vol. 97, No. 2, pp. 1035-1045

24. Masad, J. A., 1996, "Free Vibrations of a Non-Homogeneous Rectangular Membrane," *Journal of Sound and Vibration*, Vol. 195, No. 4, pp. 674-678.

25. Meirovitch, L., *Analytical Methods in Vibrations*, Macmillan Publishing, New York, 1967.

26. Meirovitch, L., *Principles and Techniques of Vibrations*, Prentice Hall, New Jersey, 1997.

27. Nurre, G. S., Sharkey, J. P., Nelson, J. D., and Bradley, A. J., "Preservicing Mission, On-Orbit Modifications to the Hubble Space Telescope Pointing Control System," *AIAA Journal of Guidance, Control, and Dynamics*, Vol. 18, No. 2, Mar.-Apr. 1995, pp. 222-229.

28. Pronsato, M. E., Laura, P. A. A. and Juan, A., 1999, "Transverse Vibrations of a Rectangular Membrane With Discontinuously Varying Density," *Journal of Sound and Vibration*, Vol. 222, No. 2, pp. 341-344.

29. Rao, S., *Mechanical Vibrations*, Second Edition, Addison Wesley, Massachusetts, 1990.

30. Rayleigh, J. W. S., *The Theory of Sound*, Dover Publications, New York, 1945.

31. Reddy, J. N., *Energy and Variational Methods in Applied Mechanics*, John Wiley & Sons, Inc., New York, 1984.

32. Roark, R. J., *Formulas for Stress and Strain*, McGraw-Hill, New York, 1975.

33. Saigal, S., Yang, T. Y., Kim, H. W. and Soedel, W., 1986, "Free Vibrations of a Tire as a Toroidal Membrane," *Journal of Sound and Vibration*, Vol. 107, No. 1, pp. 71-82.

34. Shames, I. H. and Dym, C. L., *Energy and Finite Element Methods in Structural Mechanics*, Taylor & Francis, 1985.

35. Shigley, J. and Mitchell, L, *Mechanical Engineering Design*, Fourth Edition, McGraw-Hill, New York, 1993.

36. van Niekerk, J. L. and Tongue, B. H., 1995, "Active Control of a Circular Membrane to Reduce Transient Noise Transmission," *Journal of Vibration and Acoustics*, Vol. 117, No. 7, July, pp. 252-258.

Appendix 1

<u>*Mathematica* Solutions to Spatial and Temporal Equations, See Section 3.3.2</u>:

In[1]:= **DSolve[X''[x] + α^2 * X[x] == 0, X[x], x]**

Out[1]= {{X[x] → C[2] Cos[x α] + C[1] Sin[x α]}}

In[2]:= **DSolve[2 * Y''[y] + β^2 * Y[y] == 0, Y[y], y]**

Out[2]= $\left\{\left\{Y[y] \to C[2]\ \text{Cos}\left[\frac{y\beta}{\sqrt{2}}\right] + C[1]\ \text{Sin}\left[\frac{y\beta}{\sqrt{2}}\right]\right\}\right\}$

In[3]:= **DSolve[T''[t] + γ^2 * c_1^2 * T[t] == 0, T[t], t]**

Out[3]= {{T[t] → C[2] Cos[t γ c_1] + C[1] Sin[t γ c_1]}}

Appendix 2

Mathematica Code for Rayleigh-Ritz Method, Bare Membrane, See Section 4.4:

```
ρ = 3.9828 * 10^-7; (*Define the mass per unit area of the membrane, in *)
κ = 2;(*Define the ratio of tension in the y-
  direction to the tension in the x direction*)
Px = 0.75; (*Define the tension in the x direction, in pounds per inch*)
M = 5; (*Define first modal index,
 increase for more terms in mode shape approximation*)
NN = 5; (*Define second modal index,
 increase for more terms in mode shape approximation*)
stiffness = Array[k, {M*NN, M*NN}];
mass = Array[m, {M*NN, M*NN}];

(*Define Modes*)
Clear[m, n, i, u]
i = 1;
Do[u[i] = Sin[m*π*x/a] * Sin[n*π*y/b]; i = i + 1, {m, 1, M}, {n, 1, NN}]
Clear[m, n, i]

For[i = 1, i ≤ M*NN, utotal[i] = Sum[u[n], {n, 1, i}]; i++]

Clear[i]

(*Calculate L operators*)
For[i = 1, i ≤ M*NN, Lu[i] = -Px*(D[utotal[i], {x, 2}] + κ*D[utotal[i], {y, 2}]);
 i++]
Clear[i, j]

a = 5; (*Define the x dimension of the rectangle, in inches*)
b = 2.5; (*Define the y dimension of the rectangle, in inches*)

(*Calculate Lower Triangle of Stiffness Matrix and Display Required Time*)
Timing[For[i = 1, i ≤ M*NN, For[j = 1, j ≤ i, k[i, j] =
    Integrate[utotal[i]*Lu[j], {x, 0, a}, {y, 0, b}]; j++]; i++]]
Clear[i, j]

(*Calculate Mass Matrix and Display Required Time*)
Timing[For[i = 1, i ≤ M*NN, For[j = 1, j ≤ M*NN, m[i, j] =
    Integrate[utotal[i]*ρ*utotal[j], {x, 0, a}, {y, 0, b}]; j++]; i++]]
Clear[i, j]

(*Using Symmetry, Defining Top Triangle of Stiffness Matrix*)
Do[k[i, j] = k[j, i], {i, 1, M*NN}, {j, 1, M*NN}]
```

```
(*Display Stiffness and Mass Matrices*)
MatrixForm[Chop[stiffness]]
MatrixForm[Chop[mass]]

(*Calculate Natural Frequencies, in Hz*)
khat = MatrixPower[mass, -.5].stiffness.MatrixPower[mass, -.5];
MatrixForm[Chop[Sqrt[Eigenvalues[khat]] / (2 * π)]]

(*Calculate EigenVectors and Transform to Mode Shapes*)
evectors = Eigenvectors[khat];
modeshapes = MatrixPower[mass, -.5].Transpose[evectors];
MatrixForm[modeshapes]
```

Appendix 3

Mathematica Code for Rayleigh-Ritz Method, Membrane with PVDF Patch, See Section 5.4:

```
ρ = 3.9828 * 10^-7; (*Define the mass per unit area of the membrane, in *)
ρp = .0643/386.4 * .0005; (*Define the mass per unit area of the PVDF patch, in *)
κ = 2; (*Define the ratio of y-tension to the x-tension*)
Px = 0.75; (*Define the tension in the x direction, in lb per inch*)
M = 6; (*Define first modal index,
 increase for more terms in mode shape approximation*)
NN = 2; (*Define second modal index,
 increase for more terms in mode shape approximation*)
stiffness = Array[k, {M*NN, M*NN}];
mass = Array[m, {M*NN, M*NN}];

(*Define Approximate Modes and Their Sums*)
Clear[m, n, i, u]
i = 1;
Do[u[i] = Sin[m*π*x/a] * Sin[n*π*y/b]; i = i + 1, {m, 1, M}, {n, 1, NN}]
Clear[m, n, i]

For[i = 1, i ≤ M*NN, utotal[i] = Sum[u[n], {n, 1, i}]; i++]

Clear[i]

(*Calculate L operators*)
For[i = 1, i ≤ M*NN, Lu[i] = -Px*(D[utotal[i], {x, 2}] + κ*D[utotal[i],
       {y, 2}]); i++]
Clear[i, j]

a = 5; (*Define the x dimension of the rectangle, in inches*)
b = 2.5; (*Define the y dimension of the rectangle, in inches*)
x1 = 2; (*Define x location of lower left patch corner*)
x2 = 3; (*Define x location of upper right patch corner*)
y1 = 1; (*Define y location of lower left patch corner*)
y2 = 1.5; (*Define y location of upper right patch corner*)

(*Calculate Lower Triangle of Stiffness Matrix and Display Required Time*)
Timing[For[i = 1, i ≤ M*NN, For[j = 1, j ≤ i, k[i, j] =
    Integrate[utotal[i]*Lu[j] dx dy, {x, 0, a}, {y, 0, b}]; j++]; i++]]
Clear[i, j]
```

```
(*Calculate Mass Matrix and Display Required Time*)
Timing[
 For[i = 1, i ≤ M*NN,
  For[j = 1, j ≤ i,
   m[i, j] = ∫_0^b ∫_0^a utotal[i]*ρ*utotal[j] dx dy +
     ∫_y1^y2 ∫_x1^x2 utotal[i]*ρp*utotal[j] dx dy; j++]; i++]]
Clear[i, j]

(*Using Symmetry, Defining Top Triangle of Stiffness and Mass Matrices*)
Do[k[i, j] = k[j, i], {i, 1, M*NN}, {j, 1, M*NN}]
Clear[i, j]
Do[m[i, j] = m[j, i], {i, 1, M*NN}, {j, 1, M*NN}]
Clear[i, j]

(*Display Stiffness and Mass Matrices*)
MatrixForm[Chop[stiffness]]
MatrixForm[Chop[mass]]

(*Calculate Natural Frequencies, in Hz*)
khat = MatrixPower[mass, -.5].stiffness.MatrixPower[mass, -.5];
Chop[Sqrt[Eigenvalues[khat]] / (2*π)]

(*Calculate EigenVectors and Transform to Mode Shapes*)
evectors = Eigenvectors[khat];
modeshapes = MatrixPower[mass, -.5].Transpose[evectors];
MatrixForm[Chop[modeshapes]]
```

Vita

The author, Robert Brett Williams, was born on February 7, 1977, in Portsmouth, Virginia, as the first of two children to Bob and Mary Williams, a member of the United States Navy and a legal secretary turned domestic engineer. After growing up in Norfolk, Virginia, and graduating with honors from Maury High School in 1995, Brett obtained a Bachelor of Science degree in Mechanical Engineering, Magna cum Laude from Virginia Polytechnic Institute and State University in May 1999. During his undergraduate studies, Brett held various engineering positions. The completion of this work in August 2000 marks the completion of Brett's Master of Science degree in Mechanical Engineering, Summa cum Laude, also from Virginia Tech. Before leaving college, Brett will study fiber-reinforced composite materials at Virginia Tech in pursuit of his Doctor of Philosophy degree in Mechanical Engineering under the tutelage of Dr. Daniel J. Inman. In the future, Brett would like to work in the aerospace industry as a rocket scientist and obtain a Professional Engineering license and a Master of Business Administration degree. After achieving these lofty goals, Brett would like to return to academia to be a professor where his dedication to professional, high-quality work can be better realized.

In his free time, Brett enjoys such outdoor activities as golf, tennis, swimming, running, skiing and SCUBA diving. Additionally, Brett is an avid movie, comedy and music fan and likes to shop and travel, particularly to spring break. It is to his good fortune that many of these interests and activities are shared by his loving girlfriend, Rachel Bachman.